

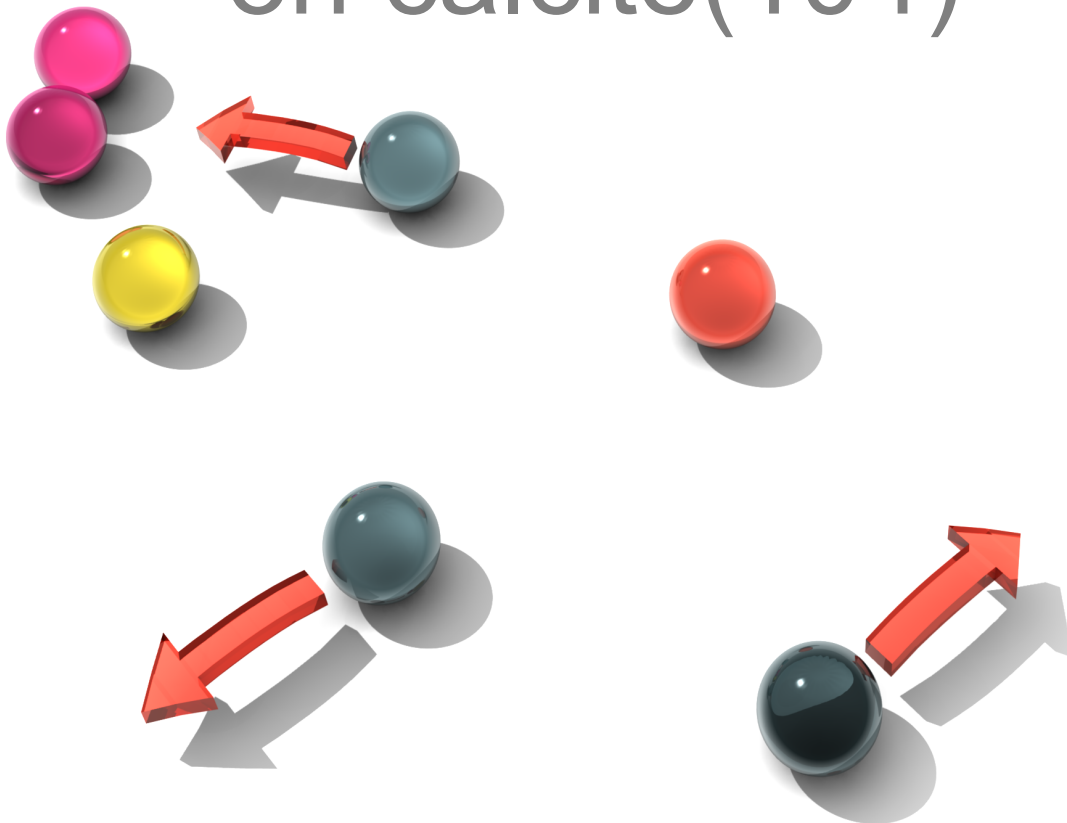
Mainz, den 6. Januar 2016

Felix Horst Kling

geboren in Frankfurt am Main

# Diffusion and structure formation of molecules

## on calcite(104)



Dissertation zur Erlangung des Grades  
„Doktor der Naturwissenschaften“  
im Promotionsfach Chemie am Fachbereich  
Chemie, Pharmazie und Geowissenschaften der  
Johannes Gutenberg-Universität in Mainz

This thesis was supervised by [REDACTED] and was carried out at the Johannes Gutenberg University Mainz from January 2013 to January 2016.

**D77** (Dissertation Johannes Gutenberg-Universität Mainz)

**Dean of the Faculty**

**1st report**

**2nd report**

**Submitted:** 6th January 2016  
**Oral examination:** 3rd February 2016

# Abstract

The arrangement of molecules is of utmost importance for the properties of a material, as apparent, for example, in biominerals. Therefore, it is important to investigate how molecules arrange themselves, a process that is referred to as molecular self-assembly.

In this thesis, the self-assembly of several molecules on the insulating calcite(104) surface in ultra-high vacuum is examined using frequency-modulation atomic force microscopy (FM-AFM). The calcite(104) surface is of special interest, for instance due to its relevance for biomineralisation.

The main goal of this thesis is to understand molecular self-assembly at a fundamental level by studying the diffusion process of molecules. The ability of the molecules to move on the surface is essential for self-assembly, because immobile molecules cannot form ordered structures.

For the examination of the diffusion process, short image series of diffusing 2,5-dihydroxybenzoic acid molecules were acquired at low temperatures. A post-processing procedure to extract, among other things, the diffusion jump length and diffusion directions from these data is presented. Surprisingly, these molecules do not diffuse along the main symmetry directions of calcite(104), but along directions diagonal to the main symmetry directions instead.

In this context, the influence of different functional groups on the diffusion of terephthalic acid and two derivatives, namely aminoterephthalic acid and bromoterephthalic acid, is studied as well. The diffusion barrier is estimated in this case by identifying the temperature at which self-assembly takes place. It is found that the diffusion barrier is significantly higher for aminoterephthalic acid than for terephthalic acid and bromoterephthalic acid. For aminoterephthalic acid a detailed analysis of the diffusion and self-assembly process is shown in addition. This analysis includes direct imaging of all processes important for self-assembly: formation and dissociation of unstable clusters, nucleation and growth.

Another goal of this thesis is to learn more about the structure formation. The structures formed by molecules depend not only on temperature, but also on coverage.

Therefore, measurements with increasing coverage are performed in this thesis for terephthalic acid and 2,5-dihydroxybenzoic acid to characterise these systems. It is disclosed that 2,5-dihydroxybenzoic acid forms ordered structures only upon a certain coverage at room temperature. For terephthalic acid existing measurements are completed by identifying, for instance, a dense structure observed at high coverages as upright standing molecules.

In addition to the above-mentioned systems, the formation of the first water layer on a cooled calcite(104) surface is investigated with measurements at different coverages. It is discovered that water forms a  $(2 \times 1)$  superstructure at low coverages and a  $(1 \times 1)$  superstructure at a full monolayer coverage. These measurements represent the first direct imaging of water at sub-monolayer coverage on calcite(104) at molecular resolution.

” *A man who does not think for himself does not think at all.*

— **Oscar Wilde**

*The soul of man under socialism*, 1891



*Dedicated to my wife Tanja*





# Contents

<b>1</b>	<b>Introduction</b>	<b>1</b>
<b>2</b>	<b>Self-assembly of organic molecules on insulating surfaces</b>	<b>3</b>
2.1	Introduction . . . . .	3
2.2	Self-assembly principles . . . . .	4
2.2.1	General considerations . . . . .	4
2.2.2	Special situation on insulator surfaces . . . . .	12
2.3	Studied systems—state of the art . . . . .	13
2.3.1	Strategies for anchoring . . . . .	14
2.3.2	Decoupling molecule-surface and intermolecular interactions . . . . .	19
2.4	Outlook . . . . .	20
<b>3</b>	<b>Frequency-modulation atomic force microscopy</b>	<b>21</b>
3.1	Basic principle . . . . .	21
3.2	Setup . . . . .	24
3.3	Feedback loops . . . . .	26
3.4	The instrument . . . . .	28
<b>4</b>	<b>Substrate and molecules</b>	<b>29</b>
4.1	The calcite(104) surface . . . . .	30
4.2	The molecules . . . . .	31
<b>5</b>	<b>Data processing</b>	<b>33</b>
5.1	TrackRead—processing motion tracking data . . . . .	33
5.1.1	Image preparation . . . . .	33
5.1.2	Processing with <i>TrackRead</i> . . . . .	34
5.2	I12c . . . . .	37
5.2.1	Calibration mode . . . . .	37
5.2.2	Drift correction with 2D-FFTs . . . . .	42
5.2.3	Choosing the proper drift correction method . . . . .	44
5.3	Justin . . . . .	45
5.3.1	Procedure . . . . .	46
5.3.2	Comparison with manual measurement and evaluation . . . . .	48

<b>6</b>	<b>2,5-DHBA</b>	<b>51</b>
6.1	The system . . . . .	51
6.2	Coverage dependence . . . . .	53
6.3	Diffusion . . . . .	55
6.3.1	Data acquisition . . . . .	55
6.3.2	Data processing and results . . . . .	56
6.3.3	Conclusion . . . . .	59
<b>7</b>	<b>Terephthalic acid and its derivatives</b>	<b>61</b>
7.1	TPA at room temperature and elevated temperatures . . . . .	62
7.2	Controlling self-assembly: diffusion studies of terephthalic acid and its derivatives . . . . .	65
7.2.1	TPA and BrTPA at low temperatures . . . . .	65
7.2.2	Characterising diffusion in detail and monitoring self-assembly with molecular resolution: ATPA at low temperatures . . . . .	67
7.3	Conclusion . . . . .	69
<b>8</b>	<b>Water on calcite(104)</b>	<b>71</b>
8.1	Temperature-programmed desorption measurements . . . . .	72
8.2	FM-AFM measurements . . . . .	73
8.3	Structural model and comparison with literature . . . . .	76
8.4	Conclusion . . . . .	77
<b>9</b>	<b>Conclusion and outlook</b>	<b>79</b>
<b>10</b>	<b>Appendix</b>	<b>81</b>
10.1	Change of the resonance frequency . . . . .	81
10.2	Substrate and molecules . . . . .	82
10.3	2,5-DHBA . . . . .	83
10.3.1	The $c(4\times 2)$ phase . . . . .	83
10.3.2	Deriving the binomial distribution for a random walk . . . . .	84
10.3.3	Deriving the Poisson distribution for the number of jumps . . . . .	84
10.3.4	Combining Poisson distribution and random walk . . . . .	85
10.3.5	Diffusion measurements—image series . . . . .	86
10.3.6	Graphs for the second measurement . . . . .	91
10.4	ATPA diffusion and self-assembly . . . . .	92
10.5	Software list . . . . .	93
	<b>Bibliography</b>	<b>95</b>
	<b>List of acronyms</b>	<b>109</b>

# Introduction

Self-assembly is everywhere.<sup>[1]</sup> From large-scale objects like galaxies and stars to minerals and the lipid bilayer forming cell membranes, everything involves the reversible formation of ordered structure whilst minimising the Gibbs energy. So how does it come that those things evolve? For galaxies and stars, it is mainly gravity that creates organised structures from gas clouds. For small structures like minerals and lipid bilayers, it comes down to interatomic or intermolecular interaction which is basically electrostatics.<sup>[2]</sup> These examples show that nature largely takes advantage of self-assembly. Living organisms even found a way of controlling the self-assembly process of minerals using an organic matrix to produce so called biominerals with tailor-made properties.<sup>[3]</sup> A typical example of a biomineral is nacre, which is composed of aragonite, but has an iridescent appearance and displays a much higher toughness than the pure mineral. Thus, understanding molecular self-assembly in detail is not only the key to mimicking nature, but also to the creation of new materials with exciting properties.

A logical first step for investigating self-assembly is to study a limited number of molecules confined to two-dimensional self-assembly by using a flat surface as template. With the emergence of scanning probe microscopy, especially scanning tunnelling microscopy<sup>[4]</sup> and atomic force microscopy<sup>[5,6]</sup>, it has become possible to image single molecules on a surface directly. By clever design of the molecules and a lot of try and error, several different structures like complex molecular island structures<sup>[7]</sup>, stripes<sup>[8,9]</sup>, porous networks<sup>[10–12]</sup> and host-guest systems<sup>[13,14]</sup> have been created. Still, predicting the structure a certain molecule will form on a given substrate is difficult if not impossible at present. A small change of the chemical formula, for example substituting a hydrogen atom with a methyl group<sup>[15]</sup>, can influence the self-assembled structures strongly. This is caused by the subtle interplay between molecules among each other and the surface lattice. Small energy differences can decide which adsorption position is preferred and how the molecule interacts with other molecules.

In this thesis, the self-assembly of several molecules on the insulating calcite(104) surface<sup>[16]</sup> is examined using frequency-modulation atomic force microscopy (FM-AFM). The calcite(104) surface is of special interest, for instance due to its relevance for biomineralisation.<sup>[17]</sup>

One goal of this thesis is to understand molecular self-assembly at a more fundamental level by studying the diffusion process<sup>[18–22]</sup> of molecules. The ability of the molecules to move on the surface is essential for self-assembly, because immobile molecules cannot form ordered structures.

The organic molecules probed in this thesis form self-assembled structures at room temperature. Hence, they start to move at lower temperatures and the sample needs to be cooled for diffusion measurements. Due to the low scanning speed and large thermal drift during variable temperature measurements, the know-how for observing the diffusion of single molecules needs to be gained in a first step. Among other things, software for fast and precise determination of drift speed during data acquisition is required (Section 5.2). The next step is to develop a post-processing procedure for a precise diffusion analysis which is presented in Sections 5.1 and 6.3. For these measurements, 2,5-dihydroxybenzoic acid is used. This is a remarkable molecule, because a phase transition attributed to a deprotonation<sup>[23]</sup> is observed after sublimation at room temperature on calcite(104).

Furthermore, the influence of different functional groups on the diffusion of terephthalic acid and two derivatives, namely aminoterephthalic acid and bromoterephthalic acid, is studied in Section 7.2. The diffusion barrier is estimated in this case by identifying the temperature at which self-assembly takes place. For aminoterephthalic acid a detailed analysis of the diffusion and self-assembly process is presented in addition.

Besides, the structures formed by molecules depend not only on temperature, but also on coverage.<sup>[24]</sup> This can be compared to states of aggregation in three dimensions, where temperature and pressure decide which phase is energetically favourable. At low coverages, the molecules may form some kind of two-dimensional molecular gas. At high coverages, many molecules form dense, ordered structures similar to bulk crystal formation. Some molecules even display several ordered phases for different coverages if the formation of a denser structure is preferred over the formation of a second layer.<sup>[25]</sup>

Therefore, measurements with increasing coverage are performed in this thesis for some of the molecules to characterise the systems (Sections 6.2 and 7.1).

In addition to the above-mentioned systems, the formation of the first water layer on a cold calcite(104) surface is investigated in Chapter 8. This system has already been subject for theoretical studies<sup>[26]</sup> due to the relevance for biomineralisation and other processes. The measurements of this chapter represent the first direct imaging of water at sub-monolayer coverage on calcite(104) at molecular resolution.

To conclude, several aspects of self-assembly from single molecule diffusion and formation of the first ordered structures to coverage dependence of molecular assemblies are investigated in this thesis.

# Self-assembly of organic molecules on insulating surfaces

This chapter was written by Felix Kling, Ralf Bechstein, Philipp Rahe and Angelika Kühnle and published in *Noncontact atomic force microscopy* Volume 3.<sup>[27]</sup>

## 2.1 Introduction

The concept of self-assembly has been recognised as a most elegant tool for creating ordered, functional materials at all scales.<sup>[1]</sup> The most widespread use of this autonomous assembly process is probably found in solution chemistry, where supramolecular structures are formed from tailored molecular building blocks. Identified as a most powerful design principle, the development of this strategy has been honoured with the Nobel Prize in chemistry in 1987. The prize has been awarded jointly to Donald J. Cram, Jean-Marie Lehn and Charles J. Pedersen for "their development and use of molecules with structure-specific interactions of high selectivity".

This chemists' concept of molecular self-assembly has been transferred into the surface science community, starting with the deposition of molecules on to single-crystal surfaces under well-controlled conditions of an ultra-high vacuum environment. In the early days, rather simple molecules have been deposited on to metal surfaces with little control over the intermolecular and molecule-surface interactions. In fact, most of these early studies have been performed with small molecules such as carbon monoxide or benzene<sup>[28]</sup> to establish a fundamental understanding about the interaction of individual molecules with the surface. From this single-molecule perspective, studies moved towards investigating molecular ensembles. Larger, mostly organic molecules have been explored<sup>[29]</sup>, allowing for introducing intermolecular interactions in the structure formation, which marks the beginning of exploring molecular self-assembly on surfaces. It has soon been recognised that tuning the balance between molecule-surface and intermolecular interactions offers the potential for creating manifold structures on surfaces with dedicated functionality. Nowadays, molecular self-assembly is used in many applications, *e.g.*, for surface functionalisation to provide specific and even switchable properties, fabrication of sensors or biocompatible surfaces, to name but a few.<sup>[30,31]</sup>

So far, however, most knowledge has been gathered on metallic substrates, as many surface science techniques require electrically conducting surfaces.<sup>[24,32–36]</sup> Especially

scanning tunnelling microscopy<sup>[4]</sup>, providing the ability to directly image molecular structures with single-molecule and even sub-molecular resolution, has tremendously pushed these studies forward. The advent of non-contact atomic force microscopy<sup>[5,6]</sup> and the constant improvements in resolution has now opened the option to extend these studies to non-conducting surfaces.

When studying molecular self-assembly on insulating surfaces, several design principles remain unaltered, while at the same time new challenges and possibilities arise from the fundamental difference in the molecule-surface interaction. Qualitatively different structures can be achieved due to the fundamental differences in the molecule-surface interactions. These aspects will surely further enhance the variability of molecular self-assembly on surfaces. Together with the greatly enlarged materials basis, this will provide flexibility for future applications, *e.g.*, in the field of molecular electronics.

## 2.2 Self-assembly principles

In the following section, we first review basic principles relevant for self-assembly before discussing the specific situation when turning to insulator surfaces.

### 2.2.1 General considerations

Self-assembly describes the autonomous formation of ordered structures by pre-defined building blocks, controlled by the interaction between these constituting entities.<sup>[37]</sup> The impressive variety of organic synthesis offers an outstanding platform for providing a large variety of tailor-made organic molecules as building blocks with specific interactions both in terms of interaction strength and directionality.<sup>[38,39]</sup> The latter two features are clearly both of high importance when aiming for controlled structure formation. Consequently, the ability of fine-tuning both strength and directionality is pivotal for enlarging the structural variety of molecular self-assembly. An important aspect of molecular self-assembly is exploiting intermolecular interactions resulting in bond formation which is reversible at room temperature. This enables binding and unbinding of the molecular entities to eventually reach the thermodynamically most favourable structure.<sup>a</sup> Consequently, non-covalent bonds with binding energies in the range of tenth of an eV are typically employed. In smart designs often several interactions of the same or of various type and/or attractive and repulsive interactions are combined to create a desired structure. To give an overview, Table 2.1 summarises the relevant non-covalent interactions.

Categorising interactions regarding their strength is not straightforward. For most

---

<sup>a</sup>In contrast, the term self-organisation is typically used when discussing kinetically controlled structures such as diffusion-limited structures. However, the terms self-assembly and self-organisation are often used synonymously.

bond types listed in Table 2.1, examples can be found with binding energies in the range of small fractions of an eV up to roughly one eV. The strength of a specific bond is, however, not sufficiently described by stating the binding energy, *i.e.*, the depth of the pair potential at equilibrium distance. Bonds can be broken in many different ways, including the formation of transition states and possibly resulting in a new binding situation. For each process different parameters need consideration if the bond strength is to be characterised. For example, lifting a molecule from a surface *via* mechanical pulling requires applying a certain force determined by the maximum slope of the pair potential. For many processes it is necessary to consider how a potential decays with increasing distance between the binding partners. Fast decaying interactions of small binding energy might in some cases be stronger than slowly decaying interactions of large binding energy. The relevant bond-breaking process for self-assembled structures is usually thermal

**Tab. 2.1:** Characteristics of intermolecular interactions used in molecular self-assembly. This categorisation is to some extent ambiguous. Note that a bond is per definition an overall attractive interaction, whilst electrostatic interaction as such can be either attractive or repulsive.

Type	Directionality	Selectivity	Binding partners
Hydrogen bond	Highly directional	Highly selective	X-H and Y, where X and Y are more electronegative than H <sup>[40]</sup>
Halogen bond			Electrophilic region at halogen atom in a molecule and nucleophilic region in another <sup>[41]</sup>
Pnicogen bond			P and N bonded to electron donors/acceptors <sup>[42]</sup>
Carbon bond			Alkyl carbon bonded to electronegative partners and negative centres in polar molecules <sup>[43]</sup>
$\pi$ - $\pi$ bond		Selective	Aromatic molecules <sup>[44]</sup>
Metal coordination bond	Directional		Metal atoms and ligands <sup>[45]</sup>
Van-der-Waals interaction		Poorly selective	Dipoles and/or polarisable species
Ion-ion interaction	Isotropic		Monopoles

excitation, which is a statistical process. Here it makes sense to analyse the stability of the bond, *i.e.*, its average life time, which is the inverse of the dissociation rate. Whether a bond is considered stable depends on the binding strength but also on the temperature of the system and the time of observation. As simple model to describe thermally excited bond breaking, often an Arrhenius law is employed as described in the next chapter (Equation 2.1).

Classical electrostatic forces can be used to describe all intermolecular and molecule-substrate interactions that are relevant here once the electron density distribution in thermodynamic equilibrium is known.<sup>[2]</sup> The Coulomb force between charges is

the physical origin of interactions such as hydrogen, halogen, pnictogen and carbon bonds,  $\pi$ - $\pi$  bonds, metal coordination bonds, van-der-Waals and other electrostatic interactions<sup>b</sup> between monopoles, dipoles, quadrupoles and so on (see Table 2.1). The desire to classify electrostatic interactions into these somewhat ambiguous categories bears the risk to count the same force twice, but it allows grouping interactions regarding their directionality and selectivity.<sup>[46]</sup> The directionality of an interaction determines the geometry of the resulting assembly, while the selectivity decides how compatible accessible binding partners are. Especially hydrogen bonding motifs have been explored extensively, benefiting from the selectivity and strong directionality of this interaction. A clever design of the molecules allows for encoding the desired supramolecular structure in the molecular building blocks, explaining the tremendous success of supramolecular chemistry in the last decades.<sup>[47,48]</sup> Molecular self-assembly has also been explored for creating functional molecular structures on surfaces. Upon deposition of molecules on to a surface, a new dimension is obtained for controlling the final structure of the molecular self-assembly process by the molecule-surface interaction. Tailoring the ratio between intermolecular and the molecule-surface interactions allows for tremendously enlarging the structural variety of the resulting patterns.<sup>[32–35]</sup> On metals, structures ranging from two-dimensional molecular films<sup>[49,50]</sup> over one-dimensional wire-like structures<sup>[9,51,52]</sup> to complex patterns such as porous networks<sup>[10–12]</sup>, bi-molecular assemblies<sup>[53,54]</sup> or host-guest systems<sup>[13,14]</sup> have been created (see Figure 2.1).

A further interesting design principle is involving adsorbate-induced surface modi-

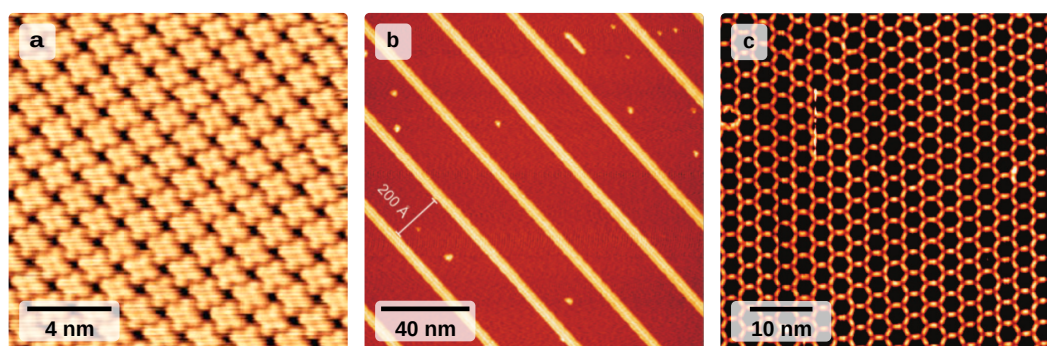


**Fig. 2.1:** Structural variety of self-assembled patterns ranging from **a** defect free two-dimensional layers (reprinted figure with permission from [49], copyright 2007 by the American Physical Society) to **b** one-dimensional wire-like structures (reprinted with permission from [9], copyright (2007) National Academy of Sciences, U.S.A.), eventually arriving at **c** complex patterns such as porous networks (reprinted with permission from [12], copyright 2007 American Chemical Society).

fications such as surface restructuring. This has been employed for creating, *e.g.*, uni-directional structures on an Au(110)-(1 $\times$ 2) surface<sup>[52]</sup>, driven by lifting the (1 $\times$ 2)

<sup>b</sup>All electrostatic interactions that have been awarded with a proper name are characterised by charge-transfer bonding, while "other electrostatic interactions" usually refers to interactions between permanent multipoles like ion-ion interaction. The latter can be either attractive or repulsive and is, therefore, a powerful instrument to develop structural complexity.



missing-row reconstruction. Further examples include structuring by charge density waves<sup>[55]</sup> and other substrate-mediated interactions<sup>[56]</sup>.

Most single-crystal metal surfaces exhibit a pronounced influence on the self-assembly of organic molecules *via* the molecule-surface interaction. This *templating effect* often originates from two different factors. First, most single-crystal metal surfaces exhibit a diffusion barrier,  $G_{\text{diff}}$ , in the range of several tenth of an eV for a single, isolated molecule.<sup>[19,21,57]</sup> This range is favourable for molecular self-assembly at room temperature as outlined below. Second, single-crystal surfaces can provide anisotropic diffusion parallel and perpendicular to the close-packed metal rows, constituting a further option for influencing the final structure.<sup>[19,58]</sup>

In the following, a simplified picture is considered to provide an estimate for diffusion barriers that allow for molecular self-assembly. Diffusion is a statistical process which can be modelled using an Arrhenius law (Equation 2.1). Here, the diffusion rate  $n_{\text{diff}}$  at a given temperature  $T$  is determined by the diffusion barrier  $G_{\text{diff}}$  and the attempt frequency  $\nu_0$  ( $k_{\text{B}}$  is the Boltzmann constant):

$$n_{\text{diff}} = n_0 \cdot e^{-\frac{G_{\text{diff}}}{k_{\text{B}}T}}. \quad (2.1)$$

In the following, we consider room temperature ( $T = 300 \text{ K}$ ) and an attempt frequency<sup>c</sup> of  $n_0 = 1 \times 10^{12} \text{ s}^{-1}$ .

The diffusion barrier,  $G_{\text{diff}}$ , must be small enough to allow for diffusion with a reasonable rate. To arrive at a well-ordered self-assembly within a realistic time frame, the diffusion barrier cannot be larger than 0.8 eV. According to Equation 2.1, this barrier corresponds to a diffusion rate of  $3.6 \times 10^{-2} \text{ s}^{-1}$  and each molecule performs on average 1000 hops within 8 hours. If the diffusion barrier is larger than that value, the molecules are practically immobile at room temperature (Figure 2.2a), inhibiting the formation of a self-assembled structure. Thus, the value of 0.8 eV can be regarded as an upper bound for the diffusion barrier. (We refer to Figure 2.2b for experimentally accessible diffusion barriers.)

At the same time, it is favourable to have a high diffusion barrier to ensure the surface having a templating effect on the final arrangement of the molecular ensemble. The mobility increases with lowering the diffusion barrier as shown in Figure 2.2a. However, if the diffusion barrier gets too low—a situation often encountered for molecules on prototypical insulating surfaces—the molecules diffuse rapidly on the surface with little control of the surface over the resulting molecular structure. In such a situation, the structure formation is governed entirely by the intermolecular interactions, typically resulting in the same molecular structure regardless of the

---

<sup>c</sup>For drawing a qualitative picture, we use a fixed attempt frequency of  $\nu_0 = 1 \times 10^{12} \text{ s}^{-1}$ . This value is motivated by the estimate of the phonon frequency of  $\frac{k_{\text{B}}T}{\hbar} = 6 \times 10^{12} \text{ s}^{-1}$ . When aiming for quantitative statements for a specific molecule-substrate system, the correct values for the attempt frequency and the diffusion barrier must be considered, because both parameters are equally important. For molecules at sub-monolayer coverage, attempt frequencies in the range of approximately  $1 \times 10^{10} \text{ s}^{-1}$  to  $1 \times 10^{20} \text{ s}^{-1}$  have been observed experimentally.<sup>[59]</sup>

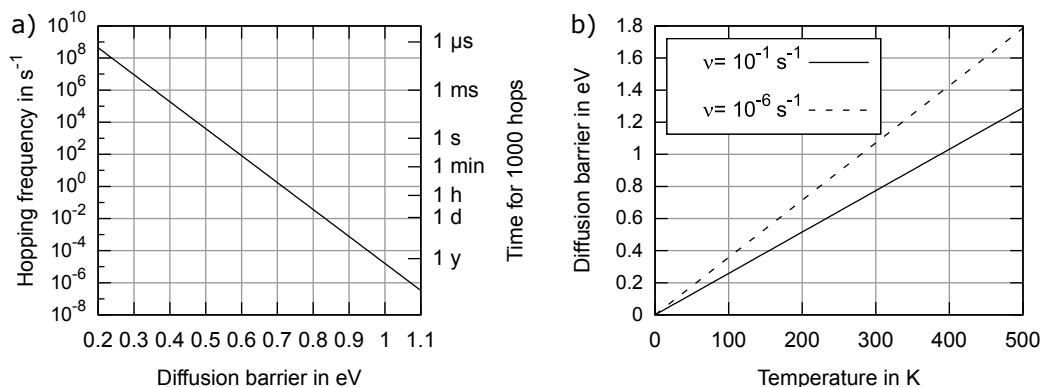


**Fig. 2.2:** a) Hopping frequency (diffusion rate) as a function of diffusion barrier (at  $T = 300$  K) and corresponding time required for a single molecule to perform on average 1000 hops. b) Diffusion barriers typically accessible in AFM experiments as a function of temperature assuming a maximum observable hopping frequency of  $0.1 \text{ s}^{-1}$  (corresponding to 95 % of the molecules move within 30 s) and a minimum hopping frequency of  $1 \times 10^{-6} \text{ s}^{-1}$  (corresponding to 10 % of the molecules move within one day) and  $\nu_0 = 1 \times 10^{12} \text{ s}^{-1}$ .

specific surface, namely the molecular bulk crystal.<sup>[60]</sup> Therefore, the diffusion barrier needs to be large enough to provide an influence of the substrate on the final structural arrangement. A simple estimate for a lower bound of the diffusion barrier will be obtained at the end of the following discussion.

The diffusion barrier is only one of the energies relevant for the self-assembly process. Self-assembly usually involves the deposition of the molecules from the gas phase as well as a transition from freely diffusing molecules to molecules arrested in an ordered phase. Thus, the change in entropy cannot be neglected. This is why the Gibbs free energy,  $G$ , has to be considered as the relevant quantity. The general free energy diagram is shown in Figure 2.3. Obviously, the molecules must not desorb from the surface. Thus, the binding energy of a single molecule to the surface, referred to as  $G_{\text{MS}}$  has to be large enough to ensure that the molecules remain on the surface for a sufficiently long time. In analogy to the above made estimate for the diffusion barrier, we can provide an estimate for the binding energy by regarding a molecule to be stable on the surface if less than one out of 100 molecules desorbs within a time span of one year. This corresponds to a lower bound for the binding energy of 1.3 eV at 300 K.<sup>d</sup>

The individual molecules diffuse on the surface and form islands, which are held together due to intermolecular interactions. In a very simple picture, we neglect the influence of the surface on the intermolecular interaction, *i.e.*, we consider the interaction of two molecules on the surface,  $G_{\text{mm}}$ , to be the same as in the gas phase, referred to as  $G_{\text{MM}}$ .

In equilibrium at a given temperature, only a certain fraction of molecules is in

<sup>d</sup>Alternatively, a cooperative effect can be envisioned. If impinging molecules stay sufficiently long on the surface to meet and form clusters with other molecules before desorption, the assembled molecules can stabilise themselves. This can allow for self-assembly even in a situation where individual molecules would desorb from the surface.

the thermodynamic minimum, *i.e.*, forming the desired (thermodynamically most favourable) structure. The other molecules are diffusing on the surface or form unwanted (thermodynamically less favourable) structures. The life time (inverse of the dissociation rate) for a single molecule to remain incorporated into the desired structure needs to be compatible with the desired time scale for the structure to remain unchanged (*e.g.*, the time required for experimental observation or the time of usage in an application). For applications such as self-assembled molecular electronic devices, the inevitable high life time requires a relatively high dissociation barrier,  $G_{\text{diss}}$  (similar to  $G_{\text{MS}}$ ).

The dissociation barrier of unwanted or kinetically trapped non-equilibrium structures, however, must be overcome within reasonable times, *i.e.*, it cannot be much larger than  $G_{\text{diff}}$ . For example, a maximum dissociation barrier of 0.9 eV for unwanted structures corresponds to the dissociation of 50 % of the bonds within 15 min.

To ensure a structural variety from a subtle balance between intermolecular and molecule-surface interactions, the dissociation barrier needs to be composed of both,  $G_{\text{MM}}$  and  $G_{\text{diff}}$  with considerable influence of both components. Assuming a typical pairwise intermolecular attraction adds a value of 0.3 eV to the binding energy of each molecule (and thereby to the dissociation barrier) and further assuming a molecule to be bound to two other molecules, we arrive at a lower bound for the diffusion barrier of 0.7 eV in order to reach a dissociation barrier of 1.3 eV as required for applications like molecular electronics.

From this very simple estimate, we can readily understand why diffusion barriers favouring applicable molecular self-assembly at room temperature are typically in a very narrow energy range (in our estimation 0.7 eV to 0.8 eV).

The above estimation contains many simplifications. In the presence of a surface, the intermolecular interaction will be altered due to geometric constraints as well as changes in the electronic structure due to adsorption. Thus, we have to exchange the intermolecular interaction in gas phase by the interaction of two molecules adsorbed on to the surface,  $G_{\text{mm}}$ . There might be a barrier for the formation of an island,  $G_{\text{form}}$ , with a corresponding rate,  $\nu_{\text{form}}$ . The latter should be high (corresponding to a small barrier) for self-assembly. Additionally, the dissociation barrier,  $G_{\text{diss}}$ , might not be obtained by a simple addition of the intermolecular interaction energy,  $G_{\text{mm}}$ , and the diffusion barrier,  $G_{\text{diff}}$ . From the above discussion, a condition for the involved rates can be obtained:

$$\nu_{\text{des}} \approx \nu_{\text{diss}} \ll \nu_{\text{diff}} < \nu_{\text{form}}. \quad (2.2)$$

According to Equation 2.1, the following relation can be deduced for the energies:

$$G_{\text{MS}} \approx G_{\text{diss}} > G_{\text{diff}} > G_{\text{form}}. \quad (2.3)$$

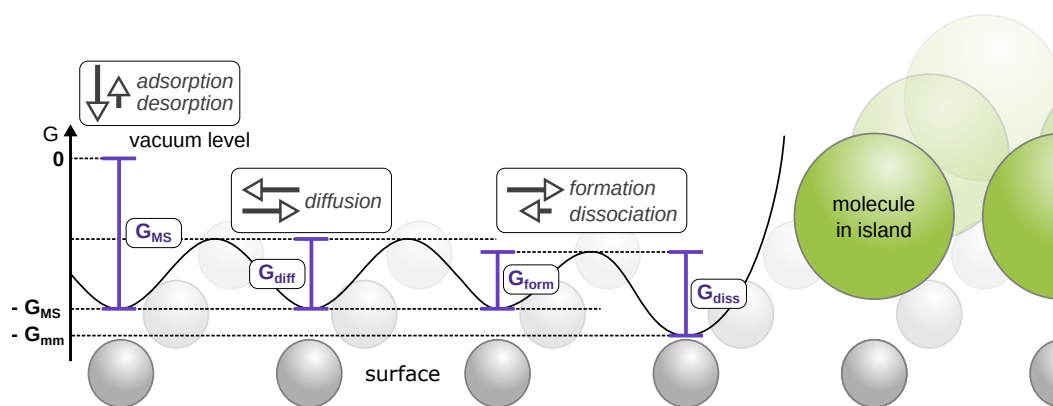


**Fig. 2.3:** Gibbs free energy for a molecule adsorbing from the gas phase. Note that favourite adsorption sites are arbitrarily chosen to be on top of the surface atoms. After adsorption, the molecule can diffuse on the surface until it reaches a spot next to another molecule on the surface (other possible nucleation sites are neglected in this simplified picture). The change in free energy when two molecules (from the gas phase) bind towards each other on the surface,  $G_{mm}$ , also includes the effect of the surface. Only in the (very unrealistic) case of a molecular geometry that is unperturbed by the presence of the surface,  $G_{mm}$  can be obtained from the superposition of the interaction of the molecules in the gas phase,  $G_{MM}$ , and the contribution of the surface  $G_{MS}$ .

It is important to note that, although the rates span a wide range, the relevant barriers are in a very narrow energy range. Thus, molecule-surface and molecule-molecule interactions need to be tuned very precisely with an accuracy typically better than 0.1 eV.

With this discussion, it can be readily understood that metastable structures

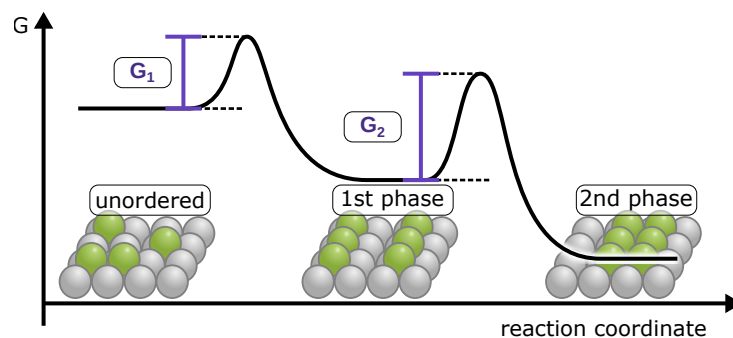


**Fig. 2.4:** Situation resulting in a metastable structure that transforms with time (or upon annealing) into the thermodynamically favoured structure.

can form that are favourable kinetically, but unfavourable thermodynamically (see Figure 2.4). In such a situation, a small (or no) barrier,  $G_1$ , exist for the formation of a thermodynamically unstable structure (phase 1), while the formation of the thermodynamically favoured structure (phase 2) is hindered by a large activation barrier,  $G_2$ . Depending on the barrier height  $G_2$ , annealing or simply waiting will drive the system into the thermodynamically favoured phase 2. Such a transformation has been observed, *e.g.*, for the deprotonation of 2,5-dihydroxybenzoic acid on calcite(104).<sup>[23]</sup> Besides the situation sketched in Figure 2.4, different structures at

different temperatures can also occur, because the thermodynamic minimum can change upon temperature due to entropic effects. This situation can be differentiated from the upper mentioned case of a kinetically hindered structure by cycling the temperature.<sup>[61]</sup> If the thermodynamic minimum changes with temperature, different phases form repeatedly. This is different for a kinetically hindered structure, where the system will remain in the energetically favourable structure independent of the temperature once this structure is reached.

Another aspect that needs to be considered is the coverage dependence of molecular self-assembly. It is known that low-density phases can be favoured at low coverages, whilst increasing coverage can result in high-density phases prior to the formation of a second layer.<sup>[25]</sup> Often higher densities are accompanied by different adsorption positions and, thereby, a change in the molecule-substrate interaction. On the other hand, the molecule-molecule interaction may increase, since entropy effects such as the preference of mobility over island formation do no longer prevail. Therefore, phase diagrams depending on both temperature and coverage are found in literature.<sup>[24]</sup> In addition, a general trend exists for the island size depending on temperature, *i.e.*, at low temperatures the rate for diffusion and island dissociation is smaller according to Equation 2.1 and, therefore, the molecules cluster into smaller islands. This also implies that the existence of many small molecule islands indicates a high diffusion and dissociation barrier, while large islands indicate the opposite. In fact, the diffusion barrier can be determined by measuring the size or the density of the islands at different temperatures.<sup>[62,63]</sup>

Furthermore, the energy barrier for island formation is usually not independent of the island size. It needs to be considered that nucleation requires higher energies and is less likely than the subsequent island growth. This is why step edges, surface defects or even intentionally added adsorbates<sup>[64]</sup> can reduce the nucleation barrier and, thus, are often observed as starting point for island growth.

Finally, it should be noted that this very simple discussion does not include specific aspects, such as anisotropic diffusion, details of intermolecular interaction or temperature-dependent attempt frequencies. However, the above discussion readily shows that molecular self-assembly surely requires matching an appropriate balance between the involved energies. Adjusting the involved interactions can be challenging as changing, *e.g.*, the intermolecular interaction by adding specific groups will almost always simultaneously influence the molecule-surface interaction and *vice versa*. An interesting strategy to facilitate tuning of the involved energies is, therefore, designing molecules that allow for largely separating intermolecular and molecule-surface interactions as will be discussed in 2.3.2.

## 2.2.2 Special situation on insulator surfaces

In contrast to many single-crystal metal surfaces, a favourable balance between the involved interactions is more difficult to achieve for most insulating surfaces investigated so far. Prominent insulating support materials for molecular assemblies are stable cleavage planes of alkali halides<sup>[60,64–91]</sup>, such as KBr(001), NaCl(001), KCl(001) or RbCl(001), the (111) cleavage plane of the fluoride CaF<sub>2</sub><sup>[7,63,92–94]</sup>, oxide surfaces such as MgO(001) or Al<sub>2</sub>O<sub>3</sub>(001)<sup>[65]</sup> as well as diamond and mica<sup>[95]</sup> surfaces. Recently, the calcite(104) surface<sup>[8,23,96–106]</sup> has gained increasing attention for reasons discussed later.

In particular, the diffusion barrier of many organic molecules on these prototypical insulating surfaces has been found to be very low compared to metallic surfaces. This is illustrated by comparing the diffusion barrier of C<sub>60</sub> on a metallic and an insulating surface. On a Pd(110) surface, the diffusion barrier is a factor of 7 larger ( $\approx 1.4$  eV<sup>[57]</sup>) than on CaF<sub>2</sub>(111) ( $\approx 0.2$  eV<sup>[63]</sup>). As a consequence, the self-assembled growth is subjected to significantly different energy barriers, commonly leading to significant higher desorption and diffusion rates on CaF<sub>2</sub>(111) as compared to metals surfaces. Early work investigating the structure formation of "classical" molecular building blocks, namely porphyrin and perylenetetracarboxylic dianhydride (PTCDA), on KBr(001) and Al<sub>2</sub>O<sub>3</sub>(0001) surfaces reflects this discussion. High molecular mobility at room temperature and clustering at step edges is a common observation in this study.<sup>[65]</sup> In another pivotal work, the molecular structure of PTCDA clusters at KBr(001) step edges has been resolved, disclosing the molecular bulk crystal.<sup>[60]</sup> This finding readily illustrates the absence of substrate templating in this system (see Figure 2.5a and b). Even molecules with larger dipoles can exhibit low diffusion barriers as highlighted by syn-5,10,15-tris(4-cyanophenylmethyl)truxene on KBr(001)<sup>[80]</sup> diffusing rapidly at [010] step edges and only anchoring at kink sites (Figure 2.5c). Consequently, the weak molecule-substrate interaction found for

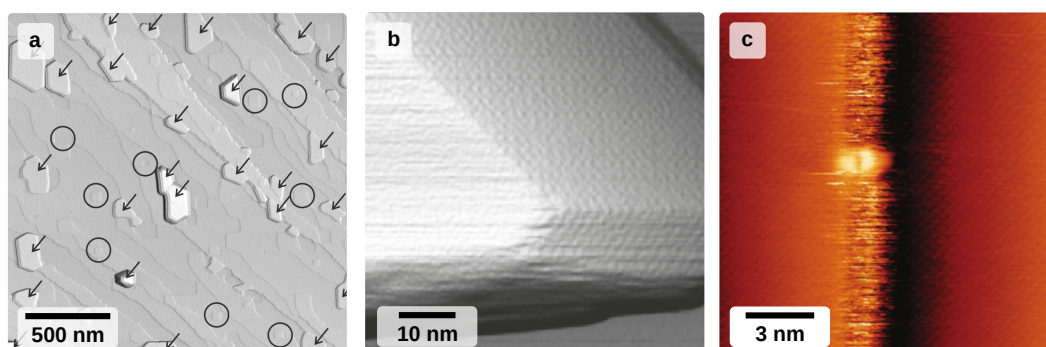


**Fig. 2.5:** Molecular structures on insulating surfaces, illustrating the high molecular mobility. PTCDA on KBr(001) forms clusters shown in **a** and **b** (reprinted with permission from [60], copyright 2005 by the American Physical Society), while syn-5,10,15-tris(4-cyanophenylmethyl)truxene anchors only at kink sites (bright protrusion at the centre of the image) and diffuses rapidly at [010] step edges (reprinted with permission from [80], copyright 2007 American Chemical Society).

many prototypical insulating surfaces has severely hampered the formation of self-assembled molecular structures on insulating surfaces at room temperature. However, the weak molecule-surface interaction can at the same time give rise to qualitatively new structures as it allows access to different energetic relations. We illustrate this point by the formation of complex island morphologies upon  $C_{60}$  deposition on an insulating substrate, shown in Figure 2.6. Qualitatively similar islands are obtained

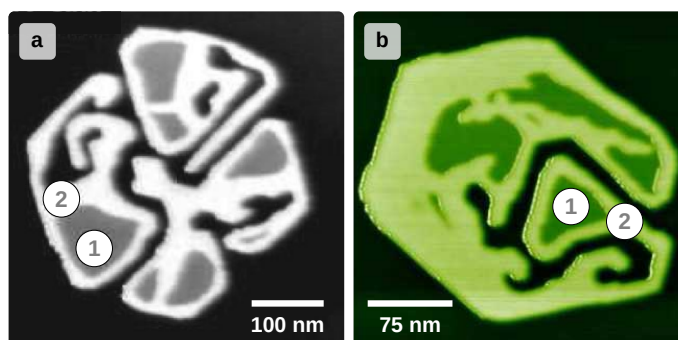


**Fig. 2.6:** Complex island morphologies with unusual shape obtained upon  $C_{60}$  deposition on two different insulating surfaces, namely **a** KBr(001) (reprinted with permission from [67], copyright 2005 by the American Physical Society) and **b**  $CaF_2(111)$  (adapted from [7]). The regions marked with ① are one  $C_{60}$  layer high, the regions marked with ② are twice as high.

regardless whether KBr(001)<sup>[67]</sup> or  $CaF_2(111)$ <sup>[7]</sup> are used, illustrating the generic character of the formation process on weakly interacting insulator surfaces. The unusual island shapes have been explained by a process referred to as "facilitated dewetting", which originates from the weak molecule-surface interaction.<sup>[7]</sup> A specific order of intermolecular interaction strength as well as diffusion and dewetting barrier is required to obtain these islands with the characteristic branched shape, which are absent on metallic surfaces. First when annealing the system to temperatures above room temperature, compact, triangular shaped islands are formed that resemble the *fcc* crystal structure of  $C_{60}$ . The unusual islands can, thus, be identified as a transient non-equilibrium structure, which sets them apart from thermodynamically stable, self-assembled structures. Interestingly, the energetic requirements are not met on metallic surfaces, explaining the absence of these morphologies on these supports.

## 2.3 Studied systems—state of the art

In the following, an overview is given over strategies that have been followed for obtaining self-assembled structures on insulating surfaces that are stable at room temperature. While the interaction of individual molecules with the substrate is discussed in the context of increasing the molecule-surface binding, the focus of this chapter is on the concerted structure formation of many molecules on the

surface rather than on single-molecule studies. Likewise, low-temperature studies are omitted in this chapter in favour of investigations that have been carried out at room temperature.

### 2.3.1 Strategies for anchoring

To benefit from the general design principles, it does not only appear necessary to tune the molecule-insulator interaction in a well-controlled manner, but also to consider the fundamentally different chemistry between organic molecules and insulators compared to the conclusions drawn for molecule-metal systems.

As a consequence, several strategies have been explored for increasing the molecule-surface interaction for molecular self-assembly on insulating surfaces.<sup>[103]</sup> Insulators, however, span a wide range from ionic crystals such as KBr or NaCl to covalently bonded crystals such as diamond or TiO<sub>2</sub> to van-der-Waals bonded molecular solids. Insulating materials can even be formed by several different binding motifs, such as a combination of covalent and ionic interactions in calcite, the most stable modification of calcium carbonate. Thus, general anchoring principles are difficult to obtain for such a heterogeneous class of materials, especially when compared to metallic systems, making this task rather challenging for insulating surfaces.

The surface energy can be considered as a macroscopic parameter for obtaining an estimate for the molecule-surface interaction.<sup>[103]</sup> Surface energies for prototypical metal substrates (ranging from 1000 mJ/m<sup>2</sup> to 2000 mJ/m<sup>2</sup>) are significantly larger than for insulating surfaces (in the order of 100 mJ/m<sup>2</sup> to 600 mJ/m<sup>2</sup>), readily revealing the inertness of most insulating surfaces studied so far. Especially, this parameter is closely linked to the abovementioned dewetting process. Using the C<sub>60</sub> molecule as an example, films adsorbed on low surface energy surfaces have been observed to perform a transition to multilayered and eventually bulk-like structures, while metallic surfaces with large surface energies have been found to confine the molecular film to the first layer.<sup>[107]</sup> Naturally, this consideration does not include the detailed binding geometry at the molecular level, but it reflects the repeatedly reported weak molecule-surface interaction. Thus, although being a macroscopic parameter, considering the surface energy might serve as a first estimate when searching for an appropriate system for molecular self-assembly.

Conceptually, three aspects emerge when aiming for increasing the molecule-surface interaction as summarised in Figure 2.7. The interaction of an individual molecule with the surface might be increased by adding appropriate functional groups such as polar end groups for electrostatic anchoring or functional moieties that offer special binding options such as carboxylic acid groups for hydrogen bonding (see Figure 2.7a). Moreover, for substrate templating the structure of the molecule needs to be optimised with respect to the binding sites on the surface, thus, also the molecule-substrate matching needs to be considered (see Figure 2.7b). Finally,



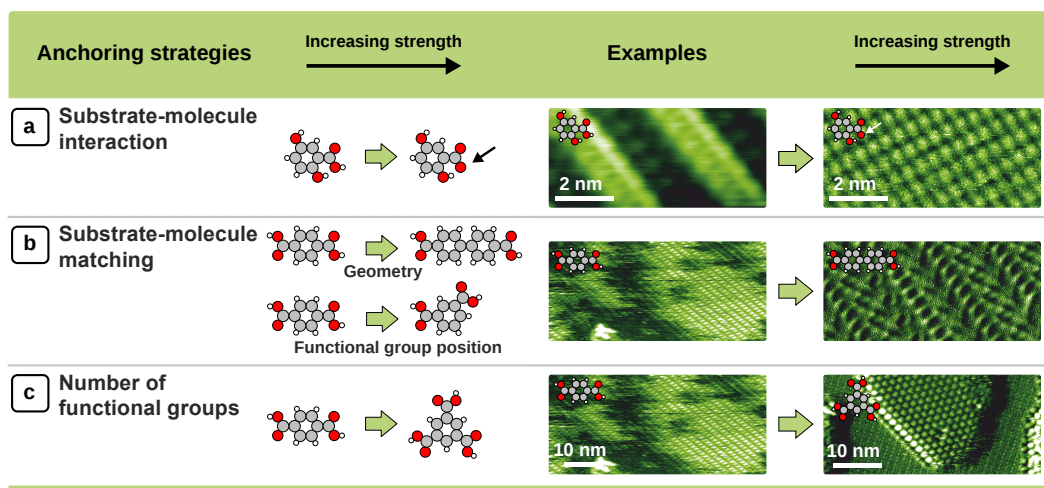


**Fig. 2.7:** Three different strategies for enhancing the anchoring of organic molecules towards a given surface, namely the calcite(104) surface. Adapted from [103].

also the number of the available binding sites is of importance (Figure 2.7c). Although separated conceptually, the three aspects are interlinked and have mutual interdependencies. To give one example, an additive effect is only achieved when the substrate matching is maintained. The mere addition of functional groups can even result in an adverse effect, requiring an additional adjustment of the substrate matching.

### Increasing the molecule-surface interaction

A straightforward and repeatedly approached concept for increasing the interaction of molecules with ionic crystal surfaces is using molecules bearing a high dipole moment, employing polar electrostatic interactions.

This strategy has successfully been applied for identifying a molecule suitable for molecular self-assembly on  $\text{CaF}_2(111)$ <sup>[92]</sup>, namely cytosine. This molecule provides a high dipole moment with the local charges being separated by a distance that corresponds to the distance of a pair of oppositely charged ions in the surface. Consequently, a comparatively high diffusion barrier of approximately 0.5 eV has been estimated for cytosine on  $\text{CaF}_2(111)$  from density functional theory. This value is, however, still too small to provide significant influence of the surface. Interestingly, in combination with the ability of the molecules to form intermolecular hydrogen bonds, trimers that are stable at room temperature have been identified. As apparent from the experiments, these trimers experience a significantly increased diffusion barrier, which is in this case approximately three times as high as the diffusion barrier of the individual molecules, as the three-fold symmetry of the substrate allows for maintaining the optimum adsorption position even when assembled in the rather rigid trimer structure. This example readily illustrates a cooperative effect in

anchoring organic molecules on to surfaces, which involves the molecule-surface and intermolecular interactions as well as the mutual impact of two interactions on each other. The latter aspect is difficult to estimate *a priori*, but can have significant influence on the resulting force balance.

Another interesting study involving four different helicene derivatives with one or two bromo or cyano groups on the Suzuki(001) surface<sup>[91]</sup> readily displays the complexity of anchoring molecules to an ionic surface. While the dibromo derivative is expected to bind stronger to the surface than the monobromo derivative, the opposite is observed experimentally. The dibromo molecule desorbs from the surface within few hours after deposition, while the monobromo derivative remains on the surface. This is explained by charge mismatch, because the Br-Br distance in the molecule does not fit to the Na-Na distance on the surface. Additionally, the dibromo molecules bind vertically to the surface. Although a decrease of the desorption barrier has been calculated for this vertical geometry, the molecule-molecule interaction is in turn increased as this geometry allows the dibromo molecules to self-assemble *via* intermolecular  $\pi$ - $\pi$  stacking. Also the cyano derivatives adsorb in a vertical position. In this case, the dicyano molecule binds stronger than the monocyano, because the charge distances match to the corresponding distances on the surface. However, the vertical adsorption geometry of the molecules still lowers the desorption barrier compared to a horizontal adsorption geometry. Consequently, desorption is observed after a few weeks. In conclusion, the molecule with the weakest dipole (monobromo) is paradoxically the one with the largest desorption barrier.

This example readily demonstrates that a simple model estimating desorption barrier by counting the anchor groups and taking into account their dipole moments can be wrong as even minute effects can severely alter the expected binding. The interaction is expected to significantly increase in strength if not only polar molecules are present, but if molecular ions are employed.<sup>[83,104]</sup> An example that is ascribed to this anchoring mechanism is 4-iodobenzoic acid on the (104) cleavage plane of calcite<sup>[104]</sup>, as shown in Figure 2.8. Upon deposition, the molecules are expected to be protonated and, thus, overall charge neutral with only little interaction with the surface. NC-AFM data have revealed a rapid molecular diffusion on the surface, *i.e.*, no islands are found except for situations in which molecules are trapped in a confined geometry. This situation is changed drastically when the sample is annealed. After this annealing step, an extended wetting layer has been observed. The internal structure of this wetting layer can be understood when considering the molecules to be deprotonated. In the deprotonated state, the molecules are expected to stand upright as this allows for increasing the molecule-surface interaction significantly by electrostatic anchoring of the negatively charged carboxylate groups with the surface calcium cations. The upright position also allows for the formation of intermolecular  $\pi$ - $\pi$  bonds, further stabilising this arrangement.

Apart from anchoring based on electrostatics, more specific binding motifs can be used. A prominent example is hydrogen bonding between the molecular layer and the

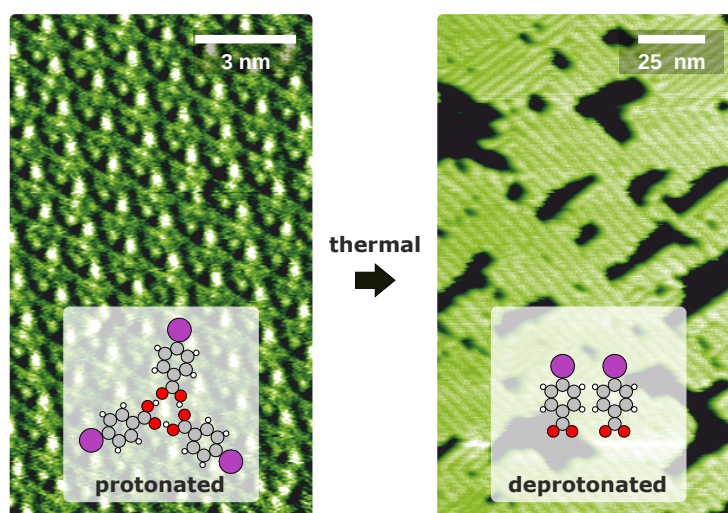


**Fig. 2.8:** Activation of substrate templating ascribed to deprotonation. 4-iodobenzoic acid on calcite(104) transforms to an upright-standing geometry with an additional increased anchoring that is ascribed to deprotonation. Adapted from [104].

substrate, *e.g.*, when depositing carboxylic acid or hydroxyl groups on to a surface that provides sites for hydrogen bond formation. This situation has been reported for carboxylic acids on calcite. In this molecule-surface system, hydrogen bonds can be formed between the hydrogen atom of the molecular carboxylic acid group and the oxygen atom of the surface carbonate group. Interestingly, the adsorption of biphenyl-4,4'-dicarboxylic acid (BPDCA) on calcite(104) results in the coexistence of two different structures.<sup>[98]</sup> One of which closely resembles the molecular bulk structure with a head-to-tail arrangement of the molecules, forming hydrogen-bonded molecular chains on the surface (see Figure 2.9a ①). The fact that a bulk-like structure is

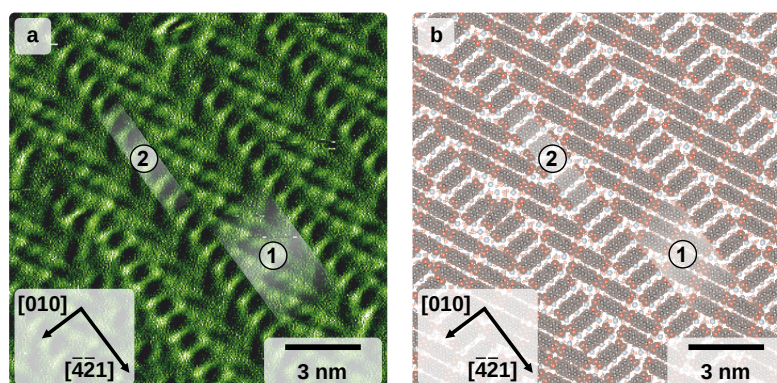


**Fig. 2.9:** Coexistence of a bulk-like structure ① and a substrate-templated structure ② of BPDCA on calcite(104). AFM image **a** with structural model **b**. Adapted from [98].

formed indicates the marginal influence of the underlying substrate on this pattern. Besides the bulk-like structure, however, a clearly substrate-templated assembly is revealed with the molecules arranged in a side-to-side fashion (Figure 2.9a ②). This latter structure can be understood by anchoring of the molecules towards the surface with the carboxylic acid groups possibly forming hydrogen bonds with the

surface carbonate groups. The coexistence of both structures at room temperature clearly indicates that the two structures are energetically very close, *i.e.*, the system constitutes an example showing the transition from molecular bulk crystal formation towards increasing substrate templating.

The molecule-surface interaction motifs described so far are of rather unspecific electrostatic nature (ionic and polar molecules on ionic substrates) or include an uncertain contribution of hydrogen bonding. For a rational design of complex self-assembled structures on insulators it will be mandatory to explore and utilise the bonds of high directionality and selectivity enlisted in Table 2.1 to a higher degree in future work.

### Optimising the molecule-surface matching

Besides the detailed nature of the molecule-surface interaction, obviously the geometric matching of the molecular structure to the substrate needs to be considered. This can be readily seen by comparing the structures formed by terephthalic acid (TPA) and BPDCA<sup>[98]</sup> on calcite(104). While the latter molecule forms both, a substrate-templated structure and a bulk-like structure as shown in Figure 2.9, the only motif found for the TPA molecule is basically molecular chain formation following the bulk arrangement. Introducing a further benzene ring as in BPDCA is expected to cause a different binding situation to the substrate while leaving the molecule-molecule interaction in the chain arrangement rather similar. With a different separation between the functional groups, the molecule can now attain an adsorption position in which both carboxylic acid groups can form hydrogen bonds towards the surface carbonate groups. The single-molecule adsorption geometry in the substrate-templated structure (denoted ② in Figure 2.9) is understood to allow for a stronger molecule-surface bond compared to the situation in the bulk-like assembly (denoted ① in Figure 2.9).

The importance of molecule-surface matching has also been shown by the comparison of anchor groups for the already mentioned helicene derivatives.<sup>[91]</sup> While the distance between two cyano groups fits to the substrate, the dibromo derivative has a shorter distance between the anchor groups, which reduces the binding energy noticeably.

### Increasing the number of functional groups

A straightforward strategy to increase the molecule-surface interaction is increasing the number of functional groups available for interaction with the surface. Using the calcite(104) surface as the supporting substrate, this strategy has been followed by changing the number of carboxylic acid groups from two as in TPA to three

as in trimesic acid (TMA).<sup>[100]</sup> In this example, the addition of a third carboxylic acid group has changed both, the intermolecular as well as the molecule-surface interaction, which is illustrated in the very different structures observed for TMA. However, as mentioned above, the effects of the functional groups are generally non-cumulative, as a cross-dependence with the surface matching needs to be considered. When positioned above a different surface site, the additional functional group might not bind similarly strong towards the surface as the first one. In fact, even a repulsive interaction can be envisioned, resulting in an adverse effect. We note that the flexibility of the functional groups can have a second cross-effect on the effective molecular diffusion barrier; the effective diffusion barrier is not necessarily the sum of its constituents.<sup>[108]</sup>

### 2.3.2 Decoupling molecule-surface and intermolecular interactions

For controlling the structure formation upon self-assembly, decoupling the intermolecular from the molecule-surface interaction is desired for tuning the involved interaction energies. This is not an easy task as changing the intermolecular interaction does generally also affect the molecule-surface interaction. Therefore, it is of utmost relevance to identify and design molecular building blocks that allow for decoupling the intermolecular from the molecule-surface interaction to a large extent. In the first place, this is a synthesis task, making use of the impressive flexibility and variability of organic chemistry.

As an example, a molecular class with a rather similar binding towards calcite(104) is considered, namely oligo(*p*-benzamide) molecules.<sup>[101]</sup> These molecules feature two iodine atoms with a distance of approximately 1.35 nm (see Figure 2.10a). Being electronegative, these two iodine atoms are expected to be electrostatically attracted

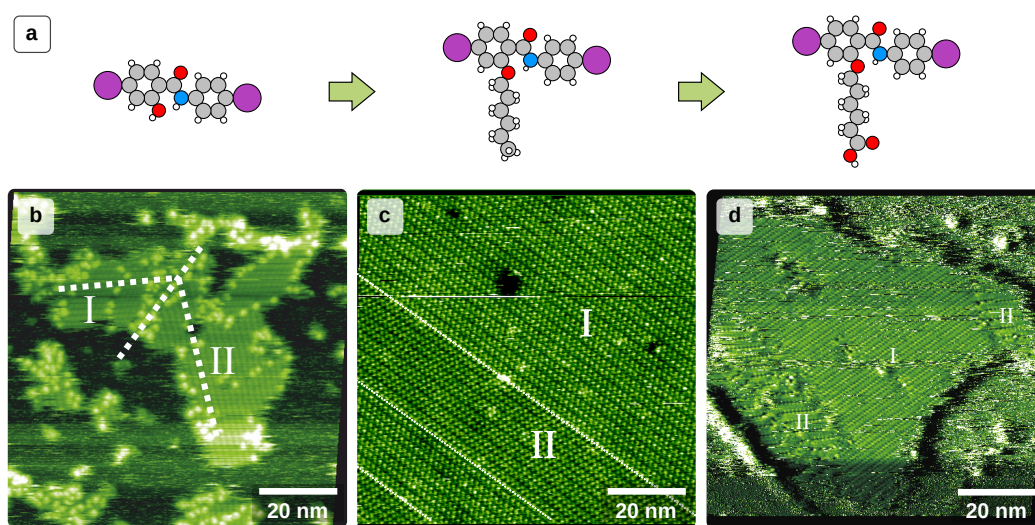


**Fig. 2.10:** Oligo(*p*-benzamide) molecules on calcite(104) as an example of similar molecule-surface interaction while varying the molecule-molecule interaction.<sup>[101]</sup>

to the surface calcium cations. Thus, an effective anchor is provided that results in well-defined adsorption positions of the molecules on the surface. The intermolecular interaction, on the other hand, can be controlled by side groups that are varied in a systematic manner. Interestingly, distinctly different molecular structures can be obtained that are governed by the respective side groups, as shown in Figure 2.10b to d. Consequently, a variation in molecular structures can be achieved by designing the respective side groups, despite the identical adsorption mechanism. This example, thus, illustrates the successful decoupling of the molecule-surface interaction from the intermolecular interaction.

## 2.4 Outlook

Despite being a comparatively young research field, molecular self-assembly on insulating surfaces has developed tremendously during the last decade. This is partly due to the impressive improvements of the main experimental tool, namely non-contact atomic force microscopy. On the other hand, the library of functional organic molecules is increasing steadily, providing a plethora of options for novel structural motifs.

Extensive effort has been made to gain precise control over the resulting structure. This control includes the control of structural parameters such as molecular orientation, symmetry and island sizes, to name but a few. Eventually, these efforts aim for converting the structural control into application-oriented functionality. Structures relevant for application will require sufficient stability in a given temperature window as well as dedicated properties that include, *e.g.*, switchability and stimuli-responsive effects. These future demands will push forward the development of steadily increasing structural control, providing the route towards more advanced and complex structures. Promising strategies to be followed in future will include a concerted action of both synthesis efforts and a clever design of the system and the deposition protocol. A key synthesis task is providing building blocks that offer a high degree of flexibility while at the same time allowing for a well-defined decoupling of intermolecular and molecule-surface interactions. On the surface science experimental side, increasing complexity by codeposition and exploring the potential of various deposition protocols will enhance structural variability. An important aspect of this development includes a precise characterisation and quantification of the involved energies and barriers.

Finally, a major challenge of future efforts is transferring the gained knowledge to the liquid/solid interface, which will be of tremendous relevance for applications. A key question to be answered here concerns the role of the solvent in molecular self-assembly at the solid/liquid interface.

# Frequency-modulation atomic force microscopy

Probing molecules on an insulating surface is often more difficult than on a conductor or semiconductor, because methods like scanning tunnelling microscopy cannot be utilised (see Chapter 2). The experiments of this thesis were performed with a non-contact atomic force microscope. A detailed review of this technique can be found elsewhere.<sup>[109]</sup> The focus of this chapter is on giving a short comprehensive introduction to frequency-modulation atomic force microscopy (FM-AFM) and to clarify questions raised during the course of this thesis.

## 3.1 Basic principle

The idea behind FM-AFM is to monitor the oscillation of a tiny leaf spring called cantilever with an atomically sharp tip at its end while being close to a sample surface. To excite the cantilever, it is connected to a shaking piezo oscillating at the frequency with the largest amplitude response, called resonance frequency.<sup>a</sup> Making use of the fact that interactions between the tip and a sample change the resonance frequency noticeably, it is possible to measure structures at the atomic scale.

To understand why and how the resonance frequency of a cantilever changes if there is interaction with the sample, we can assume the following: the restoring force of the free cantilever (no tip-sample interaction) can be described using Hooke's law:

$$F_{\text{free}} = F_{\text{Hooke}} = m^* \cdot \ddot{x} = -k^* \cdot x \quad (3.1)$$

with the effective mass  $m^*$  and the effective spring constant  $k^*$  reflecting the geometry and material of the cantilever.<sup>b</sup> A solution of this equation is

$$x_{\text{free}}(t) = A \cdot \sin(\omega t) \quad (3.2)$$

---

<sup>a</sup>A free oscillating cantilever can be compared to a ruler clamped to a table so that part of its length projects from the edge of the table. It starts to oscillate if the free end is pressed downwards and released. The frequency at which it is oscillating is the resonance frequency and is determined purely by the material and geometry of the free end. The dependence on geometry can be readily seen by changing the length of the free end.

<sup>b</sup>This equation does not include damping, which is negligible for the experiments in this thesis, because they were conducted in ultra-high vacuum.

with the amplitude  $A$  and the angular frequency  $\omega$ . Putting this solution into the differential equation yields the resonance frequency<sup>c</sup>

$$\omega_{\text{free}} = \sqrt{\frac{k^*}{m^*}}. \quad (3.3)$$

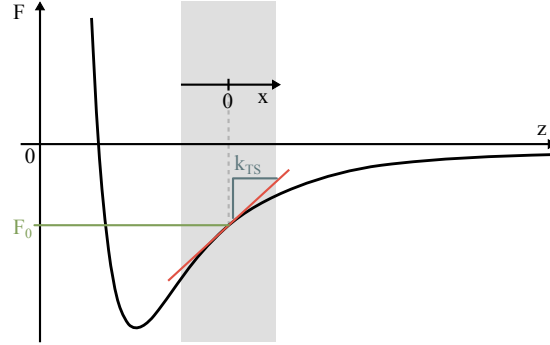


**Fig. 3.1:** Schematic drawing of the rough approximation used to determine the frequency shift resulting from an interaction of the tip with a sample for a typical force-distance curve. The tip is oscillating in the region marked with the grey box and  $F_{\text{TS}} \approx F_0 + k_{\text{TS}} \cdot x$ . This approximation is only good for very small amplitudes and the difference between true force (black line) and approximation (red line) is already large in this example.

If there is interaction with the sample, the force between the tip and the sample  $F_{\text{TS}}$  can be roughly approximated about  $x = 0$  by using the Taylor series truncated to two terms as illustrated by Figure 3.1:

$$F_{\text{TS}} \approx F_0 + k_{\text{TS}} \cdot x \quad (3.4)$$

with the slope  $k_{\text{TS}}$  of the tip-sample force at  $x = 0$  and the tip-sample force  $F_0$  at  $x = 0$ . The new total force on the cantilever is accordingly:

$$F = F_{\text{Hooke}} + F_{\text{TS}} = -k^* \cdot x + F_0 + k_{\text{TS}} \cdot x \quad (3.5)$$

The differential equation can then be written as

$$m^* \cdot \ddot{x} = -(k^* - k_{\text{TS}}) \cdot x + F_0. \quad (3.6)$$

A solution of this differential equation is now

$$x(t) = A \cdot \sin(\omega t) + \frac{F_0}{k^* - k_{\text{TS}}}. \quad (3.7)$$

<sup>c</sup>This is the resonance frequency without damping, which is called eigenfrequency. However, because the damping is low for the experiments in this thesis, the eigenfrequency is a very good approximation for the resonance frequency.



While  $F_0$  only leads to a static deflection (the second addend does not depend on time) of the cantilever, inserting Equation 3.7 into Equation 3.6 yields that the force gradient  $k_{\text{TS}}$  changes the resonance frequency to

$$\omega = \sqrt{\frac{k^* - k_{\text{TS}}}{m^*}} \quad (3.8)$$

(see appendix, Section 10.1). Thus, it is the change of the restoring force due to the interaction between the tip and the sample that changes the resonance frequency. In the region displayed in Figure 3.1, the interaction leads to a decrease in the resonance frequency. Consequently, the resonance frequency decreases first if approaching the sample and increases if being closer to the sample. This general trend holds true, even though the experiments in this thesis were performed with a way larger oscillation amplitude than depicted in Figure 3.1 where the linear approximation for the force is even worse. The relation between tip-sample force (or force gradient) and frequency shift is more complicated then.<sup>[109]</sup> Graphs displaying the relation between force, force gradient and frequency shift can be found in [110].

In the next section, the practical realisation of this concept is explained.

## 3.2 Setup

To perform FM-AFM measurements, the setup outlined in Figure 3.2 is used. The cantilever ① is driven by a shaking piezo and oscillates at its resonance frequency. For monitoring the movement of the tip, a laser beam ② is shed on the back of the cantilever. The reflection is monitored by a position sensitive detector (PSD) ③ which consists of at least two segments and produces a signal related to the intensity difference between upper and lower segments. This signal is then used to determine the oscillation amplitude, which is kept constant by a feedback loop ④ that determines the amplification of the excitation signal ⑥ for the shaking piezo. This amplification is called dissipation and indicates the energy loss caused by interaction with the sample during measurements. Usually, there is little contrast in the dissipation channel during FM-AFM measurements.

Of utmost importance is a precise determination of the resonance frequency. This is done by a phase-locked loop (PLL) ⑤ that consists of a voltage-controlled oscillator

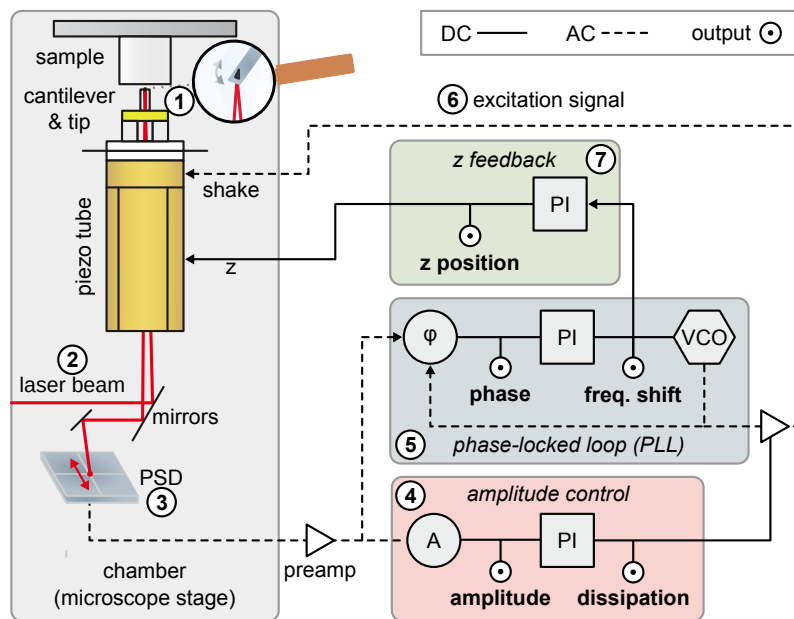


**Fig. 3.2:** Schematic drawing of the FM-AFM setup. A very small tip is mounted on an oscillating cantilever ① that is in vicinity of a sample. The oscillation of the cantilever changes upon interaction between the tip and the sample and is detected with a laser beam ② focussed on the back of the cantilever. The reflected beam travels via mirrors to a position sensitive detector (PSD) ③. The signal of the PSD is amplified by a preamplifier. An amplitude control ④ measures the amplitude  $A$  of this signal and a feedback loop compares it with a setpoint and determines the amplification (dissipation  $\Gamma$ ) of the excitation signal ⑥ for the cantilever which is fed to a shaking piezo. To measure the current resonance frequency, a phase-locked loop (PLL) ⑤ is used. Its voltage-controlled oscillator (VCO) produces the excitation signal ⑥ for the cantilever. The detected frequency shift  $\Delta f$  is passed to another feedback loop ⑦ that keeps the frequency shift constant by changing the distance between the tip and the surface ( $z$  position) by varying the voltage applied to the piezo tube.

(VCO), a phase detector and a feedback. The VCO generates a signal with a frequency proportional to the applied voltage. This signal is then compared to the signal from the PSD by determining the phase difference and the feedback regulates the voltage applied to the VCO to keep the phase difference constant. Thus, the applied voltage corresponds to the frequency of the incoming signal. A frequently asked question is why the phase is used to determine the difference in frequency. This is explained by the following example: assume you drive with a car and want to drive at the same speed as the car in front, even if you do not know the velocity of the other car. You can accomplish that by keeping the distance to the car in front constant. This way it is possible to determine the speed of the other car by looking at your own tachometer. That is basically what the PLL is doing (Figure 3.3). Corresponding to the distance, the PLL determines the phase difference between the

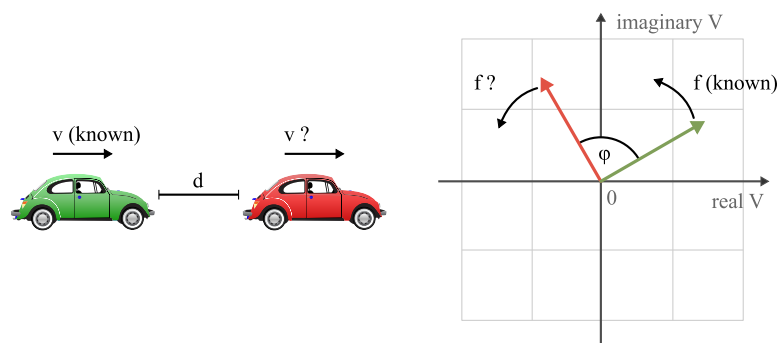


**Fig. 3.3:** Comparison between determination of the speed of another car and the determination of frequency in a PLL (see text). On the right side, the voltage of the VCO (green arrow) and of the signal from the PSD (red arrow) are displayed in the complex plane. The speed  $v$  of the car corresponds to the frequency  $f$  which is proportional to the rotation speed of the arrow. The distance  $d$  between the cars corresponds to the angle between the arrows, that is the phase difference  $\varphi$ . For keeping the phase constant, a feedback loop regulates the frequency of the VCO.

reference signal from the VCO and the incoming signal of the PSD. In Figure 3.3, the voltage of both signals is displayed with arrows in the complex plane and the phase difference corresponds to the angle between those arrows. The frequency is proportional to the rotation speed of the arrows. If the arrow representing the PSD signal is rotating faster (higher frequency), the angle will get larger (larger phase difference) and the feedback will speed up the VCO signal (and the other way around).

To keep track of the PSD signal, the VCO needs to be set to the resonance frequency of the cantilever at the beginning. Otherwise, the VCO would be for instance way too slow and the phase difference would become  $> 180^\circ$ , which would be interpreted as  $> -180^\circ$ . The VCO would then decrease the frequency instead of increasing it and never find the right frequency (lock out).

Not only does the PLL determine the frequency shift, it also generates a low-noise signal with the actual resonance frequency with its VCO. This signal is used for the excitation of the cantilever (Figure 3.2 ⑥), since the cantilever needs to be excited

at its resonance frequency.

In order to keep the interaction between the tip and the sample constant, the frequency shift is kept constant by a feedback loop (7) that regulates the height ( $z$  position) of the tip by applying a voltage to the piezo tube. If the feedback loop is working properly, the  $z$  channel image corresponds to a plane of constant frequency shift.

### 3.3 Feedback loops

At this point, something about feedback loops should be said, because false statements can be found in literature. First of all, there are two types of gains being used commonly for a feedback loop, namely integral (I) and proportional (P) gain.

*The integral gain is essential to tracking the surface. (It's easy to remember that, if you call the "I" gain the "important" gain.)*

*from the MFP-3D manual*

The I-gain does exactly what you expect a feedback to do. It looks at the difference between setpoint and actual value (error  $e$ ) and increases or decreases the output  $y$  proportional to the parameter  $k_I$ :

$$y_I(t) = \int_0^t k_I(\tau) \cdot e(\tau) \, d\tau. \quad (3.9)$$

Note that this equation takes into account that  $k_I$  may be changed during measurement and is, therefore, inside the integral. In an electronic circuit, the integration could be a capacitor being charged or uncharged. That is why the integral really starts at zero, that is at the time the feedback is switched on. A simple numerical simulation of a distance feedback loop moving a tip over the surface and keeping the distance constant is shown in Figure 3.4 for different values for  $k_I$ .<sup>d</sup> Note that for an actual AFM experiment the relation between change in resonance frequency and height of an object depends on the frequency shift setpoint. If being closer to the sample, the tip is usually more sensitive (the slope of the  $\Delta f$  vs.  $z$  curve is higher) and small protrusions cause large changes in frequency shift. That means that  $k_I$  needs to be set to small values if being close to the sample.

The P-gain is rather unintuitive, because it produces an output proportional to the error:

$$y_P(t) = k_P(t) \cdot e(t). \quad (3.10)$$

That means that if there is no error, the output is zero, which is usually not intended. Also there is typically no relation between error and a useful control value. Therefore,

---

<sup>d</sup>If starting a simulation, the initial tip position should be set by giving the integral a start value.

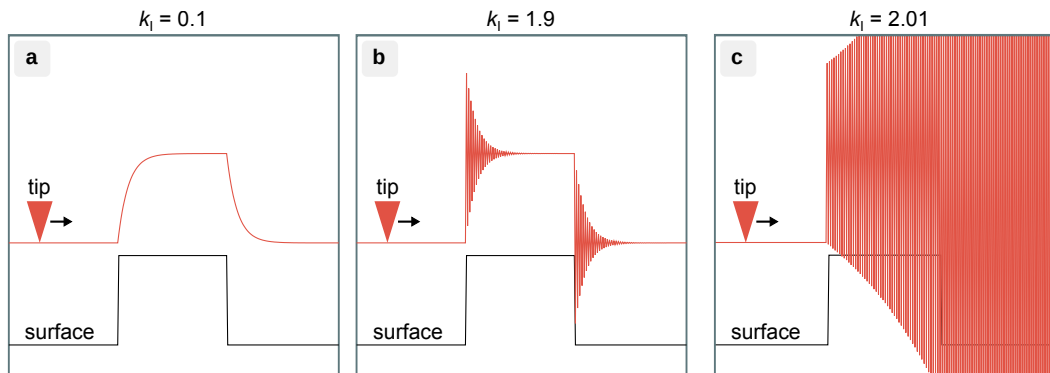


**Fig. 3.4:** Simulation of a distance feedback loop with an integral part only. Here  $k_I = 1$  is the perfect value instantly compensating the error. The graphs show plots of the tip movement for  $k_I = 0.1$  (a),  $k_I = 1.9$  (b) and  $k_I = 2.01$  (c). The curve for  $k_I = 1$  would be identical to the surface curve (shifted by the distance setpoint). One way to tune a feedback loop is to increase  $k_I$  until the feedback loop starts to overshoot ( $k_I \approx 2$ , illustrated in c) and to use half of this value for  $k_I$ .

a pure proportional controller could not be used for a  $z$  feedback in an AFM, because approaching the sample is impossible (it will measure a frequency shift error, but this does not tell how far the surface is away and because the error is always the same if being far away, the controller would set some position proportional to  $k_P$  and just stay there). However, if the output of the feedback is the sum of a I- and P-gain, the P-gain may help if there are quick changes such as spikes in topography. In any case, the value of the P-gain should be smaller than the value for the I-gain and can also just be set to zero.

Surprisingly, there is dissension in the community about feedback loops. An interesting paper describes how the P-gain leads to instabilities and, thus, assumes that its output is summed up, effectively turning the P-gain into an I-gain.<sup>[111]</sup> Some investigations of the author of this thesis revealed that this is not the case. At least three manufacturers, namely *Omicron*, *Asylum Research* and *Keysight*, use the feedback output directly as  $z$  position without summing up. *Omicron* even allows only to change the value of the I-gain in their *Matrix* software. The I-gain is the *important* gain for the distance feedback indeed.

So when is the P-gain important? If the response of the system is slow, that is a change of the feedback output does not change the measured value instantly, the P-gain is needed to react quickly. A good example is a temperature controller connected to a heater and monitoring the temperature. It normally takes time until the temperature changes and the I-gain needs to be set low to give the system time to react. This way, the feedback will slowly reach the perfect average heating value. However, the feedback should still react quickly to fast temperature fluctuations after reaching this heating value. This is exactly where the P-gain comes into play, because it just adds some additional output to the I-gain control value.

## 3.4 The instrument

Experiments were conducted using a *VT AFM XA* from *Omicron*, Taunusstein, Germany. A detailed description of the setup can be found in [112]. The pressure during measurements was around  $1 \times 10^{-11}$  mbar. The system was cooled using the built-in flow cryostat with liquid nitrogen or liquid helium. Cantilevers made of n-doped silicon with a resonance frequency around 300 kHz were used. Before usage, cantilevers were sputtered with  $\text{Ar}^+$  for 10 min. The oscillation amplitude during measurements was kept around 10 nm. KPFM<sup>[113]</sup> measurements were performed using an *HF2LI* lock-in amplifier from *Zurich Instruments*, Zürich, Switzerland. A voltage modulation signal with a frequency  $f_{\text{mod}}$  of 987 Hz and an amplitude of 1 V was applied to the tip. Using an internal feedback loop of the *HF2LI*, the amplitude of the  $\Delta f$  signal at  $f_{\text{mod}}$  (the error signal  $\Delta V_{\text{fm}}$ ) was minimised by changing the external voltage ( $V_{\text{fm}}$ ) applied to the tip.

Calcite crystals were purchased from *Korth Kristalle*, Altenholz, Germany and cut in blocks with a surface area of  $2 \text{ mm} \times 4 \text{ mm}$  by *Vario Kristallbearbeitung*, Königs Wusterhausen, Germany. The crystals were degassed *in situ* for 2 h to 5 h at about 550 K. After each *in situ* cleaving, the crystal was annealed to about 500 K to remove surface charges. Molecules were evaporated using a home-built Knudsen cell.

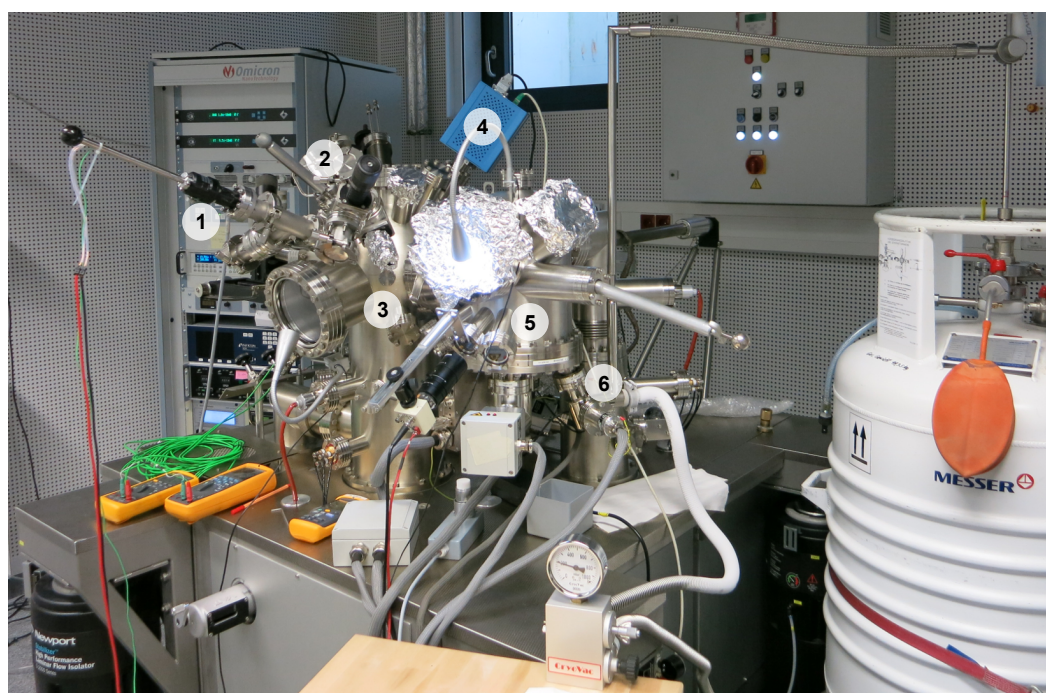
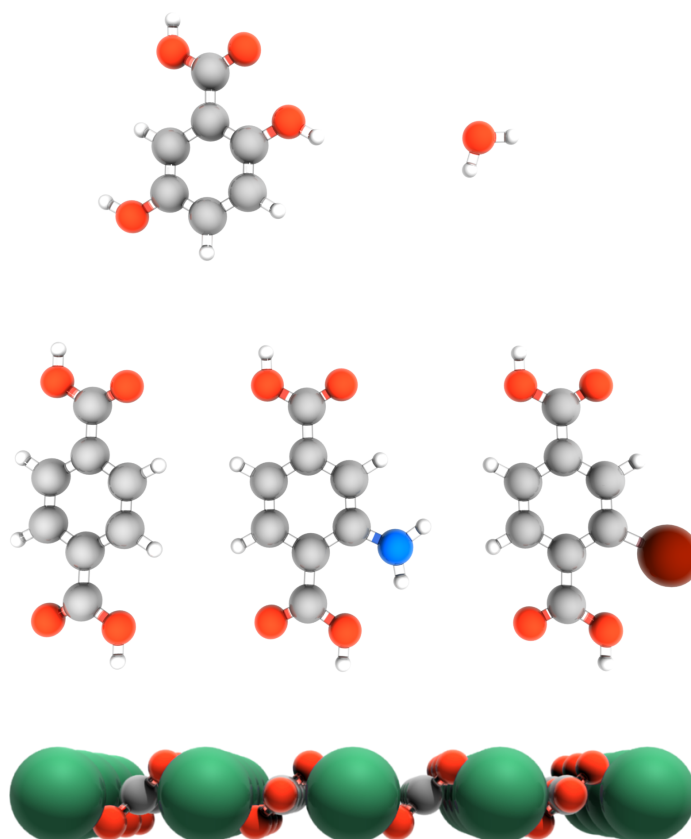


**Fig. 3.5:** Photograph of the measurement chamber during experiments performed for this thesis requiring cooling with liquid helium. ①: molecule evaporator, ②: scalpel for *in situ* cleaving of crystals, ③: analysis chamber with manipulator inside, ④: mass spectrometer, ⑤: AFM chamber, ⑥: cryostat.

## Substrate and molecules

Selecting a proper molecule-substrate system for imaging molecular self-assembly is not an easy task. Especially for experiments at room temperature, the molecules need to stick well to the surface. In the case of an insulating surface, the interaction between molecules and surface is in general weaker than between molecules and a metal surface, which makes this task more difficult.



## 4.1 The calcite(104) surface

In this thesis, all experiments were conducted on the insulating calcite(104) surface (Figure 4.1). Calcite is the most stable modification of  $\text{CaCO}_3$  and the  $\{104\}$  planes

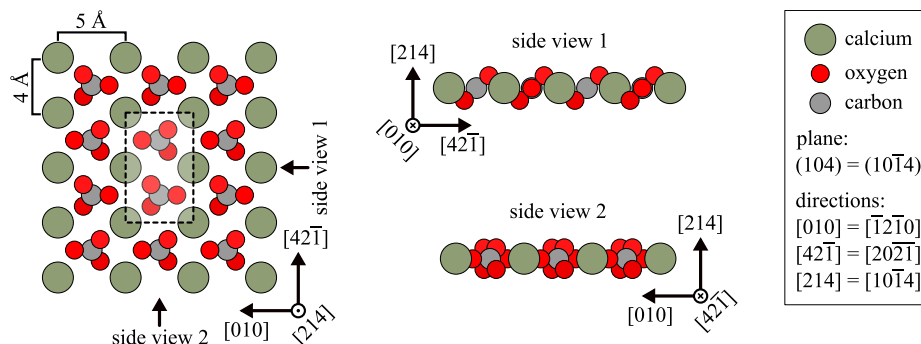


**Fig. 4.1:** Model of the calcite(104) surface. The unit cell is marked with a dashed box. The unit cell dimensions are  $5.0 \times 8.1 \text{ \AA}^2$ . Besides the top view, two side views are shown to point out the tilt of the carbonate groups (side view 1). The orientation of a calcite crystal is determined prior to locking in a crystal to the UHV chamber by looking for a double refraction, because calcite is birefringent. When looking perpendicular to the (104) surface, the extraordinary ray points to the direction of the carbonate tilt, which is the  $[42\bar{1}]$  direction. In this thesis, three indices are used to describe directions and planes. The corresponding symbols with four indices are shown in the box on the right side.

are the most stable cleave planes. The main symmetry directions of the calcite(104) surface are  $[010]$  and  $[42\bar{1}]$ .<sup>a</sup> More about the calcite(104) surface can be found in [114] and [115].

<sup>a</sup>It needs to be mentioned that the unit cell of a calcite crystal is hexagonal and Weber symbols may be used alternatively to describe directions. The correct Weber symbols of the  $[010]$  and  $[42\bar{1}]$  directions are  $[\bar{1}2\bar{1}0]$  and  $[20\bar{2}\bar{1}]$  respectively.<sup>[114]</sup> Symbols with a point instead of the third index can be found in literature as well. These are highly misleading, because the point is sometimes interpreted as a zero and sometimes as third index of the Weber symbols (where the third index is the negative sum of the first two). A common mistake is to calculate Weber symbols by using the negative sum of the first two indices as third index. In general this is wrong and false symbols such as  $[01\bar{1}0]$  and  $[426\bar{1}]$  for calcite(104) are the result. Weber indices allow for a quick identification of equivalent directions and account for the hexagonal symmetry. Hence, they should be preferred to directions with three indices. However, to avoid confusion due to false Weber indices and because most literature uses three indices, this thesis does so as well.



## 4.2 The molecules

It has been found that many carboxylic acids anchor well to the calcite(104) surface, that is the molecules do not desorb at room temperature. This is explained by the strong interaction of the oxygen atoms of the carboxylic acid group with the calcium ions on the one hand and the possibility to form hydrogen bonds with the carbonate ions on the other hand. Therefore, four of five molecules in this thesis are carboxylic acids. Besides some experiments at room temperature, most measurements in this work were conducted at low temperatures. Hence, it was also possible to image water on calcite, which desorbs at room temperature. The chemical structures of the organic molecules probed in this thesis are depicted in Figure 4.2.

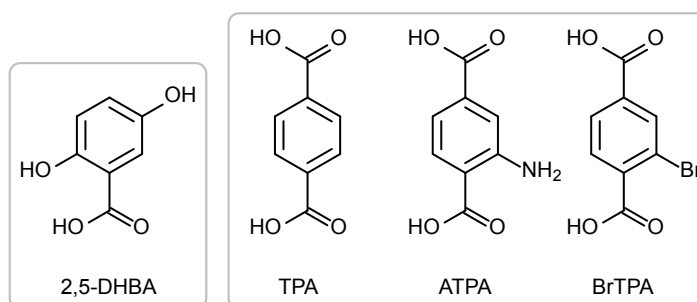


**Fig. 4.2:** Structures of the organic molecules used in this thesis. From left to right: 2,5-dihydroxybenzoic acid (2,5-DHBA), terephthalic acid (TPA), 2-aminoterephthalic acid (ATPA) and 2-bromoterephthalic acid (BrTPA).

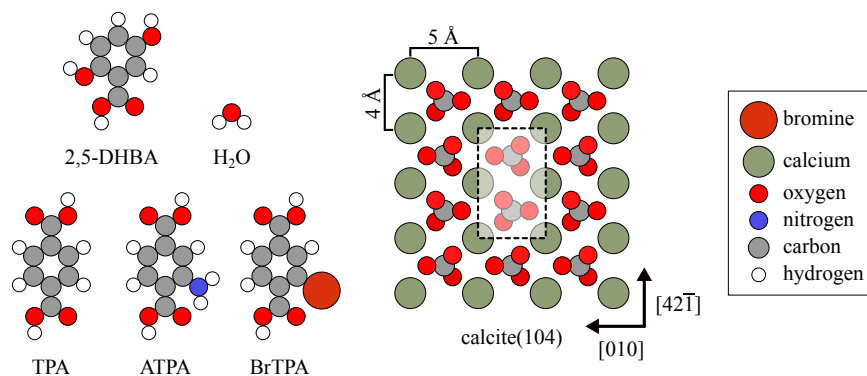


**Fig. 4.3:** Schematic true-to-scale drawing of the molecules and the calcite(104) surface.

Figure 4.3 shows a true-to-scale schematic drawing of the molecules and the calcite(104) surface. Except for water, all molecules have been imaged with FM-AFM on calcite(104) in UHV before: 2,5-DHBA by Markus Kittelmann<sup>[23]</sup> and Simon Aeschlimann<sup>[116]</sup>, TPA by Philipp Rahe<sup>[100,115]</sup> and ATPA and BrTPA by Christopher Hauke<sup>[112]</sup>.

H<sub>2</sub>O (*Milli-Q* water) was degassed with pump-freeze-thaw cycles and dosed opening a fine control valve.<sup>[117]</sup> The other molecules were deposited using a Knudsen cell.

Prior to attaching the molecule evaporators to the AFM chamber, sublimation experiments with *Justin* (Section 5.3) were performed for finding a proper sublimation temperature. The sublimation enthalpies are listed in Table 4.1 (for the Arrhenius plots see appendix, Section 10.2). 2,5-DHBA did not stick to the QCM and, thus, no sublimation enthalpy could be measured.

The measurements of 2,5-DHBA can be found in Chapter 6, those of TPA and its derivatives in Chapter 7 and the water measurements in Chapter 8.

**Tab. 4.1:** Properties of the organic molecules probed in this thesis. All molecules were purchased from *Sigma Aldrich*.

molecule	IUPAC name	purity	$\Delta H_{\text{sub}}$ in $\text{kJ mol}^{-1}$
2,5-DHBA	2,5-dihydroxybenzoic acid	> 99 %	(no rate measured)
TPA	terephthalic acid	$\geq$ 99 %	$176 \pm 12$
ATPA	2-aminoterephthalic acid	99 %	$195 \pm 13$
BrTPA	2-bromoterephthalic acid	95 %	$222 \pm 26$

## Data processing

In this chapter, three selected self-written software programs are explained, namely *TrackRead* (a program for post-processing of diffusion measurements) in Section 5.1, *I12c* (a tool for instrument calibration and drift correction) in Section 5.2 and *Justin* (for performing fully automated sublimation experiments) in Section 5.3. A list of software written during the thesis can be found in the appendix.

### 5.1 TrackRead—processing motion tracking data

*TrackRead* is a software to compensate drift using motion tracking data (see Section 6.3) from diffusion measurements.

#### 5.1.1 Image preparation

To evaluate an image series, the images are transformed to compensate for drift. This is done by selecting three characteristic points *A*, *B* and *C* in the last image as reference and using the self-written software *I12c* (Section 5.2) to determine the transformation matrix for each other image by marking these three points. Then the images are put on top of each other and cropped to the area they have in common.

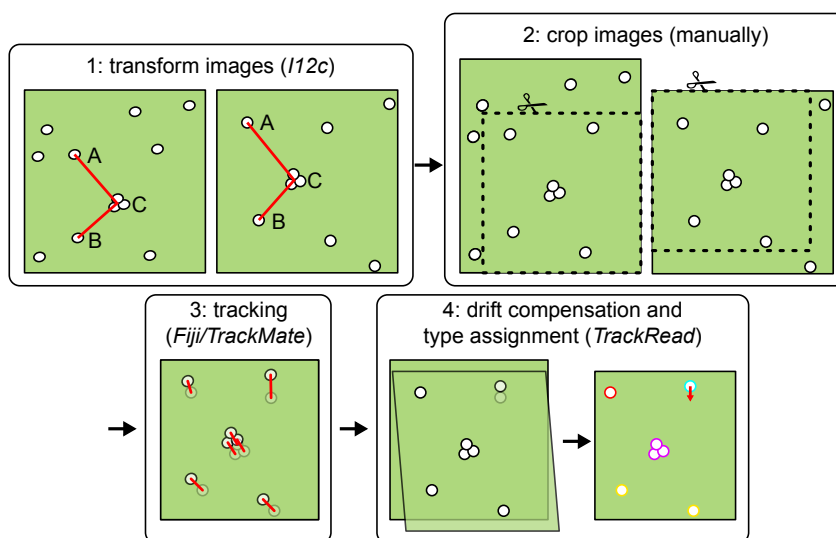


**Fig. 5.1:** Schematic drawing of the data processing of image series from diffusion measurements.

This is illustrated by Figure 5.1.

Now the images are ready for motion tracking. The image sequence is imported into the software *Fiji*.<sup>[118]</sup> Thereafter, the motion tracking plug-in *TrackMate* is executed.<sup>a</sup> The output is a list of tracks with positions for every frame. The difference in position of two consecutive frames yields a motion vector. In theory, this data could already be used directly for plotting. However, the transformation at the beginning selecting three characteristic points is not precise enough. Error sources include the manual selection of points which strongly depends on the contrast of the image, since selecting the centre of a spot can be tricky. Additionally, it is difficult to identify characteristic points and some may diffuse or change their shape during scanning. There is also some translation error when cropping the images if they are not exactly on top of each other. Hence, a method with subpixel resolution using several data points is required.

### 5.1.2 Processing with *TrackRead*

Fortunately, an easy solution exists. By plotting the  $x$  or  $y$  component of each motion vector  $\vec{v}$  for a pair of consecutive images versus the  $x$  or  $y$  position in the first image of the pair, translation, stretching and shearing can be identified (Figure 5.2). By linear regression of each graph and adding the slope multiplied with  $x$  or  $y$  and

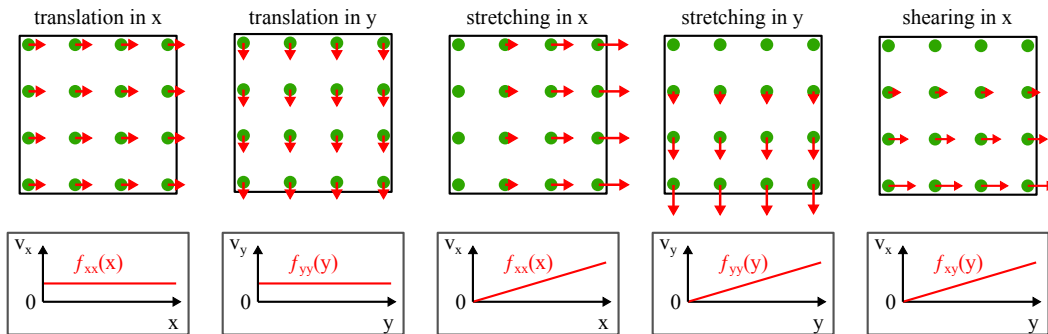


**Fig. 5.2:** Several examples for transformations of the images and how they can be detected. If the transformation is perfect, slope and  $y$ -axis intercept are zero for each plot.

adding the  $y$ -axis intercept from the corresponding points to the coordinates of the first image, the data are transformed according to:

$$x_{\text{new}} = x + \frac{df_{xx}(x)}{dx} \cdot x + f_{xx}(0), \quad (5.1)$$

$$x_{\text{new}} = x + \frac{df_{xy}(y)}{dy} \cdot y + f_{xy}(0), \quad (5.2)$$

<sup>a</sup>The images need to be converted to 8 bit greyscale before. The tracking parameters depend on image quality and contrast, typically a spot diameter of 5 pixels and a threshold of 1 are fine. For tracking, the *LAP tracker* with a maximum distance of 15-30 pixel and no gap closing is being used.

$$y_{\text{new}} = y + \frac{df_{yy}(y)}{dy} \cdot y + f_{yy}(0). \quad (5.3)$$

These equations are applied subsequently and the process is repeated several times.<sup>b</sup> This works best if using the motion vectors of little or non-moving molecules (otherwise outlier influence the result negatively, even if the vectors scatter around a line). Therefore, motion vectors with a length  $> 3$  pixels are ignored. Shearing is only performed along one direction ( $v_x$  vs.  $y$ , as caused by thermal drift.<sup>c</sup>). This method works best if the number of short motion vectors, that is little moving molecules, per frame is large ( $> 100$ ). Otherwise statistical scattering may influence transformation values noticeably. If molecules would not perform a random walk and the expectation for the average motion vector is not zero, the method should still work, because only non-moving molecules are taken into account.

Thereafter, the motion vectors are transformed to another coordinate system using the unit cell vectors  $\vec{a} = \begin{pmatrix} a_x \\ a_y \end{pmatrix}$  and  $\vec{b} = \begin{pmatrix} b_x \\ b_y \end{pmatrix}$  from the calcite unit cell. They are determined from a drift corrected image of calcite(104).<sup>d</sup> The new vector  $\begin{pmatrix} a_i \\ b_i \end{pmatrix}$  for each vector  $\vec{v}_i = \begin{pmatrix} x_i \\ y_i \end{pmatrix}$  is calculated via:

$$b_i = \frac{x_i \cdot a_y - y_i \cdot a_x}{b_x \cdot a_y - b_y \cdot a_x}, \quad (5.4)$$

$$a_i = \frac{y_i - b_i \cdot b_y}{a_y}. \quad (5.5)$$

In a final step, the resulting vectors are transformed again by subtracting the average motion vector<sup>e</sup> from the vectors for each image with  $n$  vectors:

$$\vec{v}'_i = \vec{v}_i - \sum_{k=0}^n \frac{\vec{v}_k}{n}. \quad (5.6)$$

If the result after applying Equations 5.1, 5.2 and 5.3 is already good, this last step (Equation 5.6) does not change the result much. However, especially with a

<sup>b</sup>This is required, because the length of the vectors changes due to the transformation and motion vectors with a certain length are ignored (see following text).

<sup>c</sup>The shear is along the fast scanning direction.

<sup>d</sup>For 100 nm  $\times$  100 nm images acquired with the AFM used for this thesis, the vectors were determined to  $\vec{a} = \begin{pmatrix} 1.872 \\ 2.100 \end{pmatrix}$  and  $\vec{b} = \begin{pmatrix} 3.814 \\ -2.900 \end{pmatrix}$ .

<sup>e</sup>For ATPA only vectors with  $|a| < 1$  and  $|b| < 1$  are used to ignore outliers.

low number of molecules in the image, this last step helps to get better results, because more motion vectors are included. The resulting data are used for the

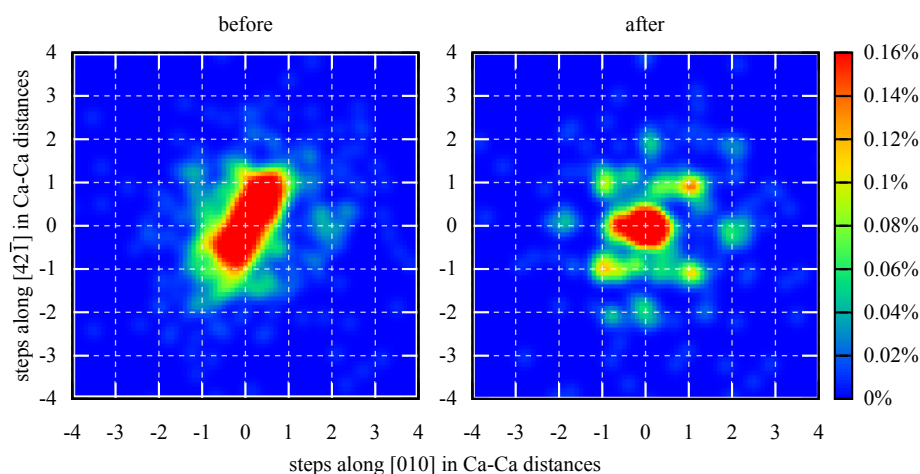


**Fig. 5.3:** Motion vector density map before and after transformation with *TrackRead*. After transforming images manually with *I12c*, the misalignment and distortion of the images is usually such that no pattern is evident before processing with *TrackRead*. The density maps in this figure show the diffusion pattern of 2,5-DHBA at 189.5 K (see Section 6.3).

output files. To generate motion vector density maps, the distance to each data point is calculated, weighted with a Gaussian ( $\sigma = 0.15$  in Ca-Ca distances) and summed up. In Figure 5.3, plots of such a density map before and after transformation with *TrackRead* are shown. This example underlines the importance of the post-processing presented in this section.

## 5.2 I12c

*I12c* ("I want to see") is a program that started as a simple tool for instrument calibration, but developed into a tool for drift correction using 2D-FFTs. This drift correction method requires images displaying periodicities. The program is able to process images that cannot be corrected with the method described in [119] and is very fast (creating drift corrected image files takes less than a minute). *I12c* is one of the programs utilised for the drift correction during the measurements in Sections 6.3 and 7.2.2.

In the first part of this section, the calibration is being explained. The second part describes the drift correction.

### 5.2.1 Calibration mode

It was found that images acquired with the *Omicron VT AFM* are slightly distorted and lengths measured in the images are too large. Therefore, a calibration of the instrument was needed. A first approach was to measure the distances of the unit cell in the images of a known substrate and to compare these with literature. With this method, a simple scaling factor was determined and applied to every image after scanning. However, the angles of the measured unit cells on a drift corrected image were still off by about 6%. Hence, a new way to calibrate images needed to be found.

Because the distances and the angle of a unit cell on calcite(104) are known, the

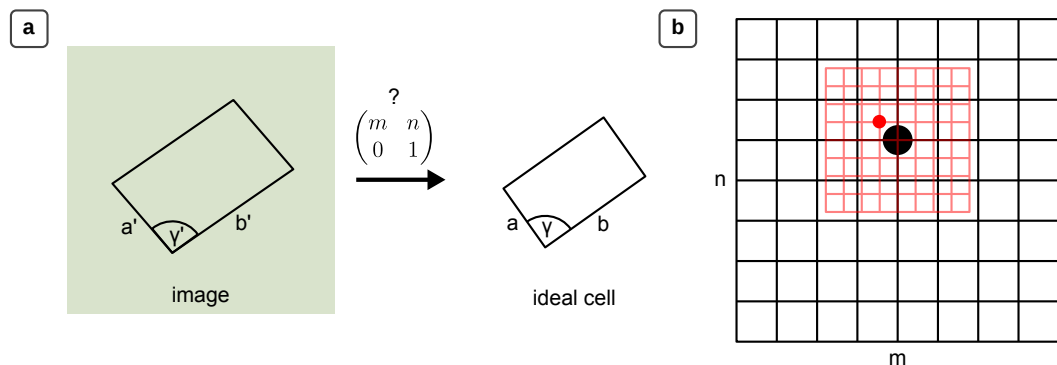


**Fig. 5.4:** Schematic drawings of the calibration problem **a** and its solution in the program **b**. Angle and dimensions of the ideal cell are known, but the transformation parameters  $m$  and  $n$  are unknown. To solve the problem, a set of values is tested (illustrated by the grid in **b**) and the best value (symbolised by the black dot) stored. The next iteration uses a smaller range for the parameters and, therefore, a finer grid (displayed in red). Because the evaluation of a pair of parameters is very fast, this simple algorithm proved to be best.

idea came up to apply shearing and stretching transformations to a drift corrected image measured with the instrument until the unit cell dimensions fit to the desired values (Figure 5.4a). To simplify the task, only the ratio of the two sides of the unit

cell is optimised and the scaling factor calculated afterwards. The transformation matrix<sup>f</sup> applied to the unit cell is then  $\begin{pmatrix} m & n \\ 0 & 1 \end{pmatrix}$  with the scaling factor  $m$  and the shearing factor  $n$  (both in  $x^g$ ). In order to find the proper parameters, a simple algorithm is used which is depicted in Figure 5.4b. To evaluate a set of parameters, the difference to the desired values for angle and ratio of the side length is summed up:

$$eval = |\gamma' - \gamma| + \left| \frac{a'}{b'} - \frac{a}{b} \right| \quad (5.7)$$

with the values  $\gamma'$ ,  $a'$  and  $b'$  of the transformed cell and the reference values  $\gamma$ ,  $a$  and  $b$ . After finding a good set of parameters for  $m$  and  $n$  (when the algorithm converged), the scaling parameter  $s$  is calculated to  $s = \frac{a}{a'}$ . The final transformation matrix is then  $\begin{pmatrix} m \cdot s & n \\ 0 & s \end{pmatrix} = \begin{pmatrix} s_x & n \\ 0 & s_y \end{pmatrix}$  with the scaling factors  $s_x$  in  $x$  and  $s_y$  in  $y$ . Using this method, a set of several drift corrected images was evaluated and the average transformation parameters determined for both AFMs used by our group each. It turned out that no significant shearing is required, but that the scaling factors in  $x$  and  $y$  are different (Table 5.1).

**Tab. 5.1:** Calibration parameters for both *Omicron VT* AFMs determined with *I12c*.

instrument	scaling in $x$	scaling in $y$
UHV I	0.83±0.02	0.91±0.02
UHV II	0.82±0.04	0.89±0.04

The errors of these calibration values reflect the extent of parameters found for different images.<sup>h</sup>

If a scan angle  $\alpha$  in  $^\circ$  is set in the measurement software<sup>i</sup>, the values of the transformation matrix for calibration change and need to be recalculated:

$$s'_x = \sqrt{(s_x \cdot \cos(\alpha \cdot \pi/180))^2 + (s_y \cdot \sin(\alpha \cdot \pi/180))^2}, \quad (5.8)$$

$$s'_y = \sqrt{(s_y \cdot \cos(\alpha \cdot \pi/180))^2 + (s_x \cdot \sin(\alpha \cdot \pi/180))^2}, \quad (5.9)$$

<sup>f</sup>A  $2 \times 2$  transformation matrix can be read as  $\begin{pmatrix} \text{scaling in } x & \text{shear in } x \\ \text{shear in } y & \text{scaling in } y \end{pmatrix}$  in this section.

<sup>g</sup>Note that shear in  $x$  is the same as shear in  $y$  followed by a rotation.

<sup>h</sup>The extent is rather large, since the parameters for each image depend strongly on the quality of the drift correction.

<sup>i</sup>The scan angle option does not rotate the sample, but changes the piezo movement to rotate the raster.



and if  $\alpha \neq 0 \pmod{90}$ )

$$n' = \cot \left( \arctan \left( \frac{s_x}{s_y} \cdot \tan \left( \alpha \cdot \frac{\pi}{180} \right) \right) + \arctan \left( \frac{s_x}{s_y} \cdot \tan \left( \alpha \cdot \frac{\pi}{180} \right)^{-1} \right) \right) - \frac{\pi}{2} \quad (5.10)$$

(else  $n' = 0$ ).

Besides instrument calibration, the software can also be used to perform a drift correction if the unit cell dimensions in an image are known. This was the reason to name the software *I12c* ("I want to see"), because it transforms any image to fit to the dimensions specified by the user. For instance, it is possible to distort a calcite(104) image to fit to the graphite(001) dimensions. Therefore, this drift correction method should be used with care. For the evaluation of diffusion measurements (Section 6.3), *I12c* was used to transform the images so that three characteristic points in each

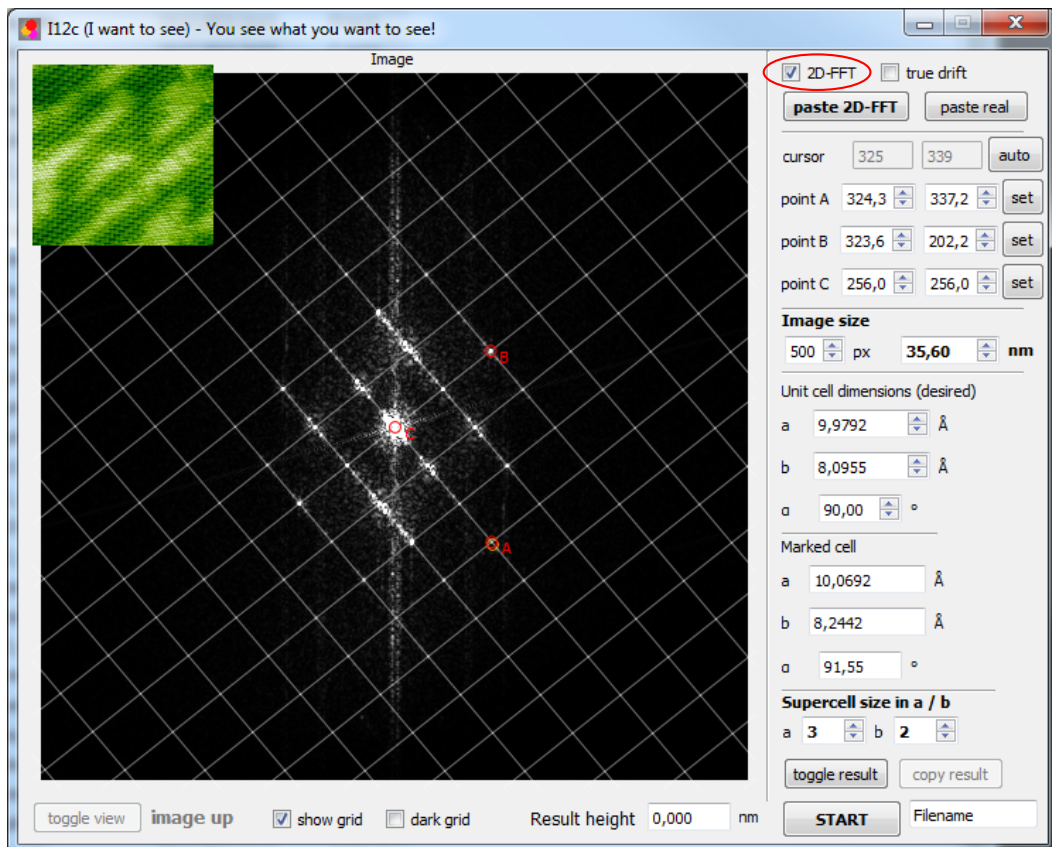


**Fig. 5.5:** Screenshot of the graphical user interface. The program is set to 2D-FFT mode on the top right (marked with a red oval). Besides the 2D-FFT, the corresponding real space image is shown on the top left. The unit cell dimensions calculated from the 2D-FFT are shown under "marked cell". After pressing start, the program uses the unit cell in real space calculated from the 2D-FFT to transform the image until it fits to the desired unit cell dimensions.

image were congruent to these points in the last image of an image series.

A graphical user interface (GUI) for *I12c* was programmed using *Qt* (Figure 5.5). In the GUI, it is possible to paste images from *Gwyddion* into the program without conversion. This allows marking the unit cell directly in the GUI. The resulting transformed images are stored as *.svg* and *.png* files after determination of the transformation matrix.

Since it is difficult to mark a unit cell in real space, an option to import 2D-FFTs from *Gwyddion* is implemented in the software. The user can mark the spots of the 2D-FFT and press *auto* in the GUI, which uses a simple algorithm to reposition the markers to the brightness maxima (or minima, if the colours of the 2D-FFT are inverted). The markers can be placed with subpixel resolution, which makes it very precise. For convenience, a grid can be displayed optionally to aid the user with the

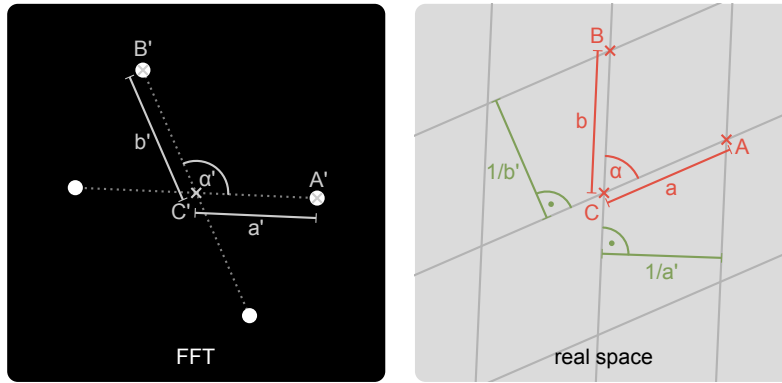


**Fig. 5.6:** Schematic drawing of the relation between 2D-FFT and real space image. The spots in the 2D-FFT mark periodicities in real space.

selection. From the marked points in the 2D-FFT, the dimensions of the unit cell in real space can be calculated (Figure 5.6) via:

$$\alpha = 180^\circ - \alpha', \quad (5.11)$$

$$a = (\sin(\alpha') \cdot a')^{-1}, \quad (5.12)$$

$$b = (\sin(\alpha') \cdot b')^{-1}. \quad (5.13)$$

Since the line segment  $\overline{CB}$  is orthogonal to  $\overline{C'A'}$  (and  $\overline{CA}$  is orthogonal to  $\overline{C'B'}$ ), the exact orientation of the real space unit cell is known as well. From then on the procedure is the same as before. It is possible to copy the real space image into the program which is then transformed.

The program can also be used just for the evaluation of 2D-FFTs, because it displays the unit cell dimensions in real space after placing the markers.

In the author's experience, most people find it difficult to evaluate 2D-FFTs and often make mistakes when doing a manual evaluation. The most common one is only looking for a unit cell in the 2D-FFT (instead of looking at the spots and drawing equidistant lines in real space accordingly) which fails for 2D-FFTs with a small amount of spots (like the one in Figure 5.6).

## 5.2.2 Drift correction with 2D-FFTs

*I12c* can also be used to perform a drift correction without any assumptions besides linear drift. For this correction, the two-dimensional fast Fourier transform (2D-FFT) of one *up*- and one *down*-image is used. Drift correction using the 2D-FFTs is surprisingly simple: the 2D-FFT of the drift corrected image is obtained by calculating the average spot positions after marking the spots in the 2D-FFTs.<sup>[120]</sup> However, especially for images acquired with a huge drift, it can be difficult to identify identical spots in two consecutive images. Therefore, a new method for drift correction was developed combining known techniques. The first step is to mark three spots in the 2D-FFTs of the *up*- and *down*-image respectively. This allows for the calculation of the points A, B and C of a unit cell in real space for each image, as described before. Let us assume now that the point C of the calculated unit cells for *up*- and *down*-image is at the very top of the image and that the *up*-image would be first in

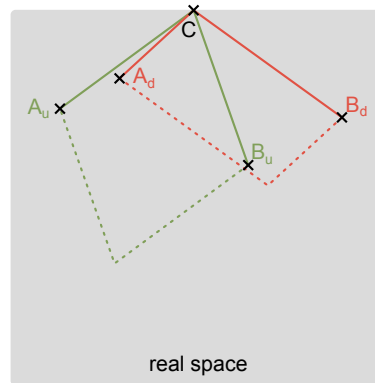


**Fig. 5.7:** Schematic drawing of the drift correction principle. The real space unit cells determined from the 2D-FFTs could be at the top of the image, where the point C is identical for both cells. A drift correction using the points A and B can be performed then.

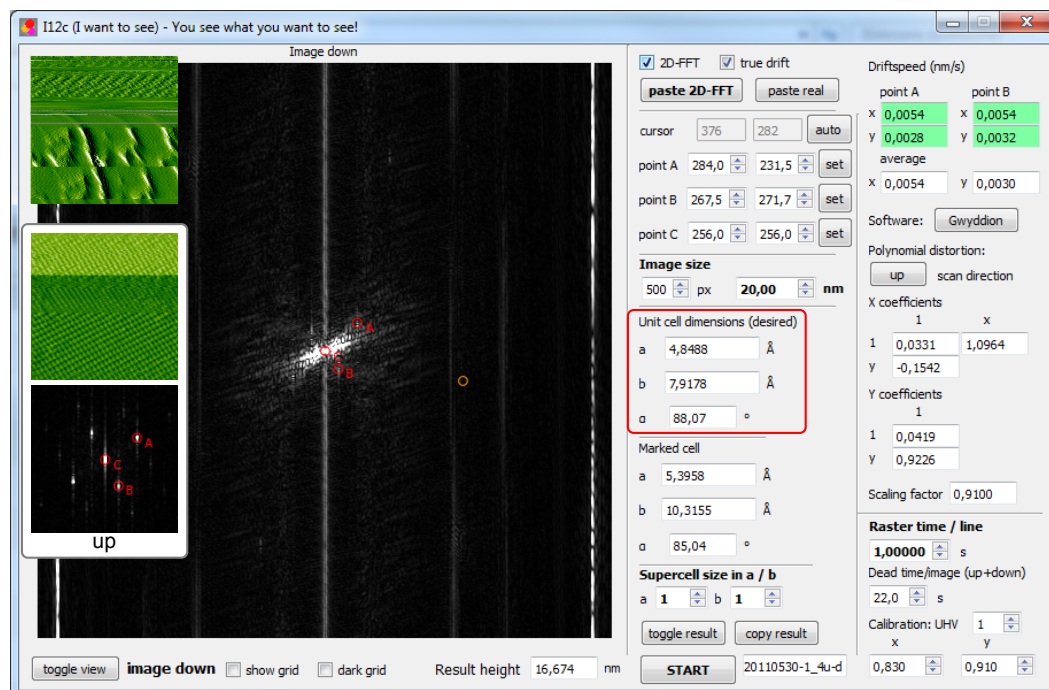


**Fig. 5.8:** Example of the drift correction of one image with good resolution (*up*, shown in the box on the left) and a consecutive *down*-image with bad resolution (top left). Even though the number of lines displaying a periodicity is small, a drift correction can be performed and the parameters of the drift corrected unit cell can be calculated (red box).

the series. Point C is then at the identical position for both images (see Figure 5.8). Using the points A and B for both scan directions, it is now possible to perform the usual drift correction described by [119]. This way, two drift velocities are obtained (one for the point A, one for B). If both velocities are similar, the spots in the 2D-FFT are selected properly. An example of the application of this drift correction is shown in Figure 5.8. An advantage of this method compared to other methods is that only a few good lines are required and it is no problem if bad scan lines, tip changes or even a displacement of the tip occur during scanning. The only requirement is a visible periodicity, the order of the images (if the *down*-image is first) does not matter.

At this point, it should be noted that the author of this thesis also wrote a program called *AlphaDrift*, which allows the user to set a certain drift speed and transforms two inserted consecutive images from a series accordingly.<sup>[119]</sup> These images are placed on top of each other by the program, so that the drift corrected images are identical at their intersection if setting the proper drift speeds. By changing the transparency of the top image, it is possible to align images very precisely (Figure 5.9), even if no periodicity can be seen. With both programs *I12c* and *AlphaDrift* drift corrected images are obtained within a minute. Furthermore, they usually produce better results, that is the corrected images are more similar at their intersection, than the correction performed before using the method described in [119]. The reason is that *I12c* takes into account the whole image and the selection of spots in a 2D-FFT is easier and, therefore, more precise than selecting the same feature in real space and with *AlphaDrift* the similarity at the intersection is optimised directly.

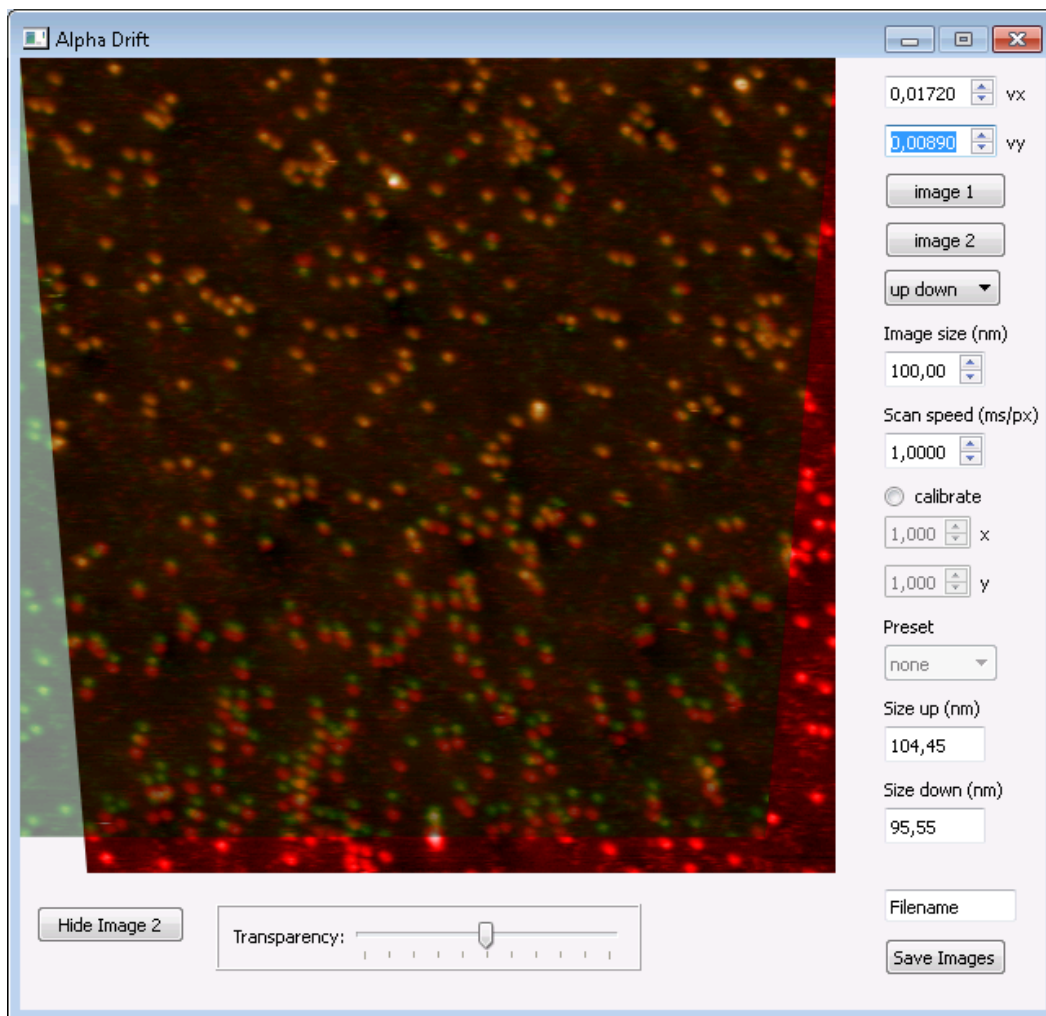


**Fig. 5.9:** Snapshot of the Software *AlphaDrift*. The user can specify a drift speed and the program applies the resulting transformation for the *up*-(red) and *down*-image (green). By making the top image (in this example the green *down*-image) semi-transparent, it is possible to determine the transformation parameters very precisely by checking if the images are identical at their intersection. You may notice that the images in this example do not fit perfectly at the bottom due to non-linear drift, which prevents a better correction.

### 5.2.3 Choosing the proper drift correction method

In general, drift correction using *AlphaDrift* is the method of choice. It is very precise and works for most examples. However, if characteristic features are not easy to identify on the images, using *AlphaDrift* can be tedious. This is usually the case for periodic structures, where the drift correction with *I12c* using 2D-FFTs can be performed. This works even in extreme cases with tip changes and few good lines (see Figure 5.8).

Only if there is just one image of a structure with known dimensions, the calibration mode may be used to transform the image. However, images generated with this method should never be used to determine a structure.

## 5.3 Justin

*Justin* is a software for the fully automated acquisition of sublimation curves with evaluation during measurement.

For sublimation experiments, a molecule evaporator equipped with a Knudsen cell and attached to an ultra-high vacuum (UHV) chamber is used for sublimation of molecules. The Knudsen cell is heated with a tantalum wire coil connected to a power supply. A quartz crystal microbalance (QCM) inside the chamber detects the mass of the deposited layer. This mass is converted by the controller to a thickness using the area of the quartz and the density of the molecules.

Upon starting measurement, *Justin* increases the temperature of the sublimation cell with coarse steps until the mass at the QCM is increasing. The increase of the thickness is monitored for some time until enough measurement points exist to perform an acceptable linear regression. By changing the temperature by small steps and monitoring the thickness, the sublimation rate for different temperatures is recorded. With these data, an Arrhenius plot and additional evaluation plots (Figure 5.13 and Figure 5.11) are created during measurement.

In the following section, the measurement and evaluation procedures are explained in detail.

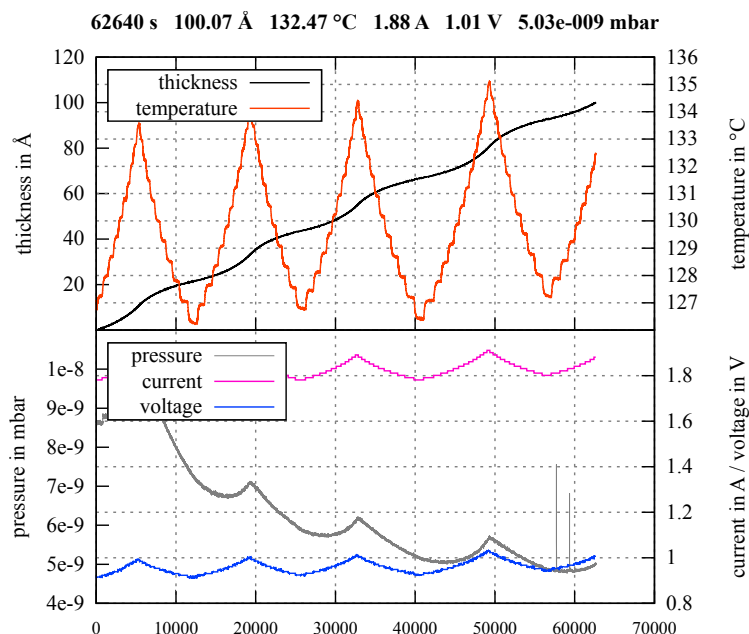


**Fig. 5.10:** Main window displayed during the measurements with *Justin*. In addition, the evaluation windows (Figures 5.11, 5.12 and 5.13) start to appear if two reasonable rates are measured.

### 5.3.1 Procedure

The program *Justin* consists of two parts: measurement and data evaluation. These parts are inside a loop and executed one after another.

The measurement part is rather simple and basically acquires sixty data points. For each point the time since start, the temperature at the sublimation cell, the thickness of the layer reported by the QCM, the pressure inside the chamber and the current and the voltage of the power supply are stored.

Besides, the measurement part controls the power supply to change the temperature

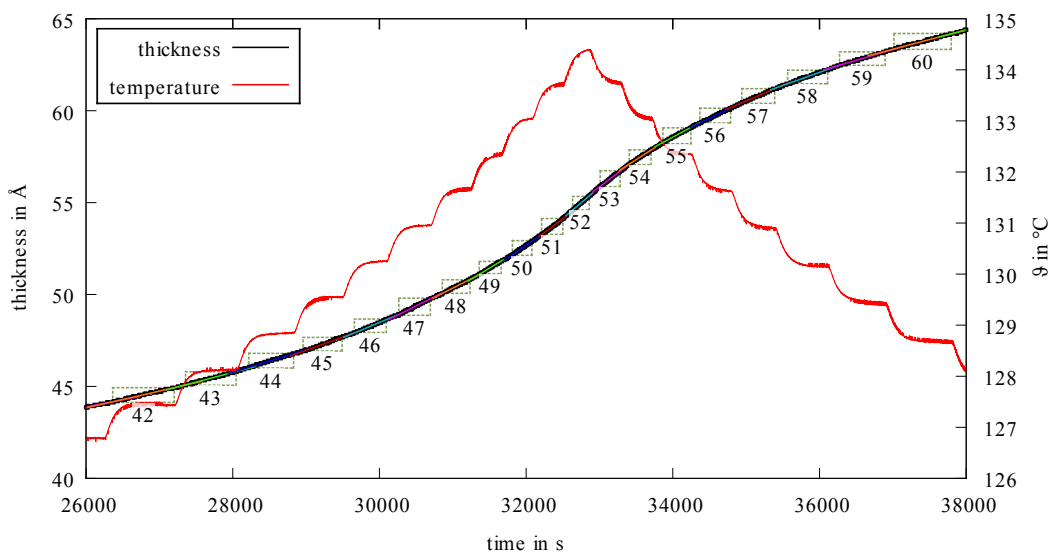


**Fig. 5.11:** Section of a sublimation curve acquired with *Justin*. The dashed boxes represent the segments of constant temperature where the slope is determined. Coloured lines represent the fits. The software automatically measures longer for low sublimation rates.

of the sublimation cell. There are two modes for changing the current at the power supply: *coarse step* and *measurement* mode.

The *coarse step* mode is set at the beginning and just collects data for a certain time before increasing the temperature with a coarse step. This is repeated until the evaluation part reports that a significant increase in thickness is measured and *Justin* switches to *measurement* mode.

*Measurement* mode means that the temperature is changed in small steps and the data acquisition time is longer. Furthermore, the temperature is not only changed after reaching a maximum acquisition time for a temperature, but also if parameters from the evaluation are above a user defined threshold. These are the coefficient of determination  $R^2$  and the thickness change.  $R^2$  proved to be quite a good indicator for the quality of a set of values, because it is a measure for linearity.

Measuring very small rates is limited by the precision of the QCM and too high rates increase the pressure and can even lead to macroscopic deposition of molecules



at the walls of the chamber. Therefore, a minimum and a maximum rate are set for measurement. Upon reaching the maximum rate, the temperature is decreased for the next steps and vice versa. This way the program performs cycles ramping up and down (Figure 5.11) until the user stops the program or a maximum layer thickness on the QCM is reached.

For molecules that do not stick well to the QCM or do not sublime prior to decomposition temperature, pressure and temperature limits are set by the user. After being above these thresholds for 30 s, the measurement is either stopped (in *coarse step* mode) or the program sets a lower temperature and is decreasing the temperature for the next steps. If no significant rate is measured and the program is in *measurement* mode, it switches to *coarse step* mode again. This is important if some impurity is measured first and the expected molecules sublime at higher temperatures.

Evaluation is not too complicated as well. The program reads in the temperature and checks whether it is constant (usually a change of less than 0.1 K within 60 s). The slope of the thickness reported by the QCM is then determined from this moment on until the current at the power supply changes. Measurement time, thickness change and  $R^2$  need to be good enough (depending on parameters set by the user) to be used for the further evaluation. Otherwise the values are being ignored. Using the slope and the average temperature of a value, an Arrhenius plot (Figure 5.12) is created and the sublimation enthalpy is determined.

For taking temperature and rate<sup>j</sup> errors into account, a linear fit considering both

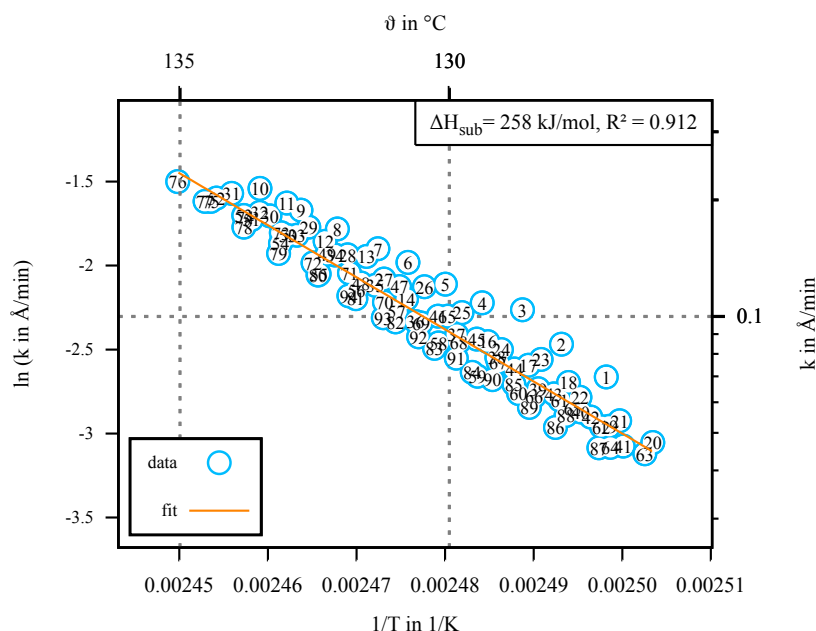


**Fig. 5.12:** Automatically created Arrhenius plot of the rates created during measurement. The values are numbered and show that at the beginning of the measurement the rates are slightly higher and stabilise after some time.

errors is performed optionally. This is done by adding random fractions of the x- and y-errors to each value and performing the Arrhenius fit. After repeating the procedure described in the last sentence several times and storing the results, the average slope is determined and the error of the slope calculated to three times the standard deviation<sup>k</sup> of the stored slopes.

Apart from the Arrhenius plot, a simple plot of the sublimation rate and current versus temperature allows for finding the right combination of current and temperature for a certain desired rate (Figure 5.13).

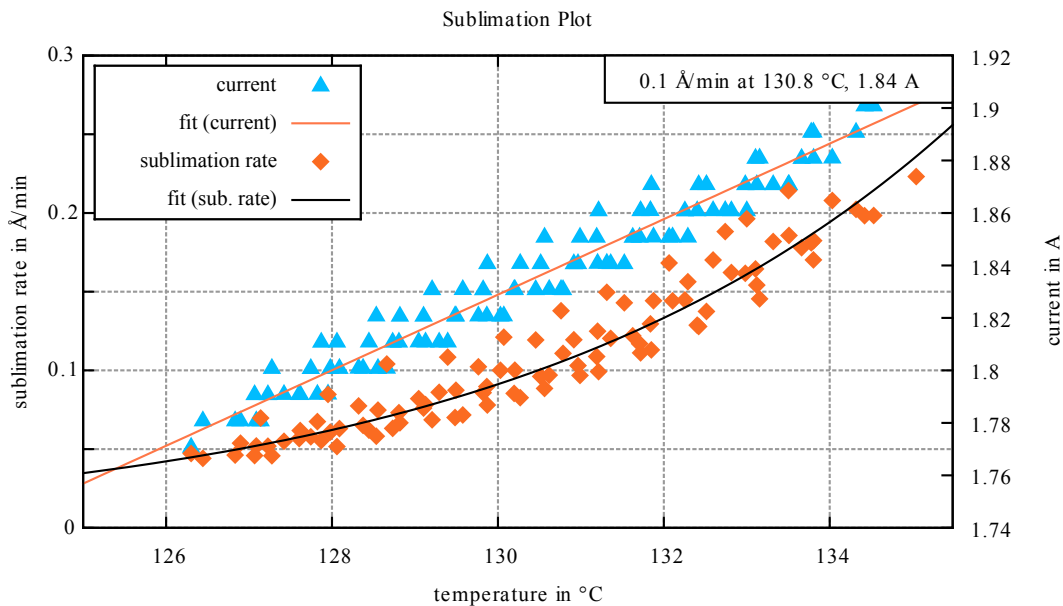


**Fig. 5.13:** Plots of the sublimation rates and corresponding currents at the power supply for different temperatures. This allows for an easy selection of the proper current and temperature for a desired sublimation rate.

To configure the program, a set-up program with graphical user interface was created with tool tips for the different options. Afterwards, the main program can be started and the measurement begins.

### 5.3.2 Comparison with manual measurement and evaluation

Obviously, the fully automated measurement saves a lot of time, because it is not necessary to monitor the measurement and it can be performed over night. Additionally, the algorithm is much better than an operator in identifying a good point to change the temperature. For high sublimation rates the measurement time

<sup>j</sup>The relative error of the rate is difficult to estimate, because the usual error calculated from the linear regression is way too small. It is, therefore, calculated using the empirical formula  $\delta r = 1 - \exp(-a \cdot (1 - R^2))$  with the parameter  $a = 30$  per default. This yields reasonable results, that is where the Arrhenius fit is usually within the error of all values.

<sup>k</sup>This assumes that the result is similar to a Gaussian distribution.

is shorter than for low rates. It was found that a few minutes are usually good enough to determine a reasonable rate. Therefore, the program is able to record more than hundred data points for the Arrhenius plot within a day. If impurities sublime at the beginning of a measurement, they can be easily identified due to the better time resolution. Furthermore, the pressure is being recorded during measurement and even if the molecules do not stick to the QCM, a good temperature for sublimation can be estimated by looking for a significant pressure increase. Due to the evaluation during measurement, the user can easily decide when to stop the measurement, rather than measuring first, stopping the experiment and discovering later on that the values are not linear and more values are required. The evaluation is easier and reproducible, in contrast to a manual evaluation where the selection of values for one temperature range is somewhat arbitrary. For the manual exclusion of data points, a separate, self-written program for data evaluation exists (*Chantal*) that basically consists of the evaluation part of *Justin* only.



## 2,5-DHBA

2,5-DHBA on calcite is an extraordinary system, because a slow phase transition from a striped phase to a dense phase is observable at room temperature. This has been attributed to a deprotonation. The deprotonation conjecture has been supported by KPFM images indicating a negative charge for the dense phase.<sup>[23]</sup> In this chapter, this system is characterised in more detail with high-resolution measurements at low temperatures. The highlight is the characterisation of the diffusion for single molecules (Section 6.3). But first, the system is introduced and the coverage dependence investigated.

### 6.1 The system

In previous measurements the focus has been on the phase transition from a striped to a dense phase (Figure 6.1). The structure of the striped phase has been identified as a  $(6 \times 1)$  superstructure. However, the dense phase is simply a  $(1 \times 1)$  superstructure (Figure 6.1c), on the contrary to what has been stated before.<sup>[23]</sup> It has been shown that the two different island types of the dense phase (Figure 6.1b) are shifted by half a unit cell along  $[42\bar{1}]$ , as expected due to the glide mirror axis of calcite(104)

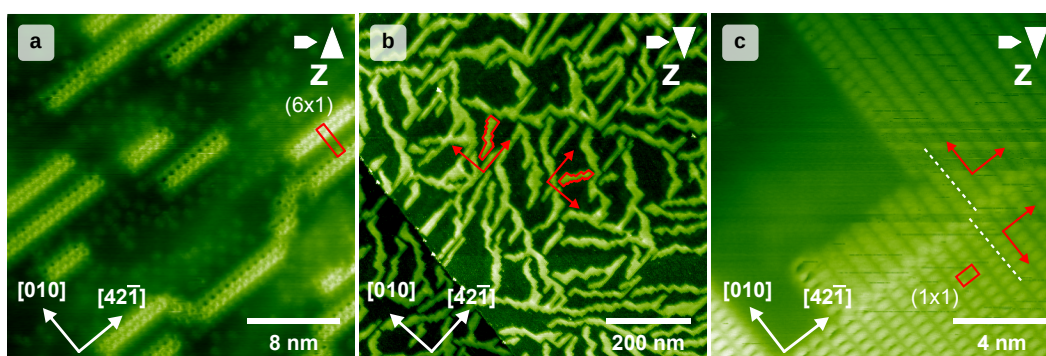


**Fig. 6.1:** Images of 2,5-DHBA on calcite(104) acquired at 185 K. For **a** the sample was prepared at low temperatures and heated to 245 K for a short time. Images **b** and **c** are from the same sample after keeping the sample at room temperature for several hours. Between **a** and **b** the phase transition between striped and dense phase occurred. The dense phase consists of two mirrored structures that grow in different directions (marked with red arrows in **b**). In **c** a high-resolution image of the border between two different islands (growth directions marked with red arrows) growing next to each other is shown. Due to the mirrored structure the islands are shifted by half a unit cell (dashed lines). This reflects the glide mirror axis of calcite(104). Stripes close to each other form a  $(6 \times 1)$  superstructure, the dense phase a  $(1 \times 1)$ . All images are calibrated, **a** and **c** drift corrected.

(Figure 6.1c). While most about the striped and dense phase has already been known, the diffusing species has been completely unknown. The reason has been that at room temperature the diffusion is so fast that diffusing molecules were not imaged and manifested in stripes along the fast scanning direction only. When imaging a sample at 185 K that has been at room temperature before, the number of diffusing molecules was rather high (Figure 6.2). It was also discovered that close to the dense phase a  $c(4\times 2)$  phase was forming. Interestingly, this was only found at the direction of growth of the islands along  $[010]$  or  $[0\bar{1}0]$  (depending on the island, for details see appendix, Section 10.3.1). Additionally, it appears that there are sometimes little stripes with two or more molecules (marked with circles in Figure 6.2) formed by the diffusing species. However, it was observed that they form and dissociate even at 185 K.

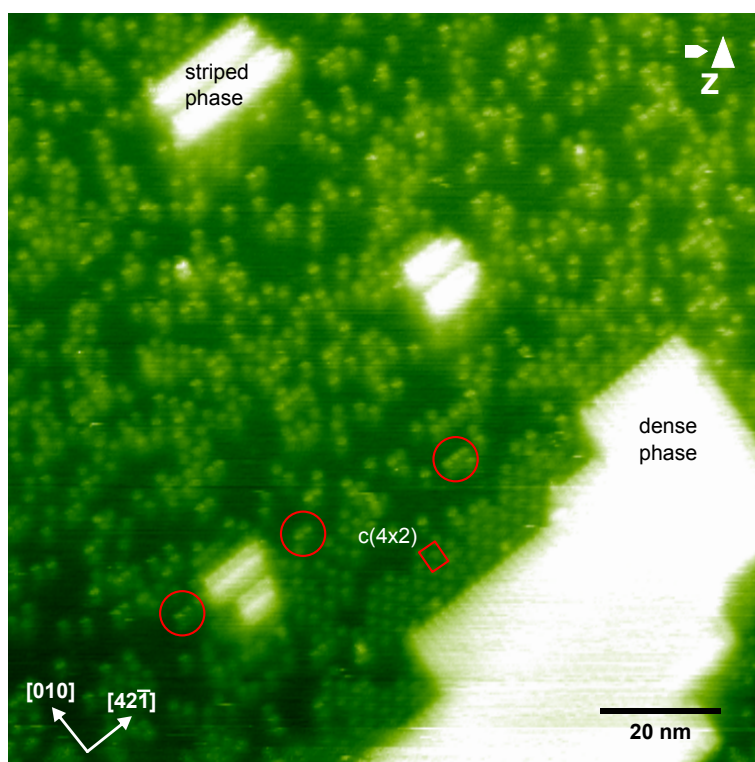


**Fig. 6.2:** Image of a sample prepared at room temperature and cooled down to 185 K. Most molecules are in the dense phase already, but some stripes still exist. Close to the dense phase a  $c(4\times 2)$  superstructure is observed (unit cell marked red in the image). Apparently, it only forms at the direction of growth along  $[010]$  or  $[0\bar{1}0]$ . Within the mobile phase some loose little stripes are formed (three marked with red circles) which display a slightly different contrast than single molecules. This image is calibrated and corrected for drift.

## 6.2 Coverage dependence

As written in the previous section, the number of diffusing molecules next to the striped and the dense phase is rather high. Figure 6.2 shows an image taken while the transition between striped and dense phase was still in progress when cooling the sample down. With these measurements, it was investigated whether the number of diffusing molecules is reduced when the phase transition is completed.

In Figure 6.3, the sample is shown before and after completing the transition (the

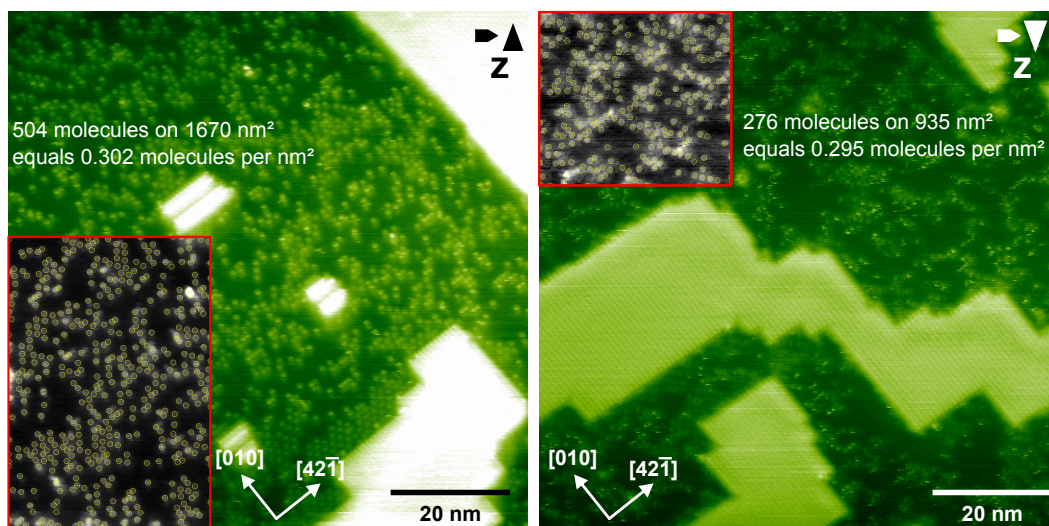


**Fig. 6.3:** Determination of the coverage between islands at 185 K. The first sample was kept at room temperature during 18 minutes of sublimation and then cooled down after a quick look at it. The second image was taken after letting the sample warm up again and stay at room temperature over night. Apparently the concentration of diffusing molecules did not change.

sample was kept at room temperature over night). Completion of transition means that there are no more stripes and the growth of islands stops. The number of diffusing molecules in the marked areas was determined using the *TrackMate* plug-in for *Fiji*.<sup>[118]</sup> Before completing the transition, the molecule density equals to 0.302 molecules per nm<sup>2</sup>. After completion of the transition, it is 0.295 molecules per nm<sup>2</sup>. Thus, there is no significant change in the concentration of diffusing molecules. This finding implies that the growth of the dense phase does not stop because there are no more diffusing molecules. The measurements in the next section (Figure 6.5) were performed after one minute of sublimation and the total number of molecules in one image with a known area can be counted. With these data, the sublimation rate was determined to 0.024 ML/min (one ML being one molecule per unit cell). It was calculated that the concentration of diffusing molecules in Figure 6.3 equals a sublimation time of about five minutes, since 0.3 molecules per nm<sup>2</sup> correspond to a coverage of about 0.12 ML.

Thereafter, a measurement series at room temperature with increasing coverage was performed (Figure 6.4). It can be seen that below the coverage determined in

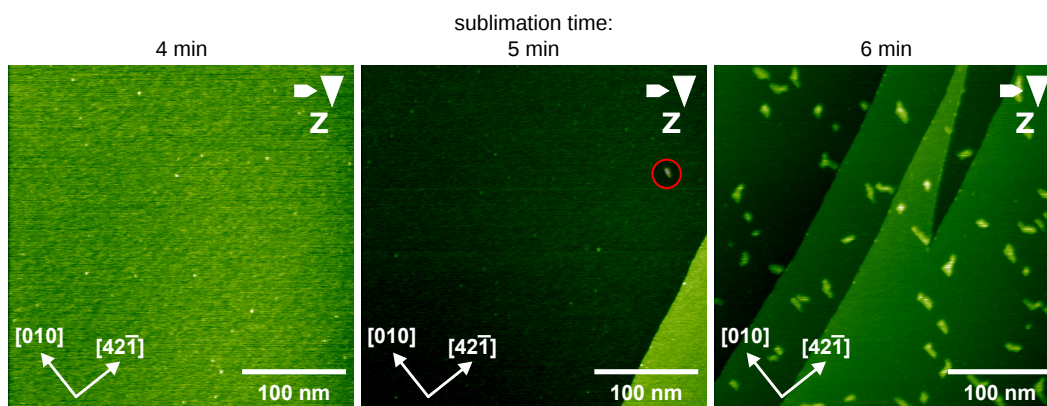


**Fig. 6.4:** Images of 2,5-DHBA at room temperature for different sublimation times. The coverage at five minutes of sublimation equals the concentration of molecules determined in Figure 6.3. Only one single small island (red circle) was observed after five minutes. At slightly higher coverages (six minutes of sublimation) suddenly islands start to grow.

Figure 6.3 no islands are visible (after four minutes of sublimation). At a coverage larger than the coverage in Figure 6.3 (after six minutes of sublimation), the first islands start to grow. This suggests that a critical coverage is needed to form island structures.

For the diffusion experiments in the next section, this information proved to be very helpful, because the diffusing species does not form self-assembled structures at low coverages and can diffuse freely. Otherwise the number of diffusing molecules would be reduced during measurement.



## 6.3 Diffusion

Besides coverage, the mobility of molecules is crucial for the formation of self-assembled structures. In this section, the diffusion process is investigated by direct imaging of moving molecules.

Observing single diffusing 2,5-DHBA molecules is only possible at a narrow temperature range around 190 K. Below, virtually no molecules are moving within the measurement time. Above, the diffusion is too fast to track single molecules or the molecules cannot be imaged at all.

### 6.3.1 Data acquisition

Measurements were performed with a low scanning speed of 1000 s between two *up*-images. Thus, the influence of thermal drift was quite serious. Therefore, drift compensation during measurement was done using the built-in drift compensation of the *Omicron Matrix* software determining the drift speed with the manual drift compensation tool and self-written programs (see Chapter 5.2).

Because of the long data acquisition time, non-linear thermal drift and tip changes during measurement, acquiring image sequences for different temperatures is challenging. Hence, series of only 5–10 consecutive usable *up*-images could be obtained. Two measurement series were performed acquiring image sequences at three temperatures each (185 K, 189.5 K and 194 K). The first measurement series started at 194 K, the second at 185 K.

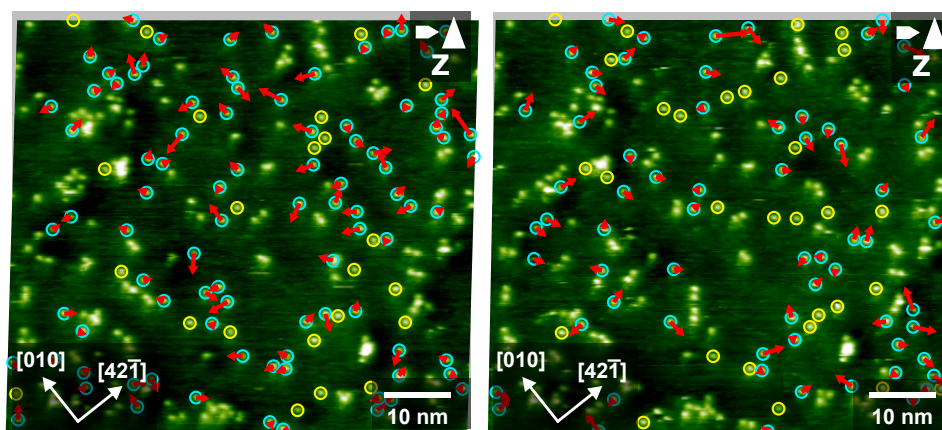


**Fig. 6.5:** Two evaluated consecutive images from a series at 194 K. Moving molecules are marked turquoise with an arrow indicating the position in the next image. Yellow marked molecules do not move now, but later within the series. Non-marked particles either never move or are ignored due to clustering or wrong track assignment. Both images are aligned to the last image (indicated by grey boxes in the background). The complete series can be found in the appendix (Section 10.3.5).

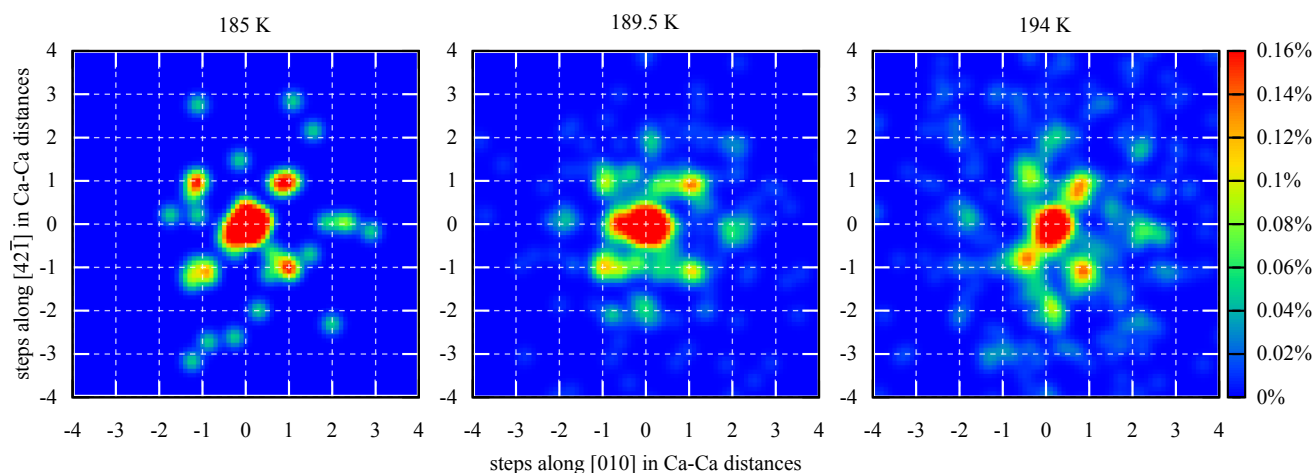


**Fig. 6.6:** Plots of the motion vector density mapped to the main symmetry directions of calcite(104)  $[010]$  and  $[42\bar{1}]$  for three different temperatures (first measurement series). The step length is one calcium-calcium distance along these directions. It is apparent that the molecules move diagonally to the main symmetry directions.

### 6.3.2 Data processing and results

To evaluate these data, the images of a series were transformed to compensate for drift and to align each image to the last image. This was done by selecting three characteristic points in each image and using a numerical algorithm to determine the transformation matrix. Then the images were put on top of each other and cropped to the area they had in common (see Section 5.1.1 for details).

In a next step, the *TrackMate* plug-in for *Fiji*<sup>[118]</sup> was used to perform motion tracking of the molecules. Wrong tracks were, if spotted, removed manually and areas with large molecule clusters masked. Afterwards, the data were aligned almost perfectly to the last image using the motion vectors to determine the transformation matrix (see Section 5.1.2). Clusters and never moving single molecules, possibly caused by surface defects, were ignored. The result can be seen in Figure 6.5. Thereafter, the motion vectors were mapped to the main symmetry directions  $[010]$  and  $[42\bar{1}]$  of calcite(104). A last alignment step was performed subtracting the average motion vector from the vectors for each image (see Section 5.1.2).

In Figure 6.6, the resulting distribution of motion vectors for three different temperatures is displayed. The distortion of the last map and density between the diagonal jumps is attributed to processing artefacts.

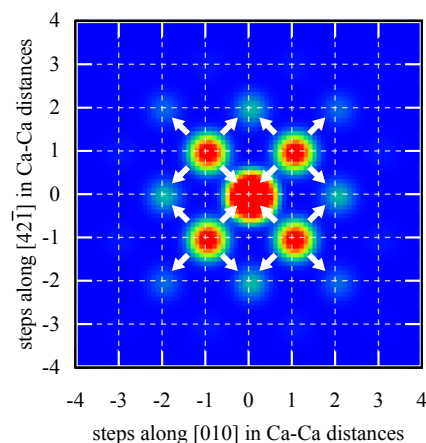


**Fig. 6.7:** Simulated (Eq. 6.1) map for the data at 189.5 K using the fit parameters from Figure 6.8. The arrows indicate the possibilities for a second jump and explain the pattern being observed.

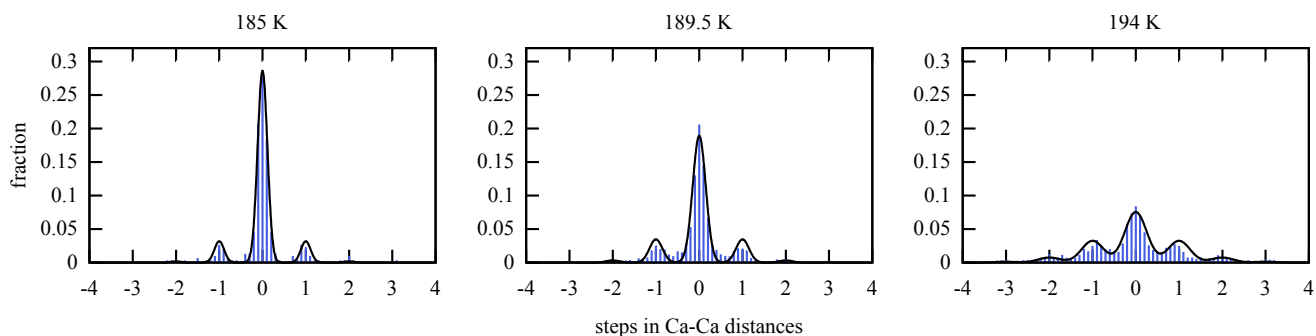


**Fig. 6.8:** Histograms of the one-dimensional jumps along the diagonal directions (Figure 6.6) for different temperatures. Because of the glide mirror axis of calcite, the two equivalent diagonal directions were combined for these diagrams. The average number of jumps for each temperature can be determined fitting the histograms via  $\mu$  and  $\sigma$  using Equation 6.2 (black line).

Note that one diagonal jump is less than four pixels in an AFM image and, therefore, these plots are quite sensitive, for example, to a slight misalignment.

The density map for 185 K (Figure 6.6) discloses a striking observation: the molecules appear to diffuse not along the main symmetry directions, but diagonally instead. This is noteworthy, because, for instance, theoretical calculations of the diffusion barrier often assume movement along the main symmetry directions. For higher temperatures, additional jump directions are observed, which are interpreted as combinations of two diagonal jumps (Figure 6.7). The jump length for each diagonal jump corresponds to the diagonal Ca-Ca distance of calcite (6.4 Å). One interesting consequence from the diagonal diffusion mechanism is that the molecules can only reach half of the surface positions (like black and white squared bishops in chess). So far, it is unclear how this specific diffusion influences self-assembly. Furthermore, a flat-lying 2,5-DHBA molecule cannot occupy an identical adsorption position if translated diagonally due to the symmetry of the calcite(104) surface (wallpaper group  $pg$ ). Reaching an identical position would require flipping the molecule. This implies that there are either two different adsorption positions for a diffusing molecule or the diffusion process involves rotations.

For a more detailed analysis, histograms of the jumps along the diagonal directions were made (Figure 6.8). In order to calculate the average number of steps  $\mu$  per image, the diagrams were fitted using the following assumptions: the chance to find a molecule at a point  $d \in \mathbb{Z}$  can be calculated if the number of steps between the images is Poisson-distributed and the molecules perform a random walk (binomial distribution):<sup>[121]</sup>

$$p(d, \mu) = e^{-\mu} \sum_{j=0}^{\infty} \left(\frac{\mu}{2}\right)^{2j+|d|} \cdot (j! \cdot (j + |d|)!)^{-1} = e^{-\mu} \cdot I_{|d|}(\mu) \quad (6.1)$$

with the modified Bessel function of the first kind and  $n$ th order  $I_n(x)$ . A derivation can be found in the appendix (Sections 10.3.2, 10.3.3 and 10.3.4). The measured

jump distances are now assumed to be normal-distributed around each step with the standard deviation  $\sigma$  and an amplitude calculated from Equation 6.1. Therefore, the distribution function for the jump distance  $x$  for a histogram with a bin width  $b$  becomes:

$$f(x) = \sum_{k=-\infty}^{\infty} p(k, \mu) \cdot \frac{b}{\sqrt{2\pi} \cdot \sigma} \cdot e^{-\frac{(x-k)^2}{2\sigma^2}}. \quad (6.2)$$

Knowing the average number of steps, the jump frequency  $\nu = \frac{\mu}{\tau}$  with  $\tau$  being the time between two images can be determined. An Arrhenius plot of the results for both measurement series is shown in Figure 6.9.

To validate this approach, the frequencies were also calculated from the fraction of non-moving molecules in each image (Figure 6.5). This fraction was used to calculate the number of steps by comparison with a plot of  $p(0, \mu)^2$  (Equation 6.1, it has to be squared because the data is two-dimensional) versus  $\mu$ . This takes into account that molecules returning to their origin after moving several steps also appear as if they were non-moving. Both methods yield very similar results and are robust to evaluation parameter changes.

The diffusion barrier  $\Delta E_{\text{diff}}$  was calculated to be 0.36 eV and the attempt frequency to be  $1 \times 10^6 \text{ s}^{-1}$ . The error of these values is hard to estimate, especially due to the

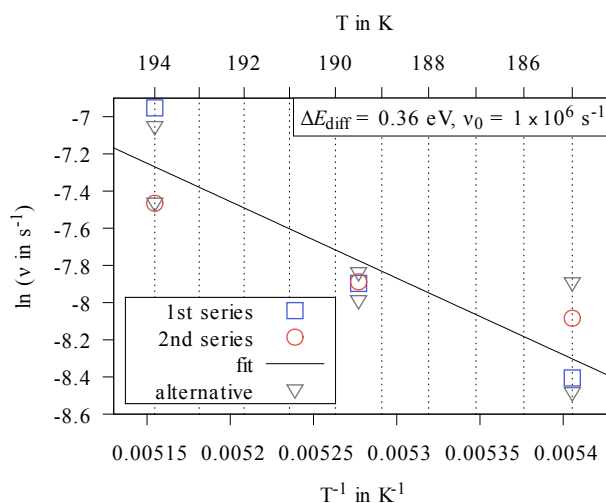


**Fig. 6.9:** Arrhenius plot of the frequencies calculated from the number of steps from the fit (Figure 6.8) and the fraction of non-moving molecules (alternative method, Figure 6.5).

complex data processing. Error sources include the temperature measurement (at the stage and not at the crystal surface), tracking errors, imperfect drift correction and irregular moving molecules (for instance, molecules "captured" by a defect for a short time or molecules manipulated by the tip). In addition, the linearity of the resulting data is rather poor and an Arrhenius plot is quite sensitive to small changes. More samples would be needed to draw a definite conclusion. Therefore, the quantitative evaluation should be taken with a grain of salt and rather seen as a

proof of concept. Still, the very small attempt frequency may indicate large entropic contributions<sup>[122]</sup> untypical<sup>[18,58,63]</sup> for diffusion.<sup>a</sup>

### 6.3.3 Conclusion

It is shown that it is possible to characterise diffusion of an organic molecule on an insulating surface with NC-AFM using motion tracking. The density map of motion vectors (Figure 6.6) is used to determine the diffusion directions and jump length. It is found that the diffusion direction for 2,5-DHBA is exclusively diagonal to the main symmetry directions of calcite(104) with interesting consequences. For instance, it contradicts the initial assumption of the molecules moving along the main symmetry directions. This information is essential for theoretical calculations of the diffusion barrier and underlines the importance of the analysis presented here for such calculations.

By fitting the histograms for jumps along the diagonal directions (Figure 6.8), it is possible to calculate the jump frequencies for each temperature and perform an Arrhenius plot (Figure 6.9).

In conclusion, a qualitative and quantitative analysis of the diffusion process is obtained from rather short series of images.

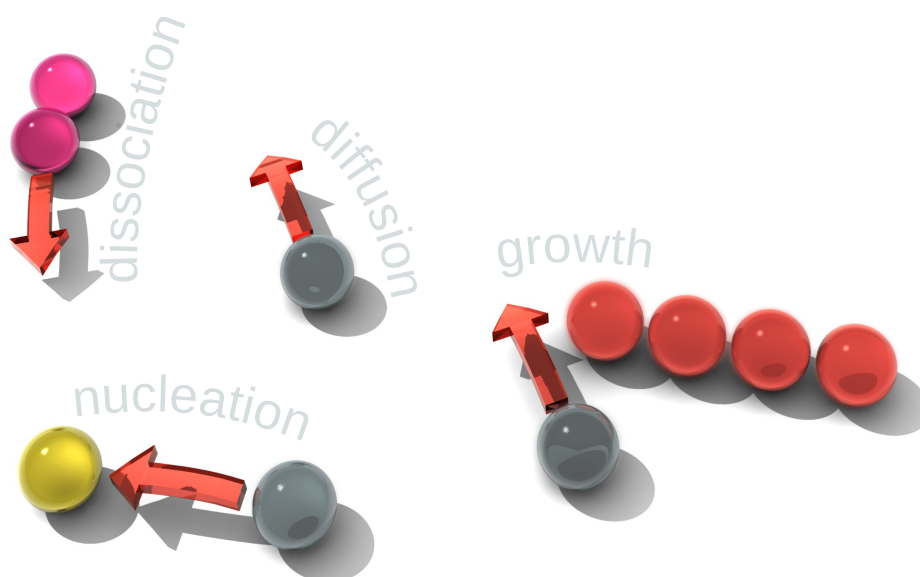
---

<sup>a</sup>A small attempt frequency implies that there are less degrees of freedom in the transition state.



## Terephthalic acid and its derivatives

In this chapter, the focus is on the influence of different functional groups, namely an amino group for 2-aminoterephthalic acid (ATPA) and a bromo group for 2-bromoterephthalic acid (BrTPA), on the diffusivity of terephthalic acid (TPA) and its derivatives at low temperatures. Notably, the diffusion and self-assembly process of ATPA is examined in detail. The diffusion is analysed using the motion tracking technique introduced in the previous chapter. But first, the self-assembly of TPA at elevated temperatures is investigated to introduce the system.



## 7.1 TPA at room temperature and elevated temperatures

TPA has been popular as a molecular linker due to its two carboxylic acid groups.<sup>[123]</sup> Therefore, several studies on different substrates exist in literature. STM and AFM studies on rutile(110) at room temperature have revealed that the molecules in a closed monolayer are upright standing<sup>[124]</sup>, whilst flat-lying molecules<sup>[125]</sup> have been observed at lower coverages. On calcite(104) a  $(2 \times 2)$  superstructure consisting of two mirrored domains ( $\alpha$  and  $\beta$ ) has been reported for low coverages at room temperature. At higher coverages, a second phase has been found, which has been assigned to either a second layer or upright standing molecules.<sup>[100]</sup>

To understand the structures in more detail, an image series with increasing coverage was recorded starting with a sublimation time of 15 min at 106 °C and gradually increasing the coverage to 45 minutes total sublimation time (Figure 7.1). Previously,

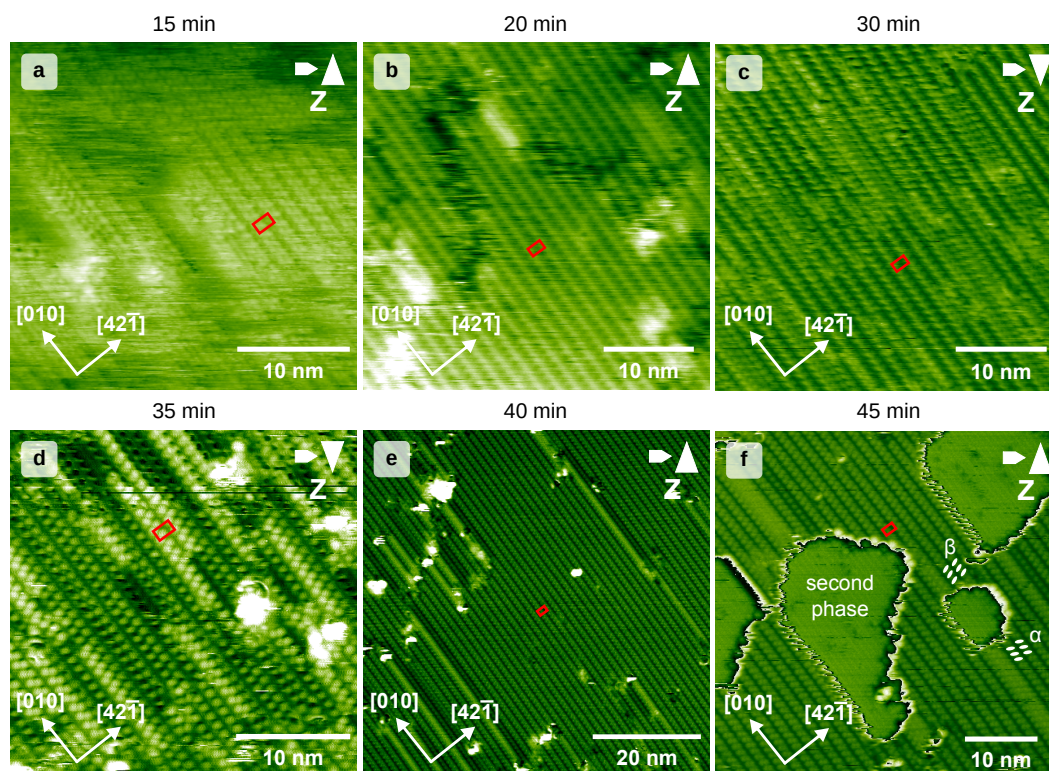


**Fig. 7.1:** TPA measurements at room temperature for different coverages. In every image the  $(2 \times 2)$  superstructure is indicated with a red rectangle. The sublimation temperature was 106 °C, the sublimation time is stated above the images. From **a** to **e** a transition from a low-density to a high-density  $(2 \times 2)$  superstructure is monitored with dense bright rows starting to appear in **d**. In **f** a second phase is formed. All images are calibrated and corrected for thermal drift.

only coverages equivalent to Figure 7.1a and Figure 7.1f have been investigated.<sup>[100]</sup> As indicated by the red rectangles in this figure, a  $(2 \times 2)$  superstructure is observed at all coverages. However, there is a transition from an apparently low-density  $(2 \times 2)$



superstructure in Figure 7.1a and b to a dense ( $2\times 2$ ) structure in e. The structure in Figure 7.1e displays the already mentioned  $\alpha$  and  $\beta$  domains. This transition can be seen especially well in Figure 7.1d, where the first bright stripes of the dense structure start to appear.

Figure 7.1f is especially interesting if compared to Figure 7.1e, since it shows that after just five additional minutes of sublimation the second phase—known from literature<sup>[100]</sup>—already covers a large fraction of the surface. These results suggest that the second phase is formed by upright standing molecules and is not a second layer.<sup>a</sup> This is also supported by the fact that a transition from  $\alpha$  to  $\beta$  domains<sup>[100]</sup> can sometimes be noticed at this second phase (marked in Figure 7.1f): a closed layer of the ( $2\times 2$ ) structure (Figure 7.1e) does not display such transitions along the  $[010]$  direction and a second layer would probably not change that.

High-resolution images of the second phase reveal the structure that is identified

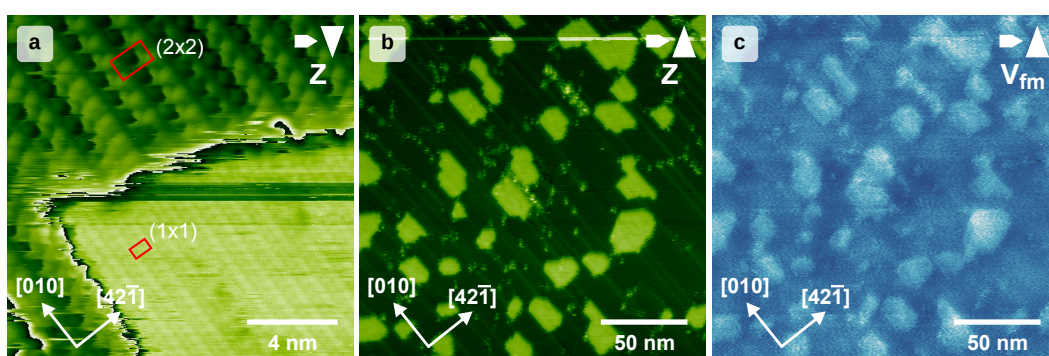


**Fig. 7.2:** High-resolution image of the second phase that is identified as a ( $1\times 1$ ) superstructure (a). The unit cells of both the ( $1\times 1$ ) and ( $2\times 2$ ) structures are marked with a red rectangle. This image is calibrated and corrected for thermal drift. The images in b and c display a larger area with several islands of the second phase. In c, the frequency-modulation Kelvin probe force microscopy (FM-KPFM) data show that the islands appear brighter, that is a more positive voltage needs to be applied at the tip to minimise electrostatic forces above the second phase islands, compared to the ( $2\times 2$ ) structure.

as a ( $1\times 1$ ) superstructure (Figure 7.2a). Also worth mentioning is the different frequency-modulation Kelvin probe force microscopy (FM-KPFM)<sup>[113]</sup> contrast in Figure 7.2c. The upright standing molecules appear about 0.6 V more positive. Nonetheless, it is not clear whether this signal is caused by crosstalk with the  $z$  channel, by the molecule orientation or by the molecule density. This may be an interesting question for the future.

At coverages lower than the one shown in in Figure 7.1a, the molecules form stripes along the  $[010]$  direction (Figure 7.3a). The mobile molecules seem to diffuse rapidly, as indicated by the horizontal lines in this image. Upon heating to 227 °C, the molecules do not desorb, but become immobile and create a less ordered structure. This is attributed to a deprotonation. The presumably deprotonated molecules are

<sup>a</sup>If it would be a second layer, it would grow slower (assuming a similar sticking coefficient for the second layer).

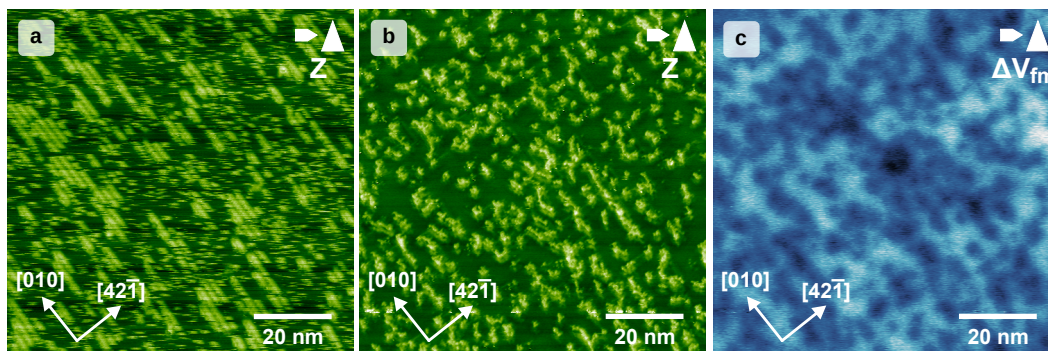


**Fig. 7.3:** Images of TPA after sublimation for 11 minutes at 132 °C with a new crucible. **b** was acquired after heating the sample to 227 °C at the manipulator. The corresponding KPFM error signal is shown in **c**, dark regions indicate a negative charge.

also visible in the KPFM error signal as negative compared to the calcite substrate similar to what has been reported for the deprotonation of 2,5-DHBA.<sup>[23]</sup> Inducing a deprotonation may be a promising way to stabilise molecules on a substrate. However, the structure prior to the deprotonation may not be preserved, like in this example. This finding also explains why temperature programmed desorption (TPD) measurements with low coverages of TPA were not successful<sup>[117]</sup>, because most molecules simply do not desorb below the decomposition temperature of calcite (between 600 K and 800 K). This problem may exist for other acids as well.

## 7.2 Controlling self-assembly: diffusion studies of terephthalic acid and its derivatives

Self-assembly is a rather complicated process requiring a subtle balance between energy barriers such as the barriers for diffusion, desorption or dissociation of non-equilibrium structures (see Chapter 2). To control self-assembly, it is necessary to understand how these energies can be tuned. In this section, the effect of different side groups on the diffusion barrier is studied. In the first part of this section this is done for TPA and BrTPA (with a bromo group). The second part contains a detailed analysis of diffusion and self-assembly of ATPA (with an amino group).

### 7.2.1 TPA and BrTPA at low temperatures

In order to study the influence of different functional groups on the diffusion barrier, the following approach was utilised: because self-assembly can only take place if the molecules can diffuse, the idea was to prepare a sample with a low coverage and increase the temperature until the first self-assembled structures are evident. To allow for the formation of self-assembled structures within observation time, an average jump frequency of more than about  $1 \times 10^{-3} \text{ s}^{-1}$  ( $\approx 8$  jumps on average within two hours) is required to create self-assembled structures.<sup>b</sup> Assuming an attempt frequency in the order of  $\frac{k_B \cdot T}{h} \approx 1 \times 10^{12} \text{ s}^{-1}$  and no major influence of entropy and knowing the temperature at which self-assembly is observed, it is possible to estimate the diffusion barrier using the Arrhenius equation (see Chapter 2 for details):

$$\Delta E_{\text{diff}} = \ln\left(\frac{\nu}{\nu_0}\right) \cdot k_B \cdot T \approx T \cdot 0.003 \frac{\text{eV}}{\text{K}}. \quad (7.1)$$

This simple estimate shows that at room temperature a diffusion barrier of about 0.9 eV is the maximum acceptable barrier that would still allow for self-assembly to happen within reasonable time to be observed in these measurements (in few hours). That being said, the measurements for the determination of the diffusion barrier using this simple approach proved to be quite complicated. Both TPA and BrTPA are extremely difficult to image at high-resolution, because tip changes occur frequently. They are attributed to molecules jumping to and from the tip. Therefore, the contrast is somewhat blurry for many tips and single molecules cannot be imaged most of the time. An additional problem is that TPA as well as BrTPA seem to form self-assembled structures below 140 K. Because the sample was prepared at the manipulator at about 85 K and then transferred with the wobble stick (precooled at the AFM stage at about 110 K when cooling with liquid nitrogen), the sample

---

<sup>b</sup>Several jumps are required for the molecules to meet and form structures. This frequency corresponds to what is found for the self-assembly of ATPA in Section 7.2.2, when the structure formation can just be observed.

warmed up during transfer. The temperature of the sample during transfer is not known, but first measurements with liquid nitrogen already showed self-assembled TPA stripes at 110 K, as it has been reported before.<sup>[115]</sup> To solve this problem, the AFM stage was cooled with liquid helium. Because it is not possible to cool the manipulator with liquid helium as well, the temperature of the sample was still at 85 K during preparation. Due to the more effective precooling of the wobble stick, the temperature rise during transfer was probably smaller. In Figure 7.4a and b,

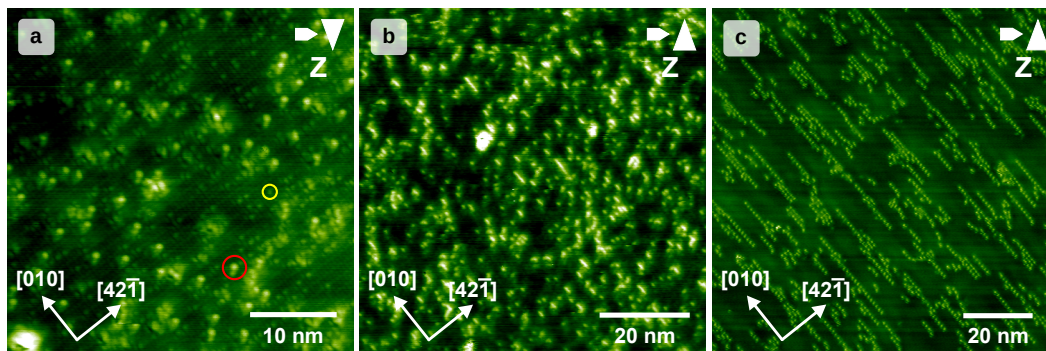


**Fig. 7.4:** TPA (a and b) and BrTPA (c) at low temperatures (sublimation at 133 °C for 3 min). Image a was recorded at 112 K and b at 142 K. The stage was cooled with liquid helium for these experiments. Image c is taken at 109 K (sublimation at 126 °C for 5 min), but the experiment was performed with liquid nitrogen. This means the sample warmed up to an unknown temperature during transfer between manipulator and AFM stage and the true temperature required for self-assembly may be higher. In both b and c molecular stripes are detectable. In a two species can be identified: what is assigned to be TPA is marked with a red circle, the small molecules (one marked with a yellow circle) may be water.

images of TPA taken at different temperatures are presented. While until 127 K<sup>c</sup> no stripes are visible, they appear at 142 K. That means self-assembly starts around  $(135 \pm 8)$  K corresponding to a diffusion barrier of about 0.4 eV (using Equation 7.1). However, it should be noted that in Figure 7.4a small molecules (marked with a yellow circle) are detected besides TPA molecules. These have been observed for TPA at low temperatures before<sup>[115]</sup> and are possibly water. It is not clear how they influence the diffusion process.

For BrTPA measurements were performed with liquid nitrogen only. Figure 7.4 reveals that even at 109 K self-assembled structures are recognised. Like TPA, BrTPA forms stripes at low temperatures, in contrast to the island structures observed at room temperature.<sup>[101]</sup> The true upper temperature limit for the assembly of stripes is higher than 109 K due to the transfer procedure. Assuming an upper limit of 150 K, the diffusion barrier is less than 0.45 eV. Accordingly, the bromo group does not increase the diffusion barrier noticeably. It could also well be that it decreases the barrier.

<sup>c</sup>Due to the better quality, an image acquired at 112 K is shown.

## 7.2.2 Characterising diffusion in detail and monitoring self-assembly with molecular resolution: ATPA at low temperatures

While forming stripes<sup>[112]</sup> like TPA or BrTPA, ATPA creates self-assembled structures at much higher temperatures, that is between 220 K and 240 K corresponding to a diffusion barrier of about 0.7 eV. Accordingly, the amino group increases the interaction between surface and molecule.<sup>d</sup> This implies that adding an amino group is a promising strategy to enhance the anchoring of molecule to the calcite(104) surface. Furthermore, the molecule is a little bit easier to image than TPA or BrTPA, since contrast changes are less frequent. Thus, it was possible to characterise diffusion in more detail. Similar to Section 6.3, single diffusing molecules were imaged to perform motion tracking (for details, see Section 6.3). Unfortunately, this is much more difficult in this case as compared to measurements with 2,5-DHBA, because ATPA creates self-assembled structures even at low coverages. The dilemma is that on one hand the coverage should not be too high for imaging freely diffusing molecules and to slow down nucleation, but on the other hand at low coverages most molecules sit at what is interpreted as defects, do not move and the number of diffusing molecules is too low for a statistical evaluation. Besides, recording an image series requires more than three hours from the point of preparation. To perform diffusion measurements, it is required that individual molecules still exist on the surface even after this time. This makes finding the right combination of temperature and coverage challenging. Several unsuccessful tries resulted in imaging

<sup>d</sup>The binding energy to the surface and the diffusion barrier are, of course, two different quantities. However, they are usually loosely correlated.<sup>[126]</sup>

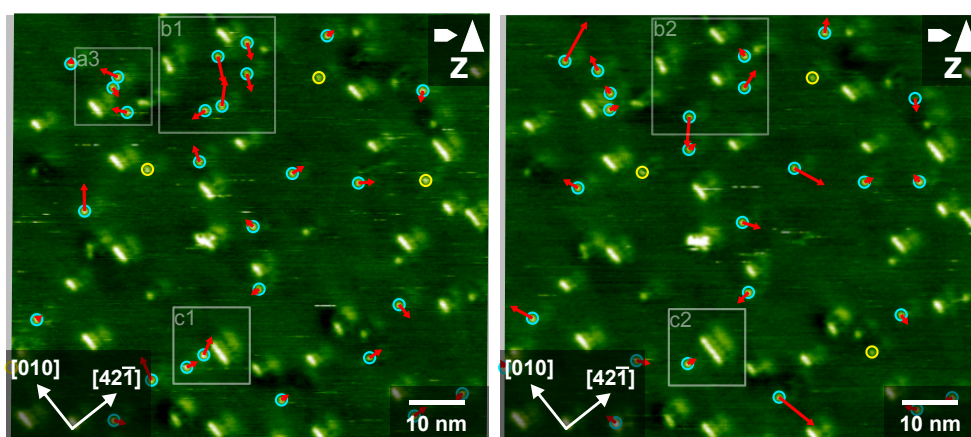


**Fig. 7.5:** Two consecutive images of a series at 245 K with a total sublimation time of 30 s at 122 °C. Moving molecules are marked with a turquoise circle and the position in the next image is indicated with a red arrow. Yellow marked molecules do not move now, but later in the series. Both images are transformed to match the last image of the series. The boxes mark the positions of the image sections in Figure 7.7. The complete series can be found in the appendix, Section 10.4.

too little or no diffusing molecules—that is if the drift was linear and there were no tip changes during imaging.

Finally, one image series with more than twenty moving molecules was acquired by increasing the coverage of a sample with four diffusing molecules per 100 nm<sup>2</sup> by 50% by sublimating again. The result is presented in Figure 7.5.

Like for 2,5-DHBA, the density map of the motion vectors (Figure 7.6) reveals the jump directions and jump lengths. The molecules move along the main symmetry directions of calcite(104), but two calcium-calcium distances each.

Along the  $[42\bar{1}]$  direction, the distance is about 8 Å, which is the size of the unit cell in this direction. This also corresponds to the next identical adsorption position. For the  $[010]$  direction, the distance is twice the unit cell dimension, that is roughly 10 Å. It is not clear why the molecules do not prefer next-neighbour jumps along  $[010]$ . It is interesting to note that the diffusion direction and jump length are different for the two molecules investigated so far. Accordingly, not only the diffusion barrier, but also the diffusion mechanism can be very diverse for different molecules. This has been shown

before for the jump length of large organic molecules on metals, demonstrating that

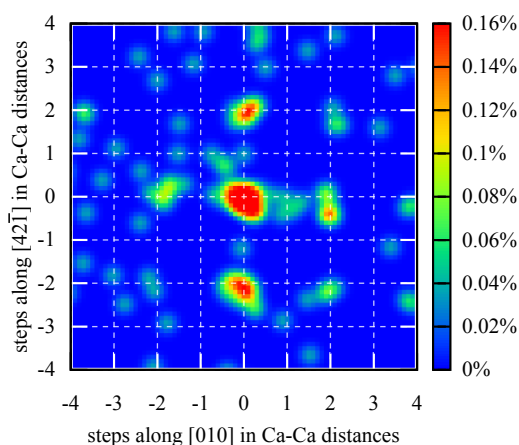


**Fig. 7.6:** Plot of the motion vector density mapped to the main calcite directions  $[010]$  and  $[42\bar{1}]$ .

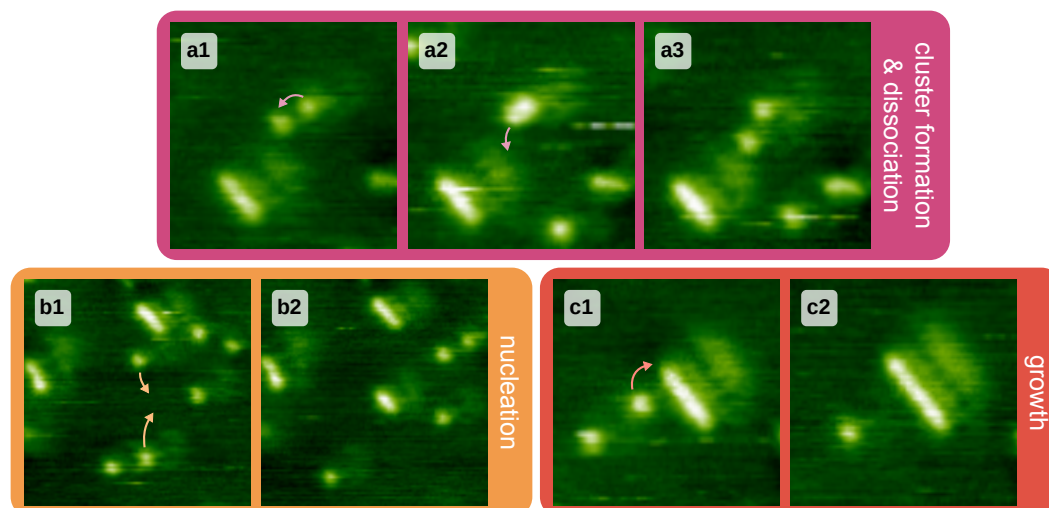


**Fig. 7.7:** Image sections of different processes discovered in the image series shown in Figure 7.5. The processes are formation and dissociation of an unstable cluster (a), nucleation (b) and growth (c). The images display artefacts caused by a double tip.

it is also possible to tune the diffusion mechanism via molecule functionalisation.<sup>[20]</sup>

Moreover, it was possible to observe the self-assembly process at molecular resolution. Figure 7.7 shows enlarged consecutive image sections from the image series. The position of five of these sections is marked in Figure 7.5. The formation of unstable clusters and their dissociation is imaged in Figure 7.7a. It is apparent that the molecules are not aligned to the direction of the stripes and, therefore, do not form a stable structure. Figure 7.7b displays the nucleation of a stripe. Stripes consisting of two molecules do not dissociate within the image series, indicating that the critical cluster size, that is the maximum size of an unstable cluster, is one if the molecules form a stripe. In Figure 7.7c, the growth of a stripe consisting of four molecules is demonstrated. To the best of the author's knowledge, this is the first time the self-assembly process of molecules on a surface has been imaged directly.

## 7.3 Conclusion

In conclusion, the technique introduced in Section 6.3 was successfully applied to an image series of ATPA. The density map of motion vectors reveals that the diffusion takes place along the main calcite directions in this case. Along the  $[42\bar{1}]$  direction, the molecules jump to the next equivalent position, while along the  $[010]$  direction the molecules perform next-neighbour-but-one jumps. Besides diffusion, all processes important for self-assembly have been observed. These are nucleation, growth and the formation and dissociation of unstable clusters.

While a bromo group did not increase the anchoring of the molecule, an amino group apparently did. The diffusion barrier of ATPA is about 0.3 eV higher than for TPA. All three molecules form stripes at low temperatures, indicating that the functional groups did not influence the type of structures. Hence, it is possible to increase the molecule-surface interaction without changing the self-assembled structures by choosing the proper molecule.

Additionally, it is shown that inducing a deprotonation can also stabilise structures on a surface. In this study, the stabilisation is such that the molecules do not desorb prior to the decomposition of calcite.





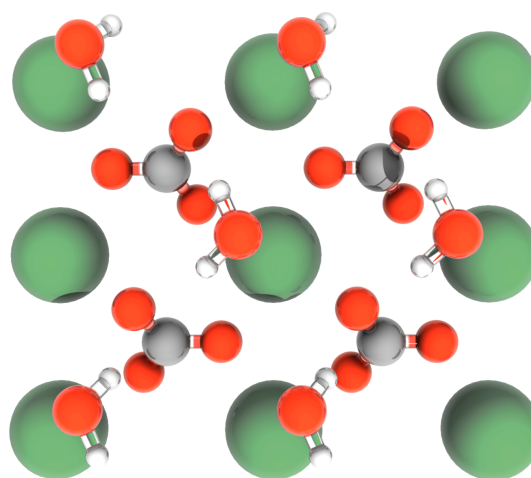
## Water on calcite(104)

Calcite is an abundant mineral in nature. Several marine organisms incorporate calcite to form, for instance, nacre. Calcite is also part of the inanimate matter and forms, for example, in kettles as scale.

Both of these examples for the occurrence of calcite in nature involve a liquid environment. In many cases, the first water layer on a surface is the structural template that mediates aqueous interfacial chemical reactions, governs ice nucleation and other processes.<sup>[127]</sup>

Therefore, the calcite-water interface is an interesting subject to study. While the structure of the first water layers on calcite in liquid environment has been resolved in recent works<sup>[128]</sup>, little is known about the calcite-water interface in UHV so far. Ab initio calculations of the first monolayer of water on calcite(104) have been performed already<sup>[26]</sup> that have not been compared to experiment yet. Also, temperature-programmed desorption (TPD) spectra for different coverages have been recorded recently.<sup>[117]</sup>

In this chapter, the structures formed by dosing sub-monolayer coverages of water on to calcite(104) at low temperatures in UHV are examined. But first, important results of TPD measurements that have been performed in [117] are summarised.



## 8.1 Temperature-programmed desorption measurements

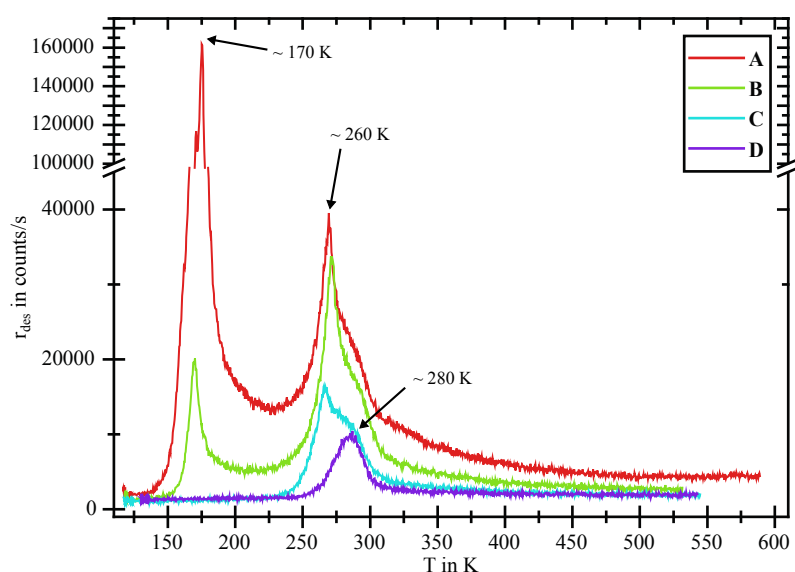


**Fig. 8.1:** Temperature-programmed desorption (TPD) spectra of water on calcite(104) acquired with a heating rate of 1 K/s. The measurements were performed with different coverages decreasing from **A** to **D**. Adapted with permission from [117].

TPD is a powerful technique for measuring the desorption kinetics of molecules from surfaces by monitoring the desorption rate while ramping up the temperature of the sample. Experiments performed by Barbara Heep (Figure 8.1) have detected a double desorption peak at 260 K and 280 K besides a multi-layer peak<sup>a</sup> at 170 K.<sup>[117]</sup> For low coverages, only one peak at 280 K has been observed. Accordingly, this peak is formed by the molecules within the first adsorption layer. The double peak at higher coverages has been fitted with two Gaussians, revealing that the area of the peak at 260 K and of the peak at 280 K is about the same.<sup>[117]</sup> Because the area of a peak corresponds to the number of molecules, this raises the question whether the peak at 260 K originates from a second water layer or from a second species in the first layer. This question will be answered in the next section.

<sup>a</sup>This peak is caused by higher layers and not relevant for this chapter.

## 8.2 FM-AFM measurements

First NC-AFM measurements in UHV were performed after dosing water on to a cold calcite surface (85 K) at  $2 \times 10^{-9}$  mbar for 30 s and measuring at a stage temperature of 110 K. In Figure 8.2, a  $(2 \times 1)$  superstructure is identified, which is formed by stripes along the  $[42\bar{1}]$  direction. Interestingly, a second, dense structure coexists that is marked with arrows in the figure. One of these structures could be formed by the species desorbing at 260 K. To get a clearer picture of the adsorption process, an experiment with increasing coverages was performed starting with a sublimation time of 15 s (Figure 8.3). Note that sublimation times of different experiments cannot be compared directly, because sublimation times are rather short and regulating the pressure manually by opening

and closing the valve is rather imprecise. The temperature of the AFM stage was kept at 140 K for these experiments for practical reasons.<sup>b</sup> Figure 8.3a reveals that at low coverages two different species can be observed: small protrusions with rather weak contrast and larger bright protrusions. Because the small protrusions are the smallest observed motive, they are interpreted as single water molecules (monomers). Judging from the size compared to the small protrusions, the larger protrusions may be dimers. Notably, every second calcite row along  $[010]$  in Figure 8.3a is not occupied and a kind of  $(2 \times 1)$  superstructure is already evident. In Figure 8.3b, the scanned surface is almost completely covered with a  $(2 \times 1)$  superstructure. Upon increasing the coverage, molecules start to arrange in a dense structure that is identified as a  $(1 \times 1)$  superstructure in Figure 8.3c. At a coverage roughly equivalent to twice the coverage of Figure 8.3b, almost all of the surface is covered with the  $(1 \times 1)$  superstructure (Figure 8.3d). Some molecules on top of the dense structure are visible. The horizontal lines in the image may be caused by diffusing molecules, which may be an indication that the interaction between the first layer and the second layer is rather weak.

These results suggest that the two TPD peaks at 260 K and 280 K (Figure 8.1) are caused by the  $(1 \times 1)$  and  $(2 \times 1)$  structures, respectively.

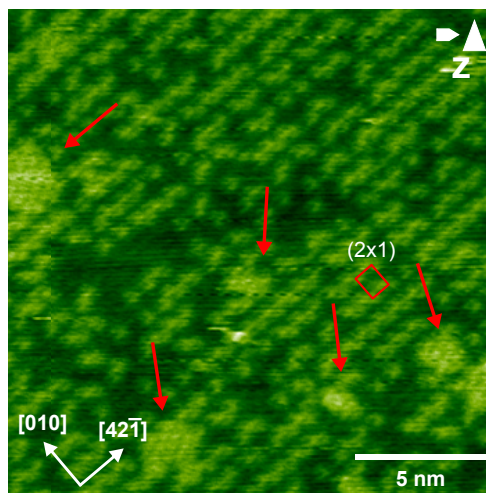


**Fig. 8.2:** Image of the calcite(104) surface at 110 K after dosing water for 30 s at  $2 \times 10^{-9}$  mbar. The  $(2 \times 1)$  superstructure is marked with a rectangle. Arrows indicate the positions where the dense structure is evident. The image is calibrated and corrected for thermal drift.

<sup>b</sup>The heater feedback loop range is larger for higher temperatures and, therefore, it is easier to keep the temperature constant.

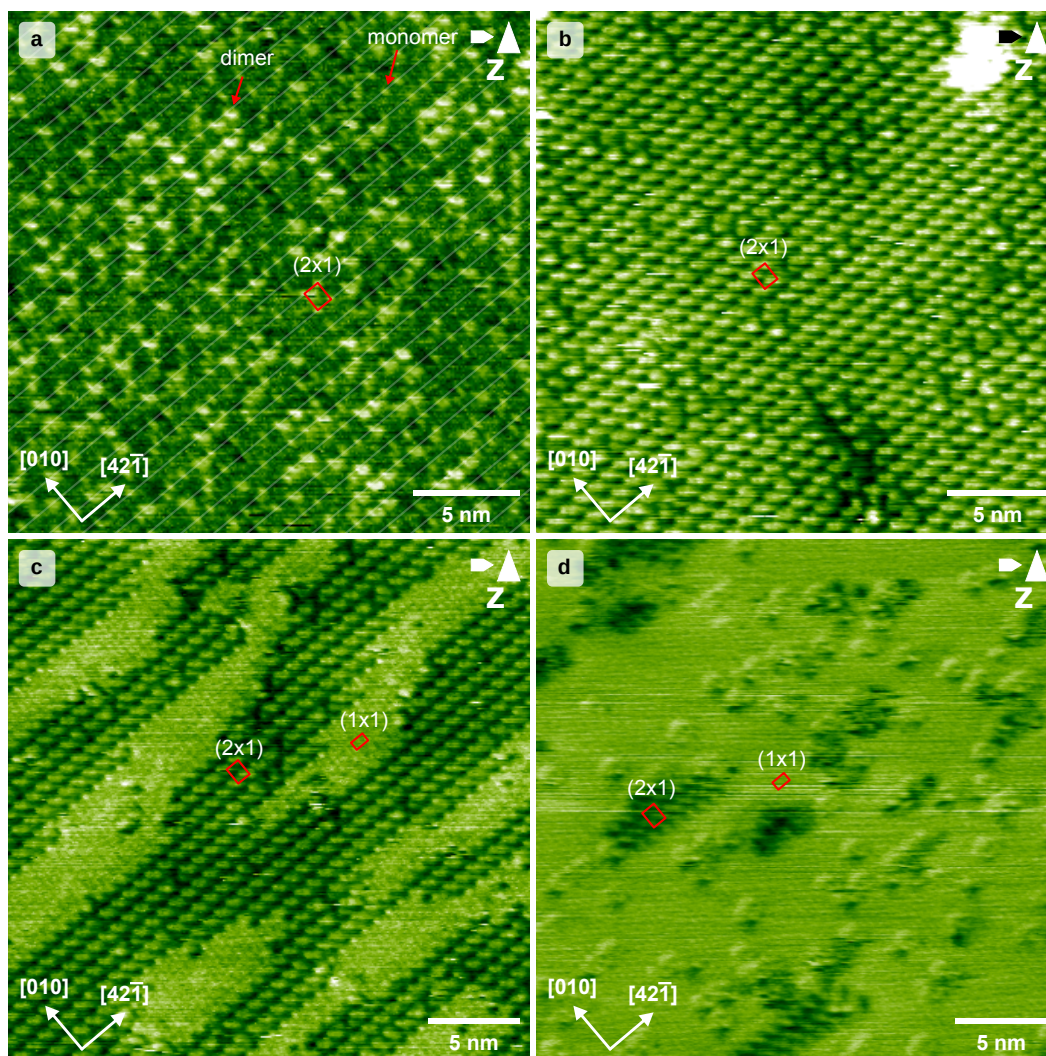


**Fig. 8.3:** Different coverages of  $\text{H}_2\text{O}$  on calcite(104). The sublimation times were 30 s (a), 60 s (b), 80 s (c) and 125 s (d) at  $2 \times 10^{-9}$  mbar. In a, only every second row along  $[010]$  is occupied (marked with a grid) and even at this very low coverages, a  $(2 \times 1)$  superstructure is observed. The unit cells are marked with rectangles. A dense  $(1 \times 1)$  structure starts to appear at high coverages and is marked in c and d. All four images are calibrated and corrected for drift.

Additionally, it is very interesting that a  $(2 \times 1)$  superstructure is observed at low coverages. Because intermolecular interactions usually lead to the formation of self-assembled structures, it does not make sense that a structure with large distances between the molecules is preferred to the dense structure observed at high coverages at first glance. One explanation would be repulsion between the molecules. However, this would not explain why only every second row along  $[010]$  is not occupied (Figure 8.3a). A larger spacing would be expected sometimes as well. If it is not the molecule-molecule interaction, it needs to be the molecule-surface interaction that causes this behaviour. The explanation could be that the surface displays a  $(2 \times 1)$  reconstruction, which has been frequently observed for calcite(104) before.<sup>[16]</sup> The superstructure would then just reflect the surface structure. It could also be that

water induces a  $(2\times 1)$  reconstruction of the surface.

The TPD measurements (Figure 8.1) suggest that the desorption of water from the first layer starts at about 220 K.<sup>c</sup> To check the validity of the assumption

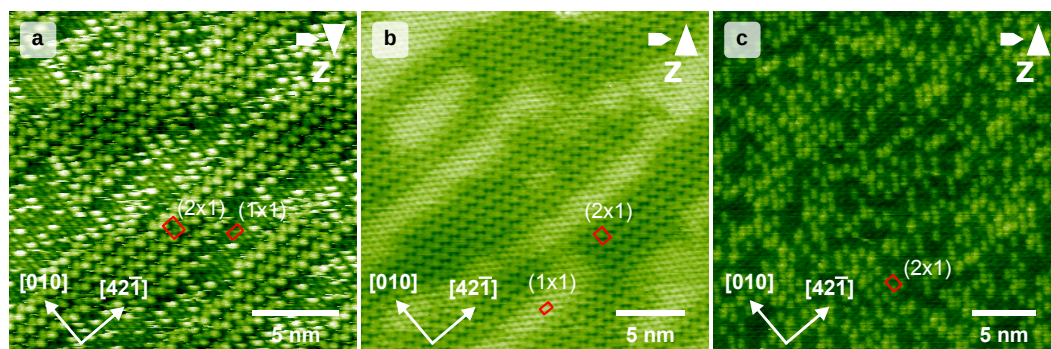


**Fig. 8.4:** Images from the surface after dosing water for 120 s at  $2 \times 10^{-9}$  mbar (**a** and **b**) and after heating to 220 K for one hour (**c**). Images **a** and **b** display a contrast inversion.<sup>[129]</sup> All images acquired at 140 K, calibrated and corrected for drift.

that the two peaks are caused by the first monolayer, a sample with a rather high coverage (Figure 8.4a and b) was heated to 220 K at the AFM stage for one hour and cooled down again afterwards. As illustrated by Figure 8.4c, the coverage decreased noticeably during this procedure. The  $(1\times 1)$  superstructure can no longer be observed and an imperfect layer of the  $(2\times 1)$  superstructure remains.

It is noteworthy that these AFM images alone do not prove that the molecules in the  $(1\times 1)$  superstructure desorb first, since the  $(2\times 1)$  superstructure may form at a certain coverage no matter which molecules desorbed. However, it is evident that molecules from the  $(2\times 1)$  structure which forms at low coverages desorb last (Section 8.1) and in combination with the two peaks in the TPD spectra it can be deduced that the molecules from the  $(1\times 1)$  superstructure desorb first indeed.

<sup>c</sup>This is where desorption can just be detected by the mass spectrometer, that is the beginning of the peak. At room temperature, all water molecules desorb, which was confirmed by NC-AFM measurements.

## 8.3 Structural model and comparison with literature

The resolution of the image in Figure 8.4a is good enough for a comparison with the theoretical calculations in [26]. Figure 8.5a shows an image section of the dense  $(1 \times 1)$  superstructure in Figure 8.4b together with the structure for a complete monolayer predicted by [26]. The calculation is in agreement with the observed structure which is formed by zig-zag lines of water molecules along  $[42\bar{1}]$ . Accordingly, the number

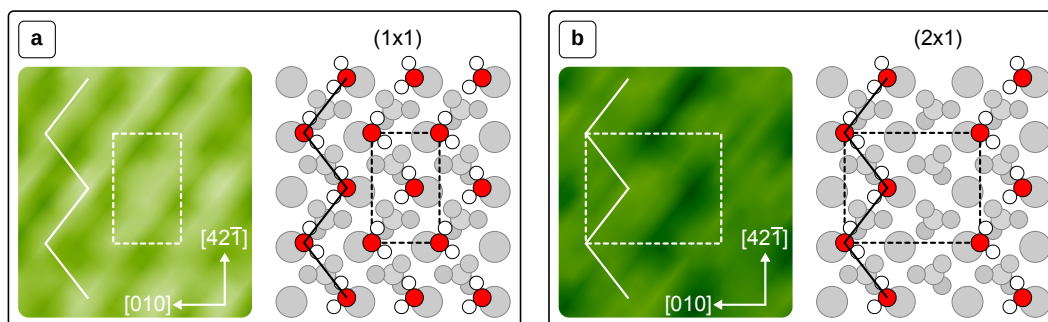


**Fig. 8.5:** AFM images and structural models of the  $(1 \times 1)$  (a) and  $(2 \times 1)$  (b) superstructure of water on calcite. The AFM images are sections from Figure 8.4b. In a the structural model corresponds to the result of the calculations in [26]. On the contrary, the model in b is just a proposal made by removing one of the zig-zag lines of water molecules in a.

of molecules per unit cell is two. For the  $(2 \times 1)$  structure (Figure 8.5b), a structure is proposed here that consists of zig-zag lines as well, but with unoccupied lines in between. As a result, the molecule density of this structure is just the half, which fits to the measurements of different coverages in Figure 8.3.

Interestingly, the structure of the complete monolayer is very similar to what has been observed for the first monolayer of water on calcite in liquid environment.<sup>[128]</sup> This is readily explained by the strong interaction between the first monolayer and the substrate, which is apparent from the high desorption temperature and confirmed by the theoretical calculations.<sup>[26]</sup> Apparently, the interaction between the first monolayer and the substrate is so strong, that additional water layers do not alter the structure.

## 8.4 Conclusion

AFM measurements revealed the superstructure of a sub-monolayer H<sub>2</sub>O on calcite(104) at low temperatures, namely a (2×1) structure for low and in addition a (1×1) structure for high coverages. The (1×1) structure has been predicted by theoretical calculations<sup>[26]</sup> and is identical to what has been observed for the first monolayer of water on calcite in liquid environment.<sup>[128]</sup> The existence of a (2×1) structure for low coverages is a bit surprising, because self-assembled structures are usually governed by intermolecular interaction, which is weaker for larger distances between molecules and generally favours dense structures with little spacing. However, for the present system the opposite is the case. The (2×1) structure with a gap between the molecule rows is preferred to the dense (1×1) structure. In this case, the (2×1) superstructure may be explained by the strong molecule-surface interaction in connection with a (2×1) surface reconstruction that has already been observed for calcite(104).<sup>[16]</sup> It could also be that this surface reconstruction is induced by water. These questions are currently being addressed by Ville Loukonen from Aalto University, Finland, who performs additional theoretical calculations for this very system.

These findings readily explain the observation of two desorption peaks at high temperatures in TPD measurements that now can be assigned to these two structures. Thus, AFM and TPD experiments proved to be a powerful combination for understanding the desorption process.





## Conclusion and outlook

In conclusion, this thesis investigates several aspects of self-assembly and diffusion of molecules on the insulating calcite(104) surface in ultra-high vacuum using frequency-modulation atomic force microscopy with molecular resolution. Highlights include the development of a post-processing procedure to evaluate short image series of diffusing molecules distorted by thermal drift (Sections 6.3 and 5.1), the first direct observation of the self-assembly process (Section 7.2.2) and the imaging of water at sub-monolayer coverages (Chapter 8).

This thesis presents systems that demonstrate the importance of the diffusing species. Measurements of 2,5-dihydroxybenzoic acid (2,5-DHBA, Chapter 6) reveal that a large fraction of molecules is diffusing at room temperature. The diffusing molecules are too fast to be detected at room temperature and the sample needs to be frozen for observing this species. It is also discovered that at low coverages all molecules are diffusing at room temperature and molecular islands form only upon reaching a certain threshold. This underlines the importance of both temperature and coverage for self-assembly.

Furthermore, the diffusion process of single 2,5-DHBA molecules is studied at low temperatures. Using motion tracking, a post-processing algorithm is introduced allowing for a very precise drift correction (Section 5.1). Even with a small number of images at a rather large scale (100 nm × 100 nm), it is possible to extract the diffusion directions and jump length. For 2,5-DHBA, the molecules diffuse one step diagonal to the main directions. Here, it was disclosed that the molecules jump along directions diagonal to the main symmetry directions of calcite(104), which is in sharp contrast to the initial assumption of the molecules moving along the main symmetry directions. This provides essential input for theoretical calculations of the diffusion barrier. Therefore, the diffusion analysis presented in this thesis should be performed prior to running such calculations.

It is also shown that a determination of the diffusion barrier and the attempt frequency is possible using the post-processing procedure introduced in this thesis, although the number of diffusion rate measurements for different temperatures is still low and more values would be needed for a significant result.

In Chapter 7, the structures of terephthalic acid (TPA) on calcite(104) at different coverages are presented. These results suggest that the molecules lie flat first and stand upright at high coverages, forming island-like structures.

It is also shown that terephthalic acid deprotonates upon heating to 500 K and does not desorb from the surface. Hence, deprotonation is identified as a promising strategy to anchor molecules on calcite.

Another strategy for increasing the molecule-surface interaction is tuning the anchoring by variation of functional groups which is investigated for aminoterephthalic acid (ATPA) and bromoterephthalic acid (BrTPA). This is done by sublimation on a cold substrate and finding the temperature at which the molecules start to move and form self-assembled structures within the observation time. While TPA and BrTPA start to diffuse at very low temperatures below 150 K, it is found that the diffusion of ATPA first becomes observable at about 240 K. Accordingly, the diffusion barrier of ATPA is higher than for TPA. Notably, both TPA and ATPA form stripes, which shows that it is possible to change the diffusion properties without changing the type of self-assembled structures if selecting the proper molecules. For ATPA a detailed study of the diffusion is performed using the same procedure as for 2,5-DHBA. Additionally, the whole self-assembly process consisting of the formation and dissociation of unstable clusters, nucleation and growth is directly followed in a series of images. Although this mechanism is known, this is to the best of the author's knowledge the first time that these processes are imaged directly.

The last chapter (Chapter 8) is a study of the adsorption of the first water layer on calcite(104) at low temperatures. High-resolution images reveal two superstructures for low and high coverages. In particular, these measurements may serve as a benchmark for simulations and help to understand the calcite-water interface at a small scale.

To sum up, it will be interesting to see how the results and techniques presented in this thesis may contribute to future research. Especially the diffusion analysis method presented in Sections 6.3 and 5.1 may be applied to other questions such as how other organic molecules diffuse on calcite and how different side groups alter the diffusion direction and step length.

## Appendix

### 10.1 Change of the resonance frequency

The differential equation for the cantilever close to a sample is

$$m^* \cdot \ddot{x} = -(k^* - k_{\text{TS}}) \cdot x + F_0 \quad (10.1)$$

(Section 3.1). A solution of this differential equation is

$$x(t) = A \cdot \sin(\omega t) + \frac{F_0}{k^* - k_{\text{TS}}}. \quad (10.2)$$

Inserting Equation 10.2 into the left side of Equation 10.1 yields

$$m^* \cdot \ddot{x} = -m^* \cdot \omega^2 \cdot A \cdot \sin(\omega t) \quad (10.3)$$

which can be transformed using Equation 10.2 to

$$m^* \cdot \ddot{x} = -m^* \cdot \omega^2 \cdot \left( x - \frac{F_0}{k^* - k_{\text{TS}}} \right). \quad (10.4)$$

Equation 10.1 can be rearranged to

$$m^* \cdot \ddot{x} = -(k^* - k_{\text{TS}}) \cdot \left( x - \frac{F_0}{k^* - k_{\text{TS}}} \right). \quad (10.5)$$

Now, combining Equations 10.5 and 10.4 yields

$$-m^* \cdot \omega^2 \cdot \left( x - \frac{F_0}{k^* - k_{\text{TS}}} \right) = -(k^* - k_{\text{TS}}) \cdot \left( x - \frac{F_0}{k^* - k_{\text{TS}}} \right). \quad (10.6)$$

From this it follows that

$$\omega = \sqrt{\frac{k^* - k_{\text{TS}}}{m^*}}. \quad (10.7)$$

## 10.2 Substrate and molecules

The following figures are an alternative version of Figure 4.1 (Figure 10.1) and the Arrhenius plots from sublimation experiments with TPA, ATPA and BrTPA using *Justin* (Figure 10.2).

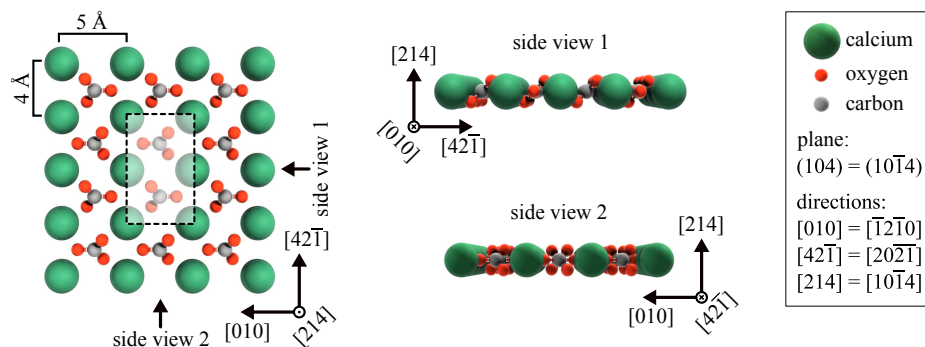


**Fig. 10.1:** Alternative version of Figure 4.1 made with *Blender*.

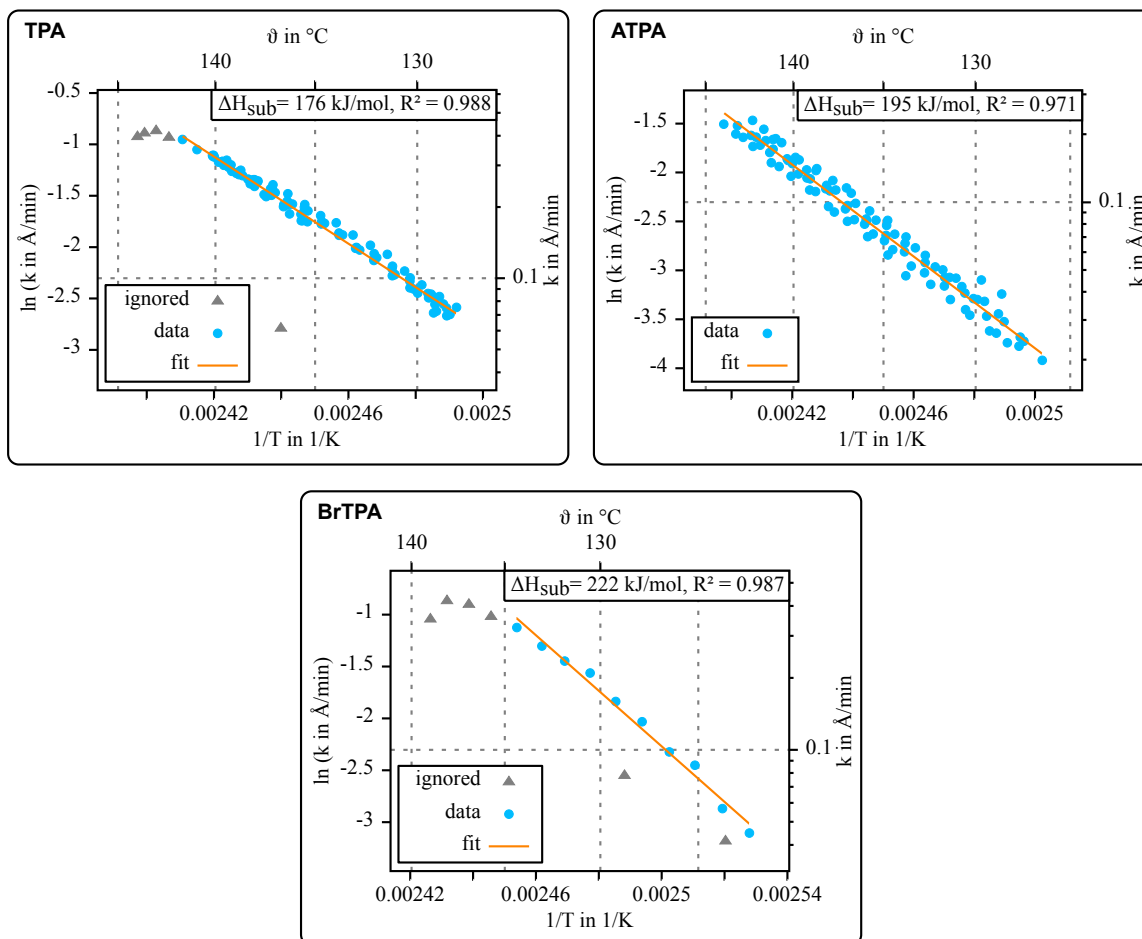


**Fig. 10.2:** Arrhenius plots for the determination of the sublimation enthalpy for TPA, ATPA and BrTPA measured using *Justin*.

## 10.3 2,5-DHBA

### 10.3.1 The $c(4\times 2)$ phase

The  $c(4\times 2)$  phase is rather difficult to image, since the contrast of the probably flat lying molecules is usually weak. At room temperature it was not observed at all. However, Figure 10.3 shows that the  $c(4\times 2)$  phase is observed just at the side in growth direction along  $[010]$  of each island for the dense phase islands. Therefore, it may be that the formation of this  $c(4\times 2)$  phase influences the island growth. One possibility is that it always forms prior to growth, another that it slows down or prevents growth. It may also be possible that the  $c(4\times 2)$  phase is not stable at elevated temperatures and only forms when cooling down the sample.

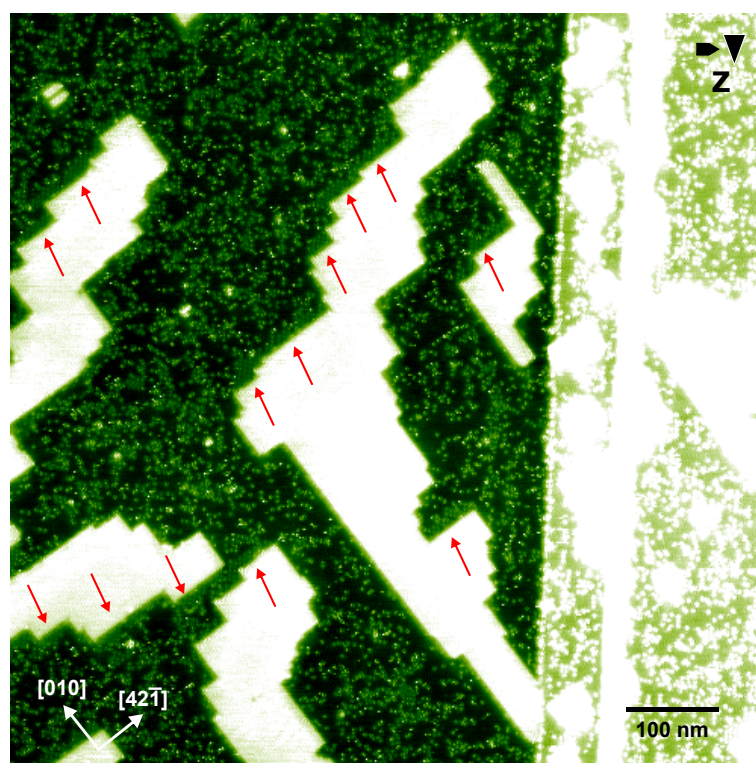


**Fig. 10.3:** Image of several dense phase islands with the  $c(4\times 2)$  superstructure next to the islands. Note that the  $c(4\times 2)$  structure is only found at the direction of growth along  $[010]$  (red arrows). The temperature for this measurement was 185 K. Due to the weak contrast, the  $c(4\times 2)$  phase may not be visible in a printed version. Please use the digital version in this case.

### 10.3.2 Deriving the binomial distribution for a random walk

The probability mass function for the binomial distribution with  $n \in \mathbb{N}$  tries,  $k$  successes and the probability for a successful event  $p$  is:

$$B(k, n) = \binom{n}{k} \cdot p^k \cdot (1 - p)^{n-k} \text{ with } k = 0, 1, \dots, n. \quad (10.8)$$

In one dimension, molecules can move to the right or to the left. The probability  $p$  for both events is 0.5 respectively, since hopping to the left and right is equally likely. After  $n$  jumps the molecule can be found at the position  $d \in \mathbb{Z}$  that is the sum of the jumps to the right  $k$  minus the jumps to the left  $n - k$ :

$$d = k - (n - k) = 2k - n \Rightarrow k = \frac{d + n}{2}. \quad (10.9)$$

Now, the chance  $\beta$  to find a molecule at position  $d \in \mathbb{Z}$  becomes:

$$\beta(d, n) = \binom{n}{\frac{d+n}{2}} \cdot \left(\frac{1}{2}\right)^n = \frac{n!}{\left(\frac{d+n}{2}\right)! \cdot \left(n - \frac{d+n}{2}\right)!} \cdot \left(\frac{1}{2}\right)^n. \quad (10.10)$$

Note that for an even number of jumps  $n$  only even values of  $d$  are possible (and for odd  $n$  only odd  $d$ ). This is because, for example, after one jump there is no possibility to stay at zero. Also  $\beta(d, n) = \beta(-d, n)$ , since the distribution is symmetrical. Therefore, we can write:

$$\beta(d, n) = \frac{n!}{\left(\frac{|d|+n}{2}\right)! \cdot \left(n - \frac{|d|+n}{2}\right)!} \cdot \left(\frac{1}{2}\right)^n. \quad (10.11)$$

### 10.3.3 Deriving the Poisson distribution for the number of jumps

We assume that molecules on a surface oscillate with some very large frequency (in order of the phonon frequency  $\frac{k_B \cdot T}{h} \approx 1 \times 10^{12} \text{ s}^{-1}$ ). A very small fraction of those oscillations leads to a jump. The chance to jump after a certain amount of oscillations could be calculated using the binomial distribution (Eq. 10.8). But because the number of tries  $n$  is large and the chance for success  $p$  is very small, we can calculate the limit of the binomial distribution

$$\lim_{\substack{p \rightarrow 0 \\ n \rightarrow \infty}} B(k, n) = \frac{(n \cdot p)^k}{k!} \cdot e^{-n \cdot p} \quad (10.12)$$

with the average number of jumps  $\mu = n \cdot p$  within a certain time frame and the number of jumps  $k$ . This is the Poisson distribution and can be written as:

$$P(k, \mu) = \frac{\mu^k}{k!} \cdot e^{-\mu}. \quad (10.13)$$

Different derivations can be found in literature and on-line (search for *Poisson limit theorem*) and are, therefore, not reproduced here. In general the Poisson distribution can be applied if a certain amount of independent events happen in a certain observation time and the number of tries is large compared to the number of success.

### 10.3.4 Combining Poisson distribution and random walk

Now, we calculate the chance to find a molecule at position  $d \in \mathbb{Z}$  if the average number of jumps  $\mu$  is known. The chance to find a molecule at position  $d$  after  $n$  jumps is given by a binomial distribution  $\beta(d, N)$  (Equation 10.11). The chance for a molecule to perform  $N$  jumps for a known  $\mu$  is calculated with the Poisson distribution  $P(N, \mu)$  (Equation 10.13). Therefore, the chance to reach the position  $d$  with  $N$  jumps is:

$$p(d, N, \mu) = P(N, \mu) \cdot \beta(d, N). \quad (10.14)$$

Any position  $d$  can be reached only with  $N = 2j + |d|$  jumps with  $j \in \mathbb{N}_0$ , since an even distance to the origin requires an even number of jumps (and an odd distance an odd number of jumps) and at least  $|d|$  jumps are required to reach a position  $d$ . The chance to reach a position  $d$  is accordingly the sum over all possible numbers of jumps:

$$p(d, \mu) = \sum_{j=0}^{\infty} P(2j + |d|, \mu) \cdot \beta(d, 2j + |d|). \quad (10.15)$$

This can be written as:<sup>[121]</sup>

$$p(d, \mu) = \sum_{j=0}^{\infty} \underbrace{\frac{\mu^{2j+|d|}}{(2j+|d|)!}}_{\text{Poisson distribution}} \cdot e^{-\mu} \cdot \underbrace{\frac{(2j+|d|)!}{\binom{|d|+2j+|d|}{2}! \cdot \binom{2j+|d|}{2}!}}_{\text{binomial distribution}} \cdot \left(\frac{1}{2}\right)^{2j+|d|} \quad (10.16)$$

$$= \sum_{j=0}^{\infty} \frac{\mu^{2j+|d|}}{(2j+|d|)!} \cdot e^{-\mu} \cdot \frac{(2j+|d|)!}{(j+|d|)! \cdot j!} \cdot \left(\frac{1}{2}\right)^{2j+|d|} \quad (10.17)$$

$$= e^{-\mu} \sum_{j=0}^{\infty} \left(\frac{\mu}{2}\right)^{2j+|d|} \cdot ((j+|d|)! \cdot j!)^{-1} \quad (10.18)$$

$$= e^{-\mu} \cdot I_{|d|}(\mu) \quad (10.19)$$

with the modified Bessel function of the first kind and  $n$ th order  $I_n(x)$ .

### 10.3.5 Diffusion measurements—image series

These figures represent the image series from the diffusion measurements of 2,5-DHBA (Section 6.3) after processing with *TrackRead*. The colour code is:

- red: never moving.
- yellow: not moving from this to the next image.
- turquoise: moving (red arrow indicating the position in the next image).
- purple: cluster (ignored due to other molecules nearby).
- white: molecule in the last image.

For each image, the area of the last image is indicated by a black box. The images are sorted from left to right and top to bottom.

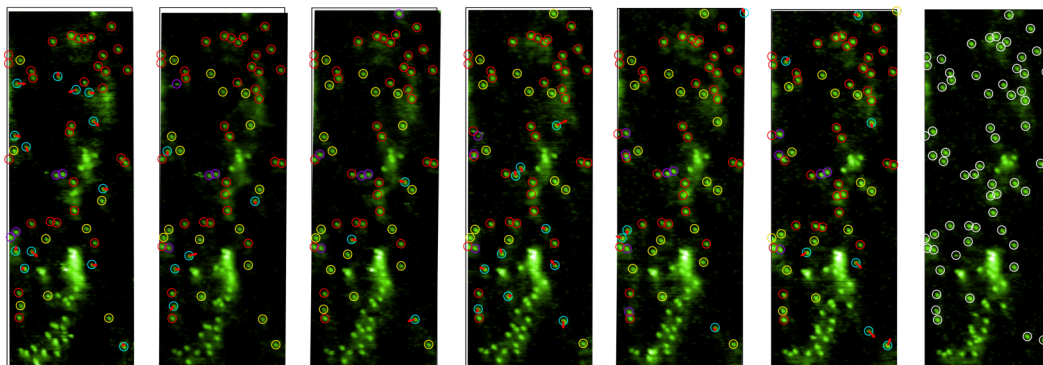


**Fig. 10.4:** Image series acquired at 185 K from the first measurement of 2,5-DHBA after processing with *TrackRead*.



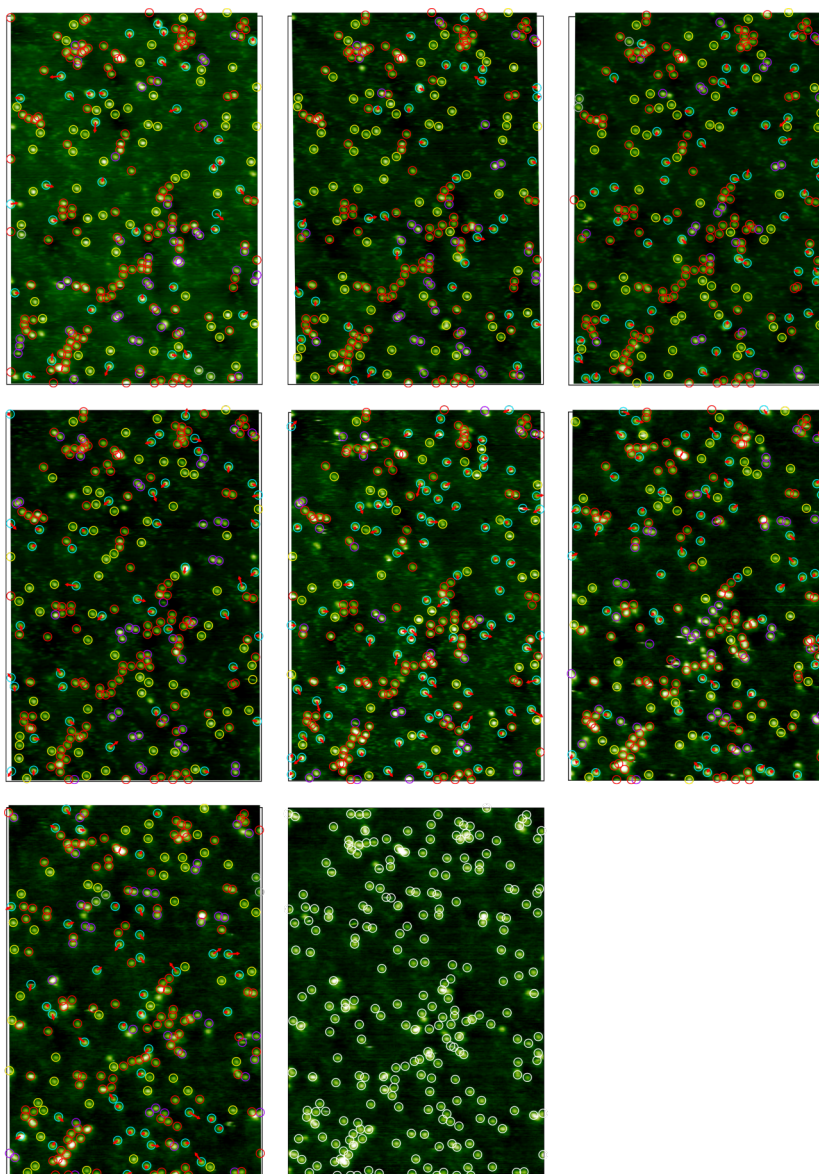


**Fig. 10.5:** Image series acquired at 189.5 K from the first measurement of 2,5-DHBA after processing with *TrackRead*.

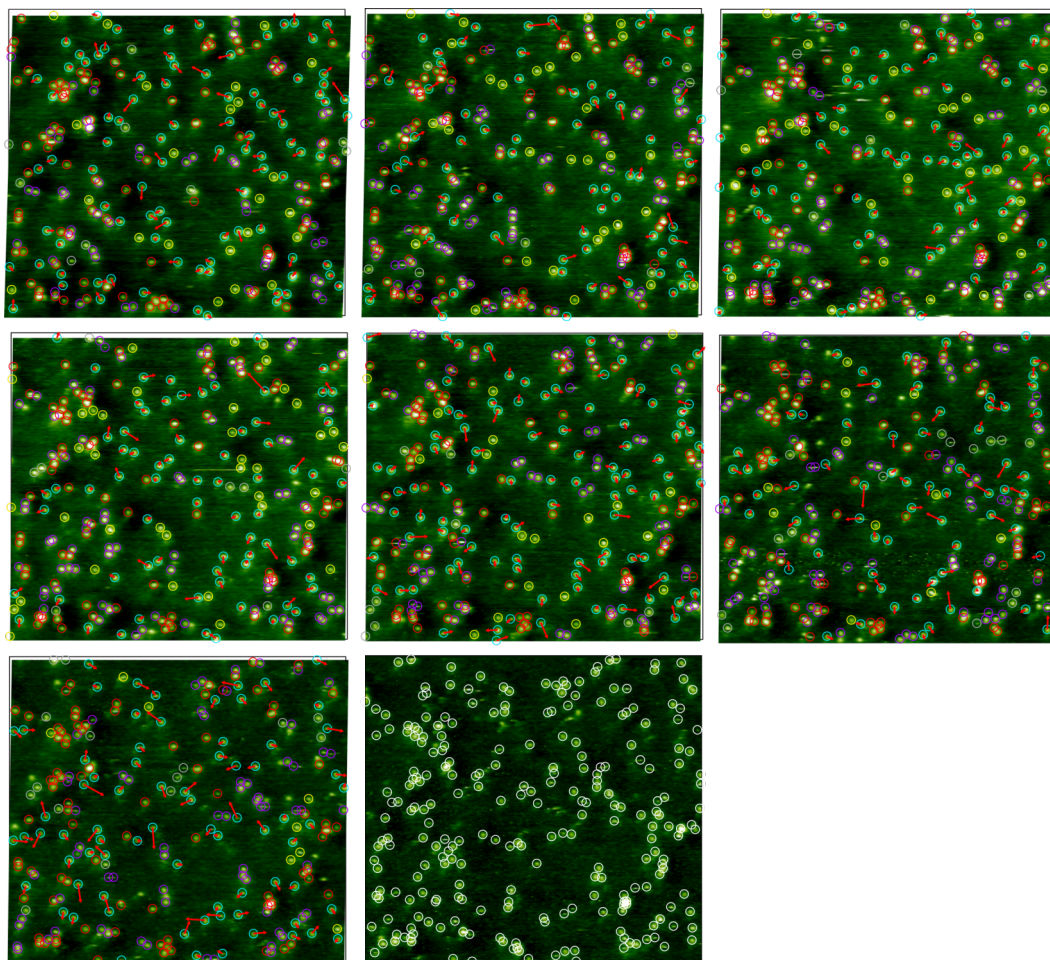


**Fig. 10.6:** Image series acquired at 194 K from the first measurement of 2,5-DHBA after processing with *TrackRead*.

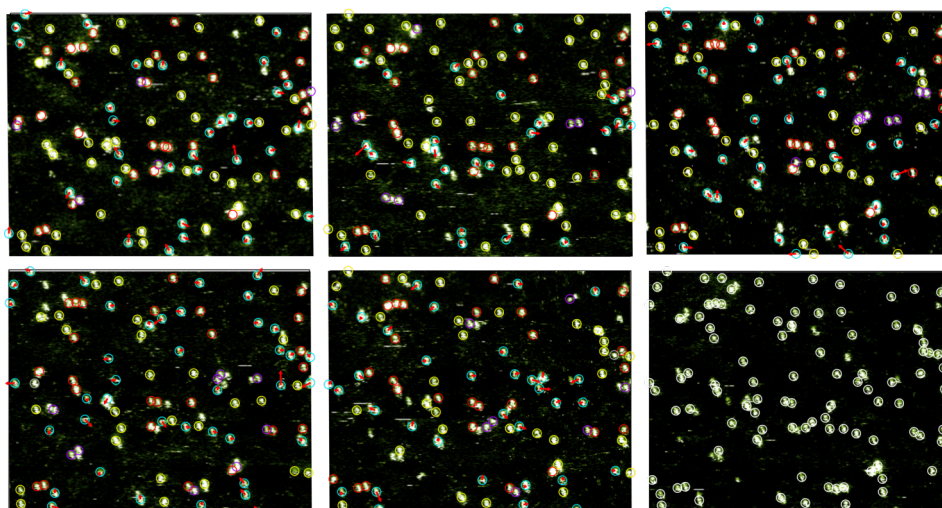


**Fig. 10.7:** Image series acquired at 185 K from the second measurement of 2,5-DHBA after processing with *TrackRead*.

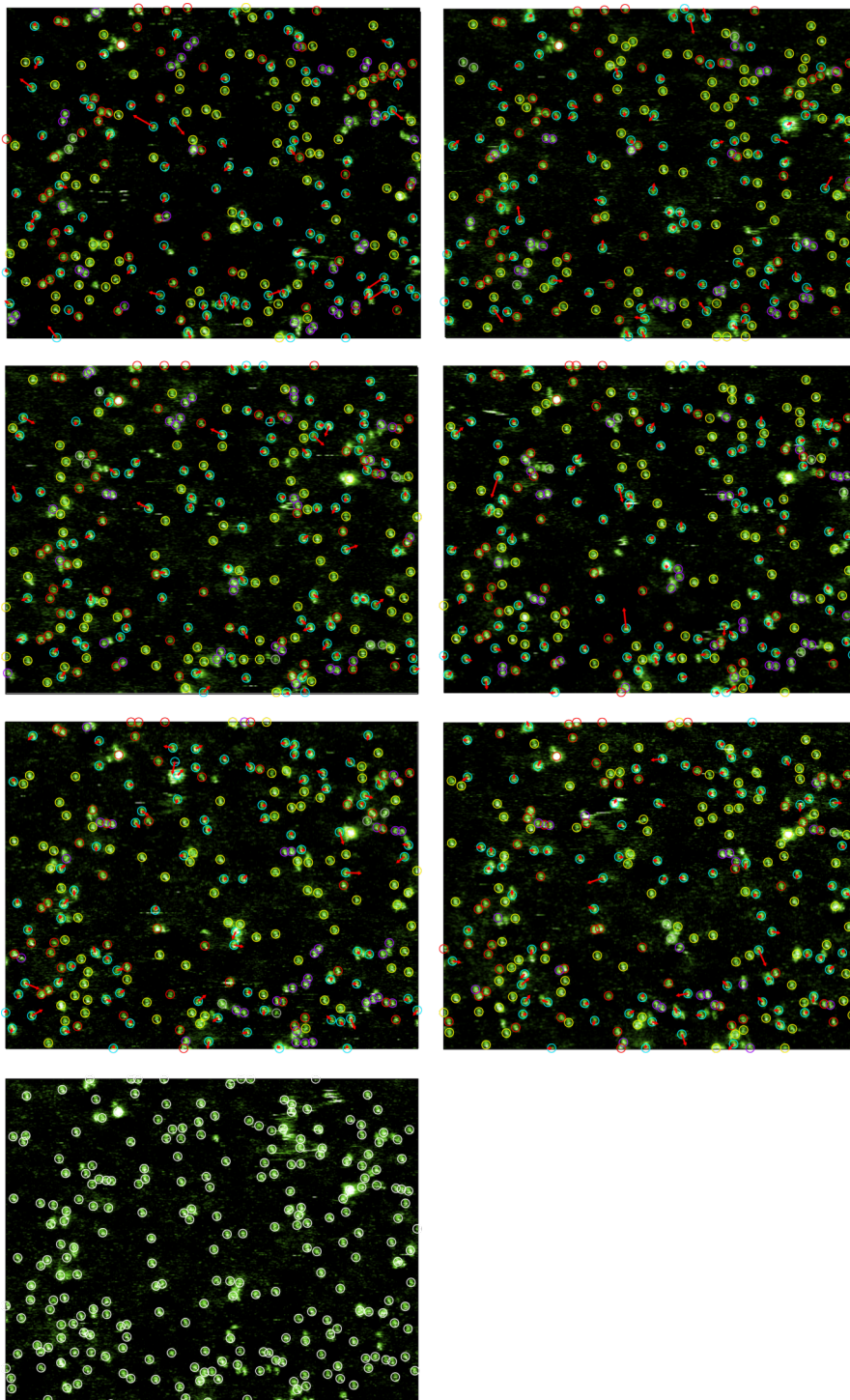


**Fig. 10.8:** Image series acquired at 189.5 K from the second measurement of 2,5-DHBA after processing with *TrackRead*.

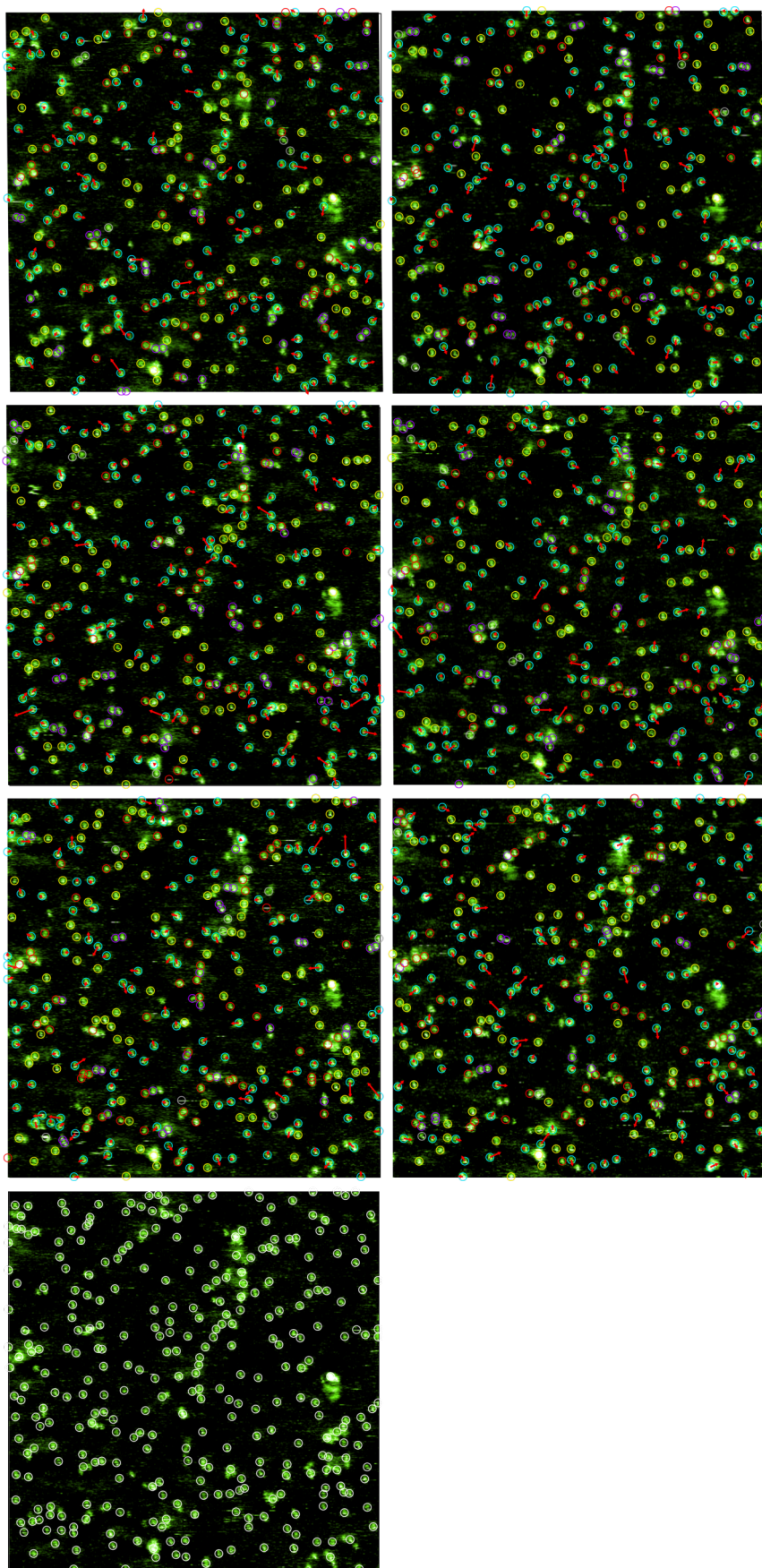


**Fig. 10.9:** Image series acquired at 194K from the second measurement of 2,5-DHBA after processing with *TrackRead*.

### 10.3.6 Graphs for the second measurement

These graphs correspond to Figure 6.6 and Figure 6.8 and were made for the data from the second measurement (see Section 6.3 for a detailed description).

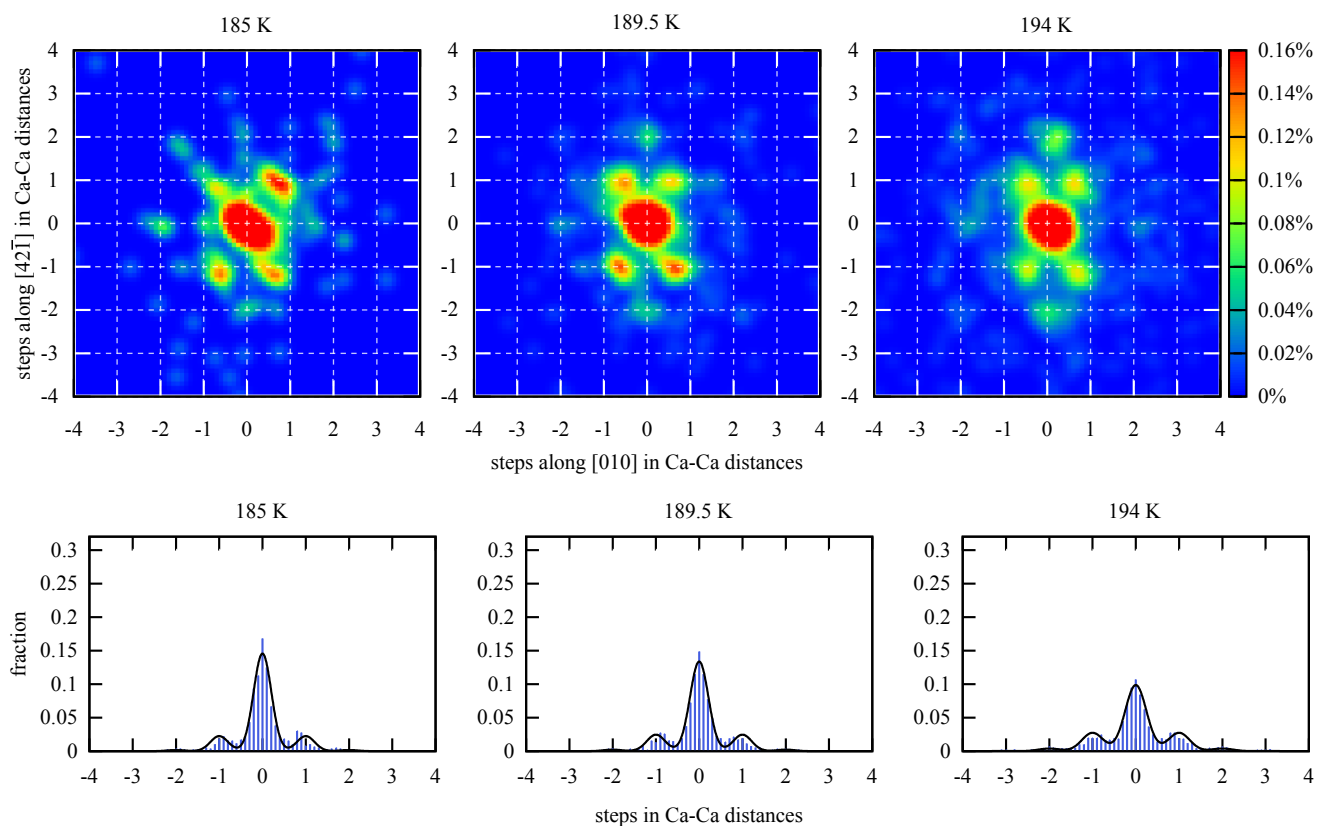


**Fig. 10.10:** Map of the motion vector density and histograms of the jumps along the jump directions for the second measurement.

## 10.4 ATPA diffusion and self-assembly

Figure 10.11 shows the complete image series from the ATPA measurements (Section 7.2.2). Colour code and sorting are identical to Section 10.3.5.

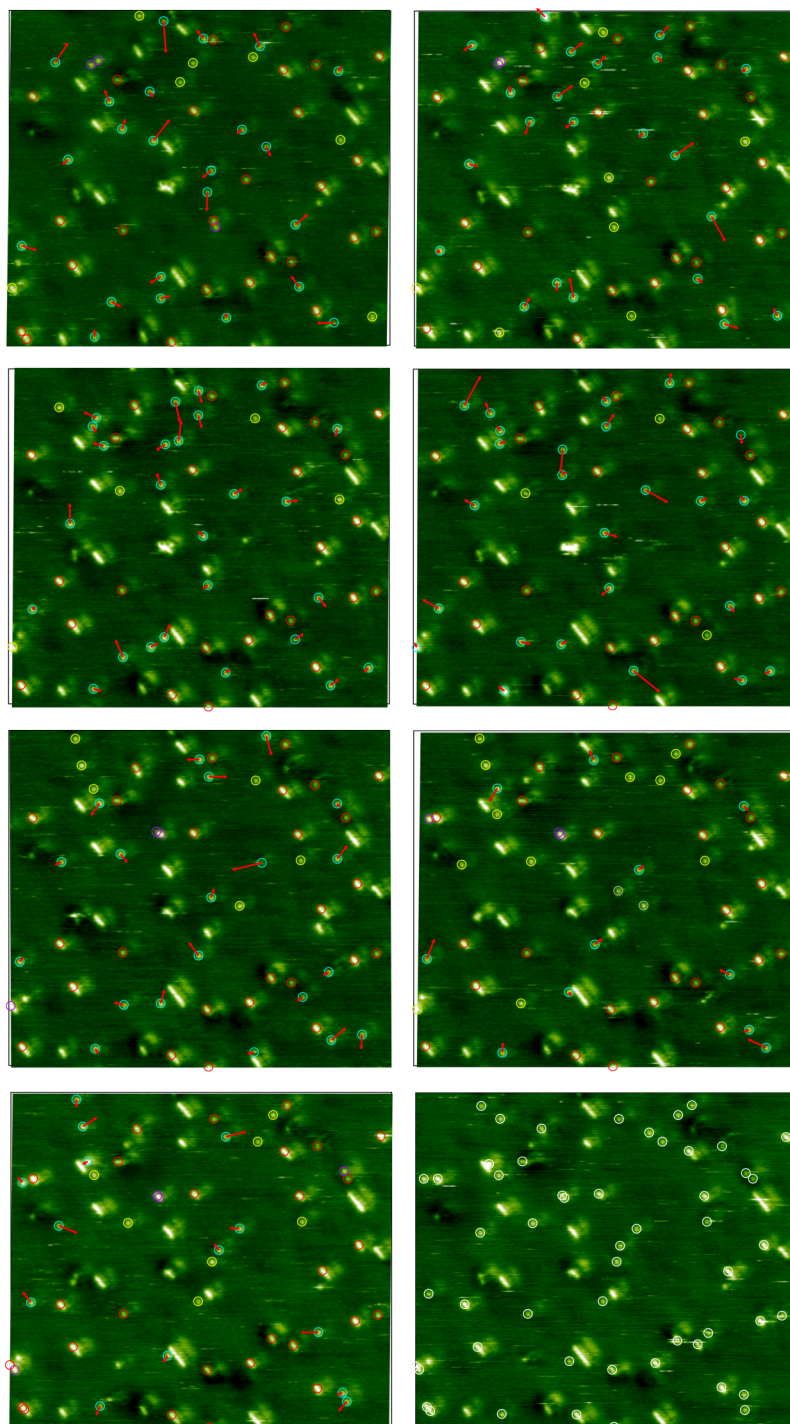


**Fig. 10.11:** Image series of ATPA molecules acquired at 245 K after processing with *TrackRead*.

## 10.5 Software list

This is a list of some selected software written during this thesis.

- *Justin*: fully automatic sublimation measurements with evaluation during measurement (Section 5.3).
- *Chantal*: evaluates sublimation data within seconds.
- *I12c* (I want to see): program for calculating the transformation to get a desired structure. Also evaluates 2D-FFTs and is able to perform a drift correction using the 2D-FFTs of an *up*- and *down*-image (Section 5.2).
- *EasyDrift*: the classic drift correction selecting characteristic points in consecutive images with an easy to use graphical user interface. Drift correction can be performed within a minute.
- *AlphaDrift*: calculates the drift speed by putting two images on top of each other and manually transforming them until they fit (Section 5.2). Produces corrected images within a minute.
- *TrackRead*: tool for processing motion tracking data (Section 5.1).
- *SurfaceCreator*: exists for calcite(104), dolomite(104) and diamond(001). Generates a *.pdb* or *.xyz* file of the surface.
- *ManipulatorDegassing*: program to control the *TDK-Lambda GEN-60* power supply. It includes the possibility to define ramp procedures. It stores current, voltage and temperature and also allows for degassing samples over night.
- *LakeshoreReader*: displays and stores the information from the *Lakeshore* temperature controller. This includes the heater output.
- *Qfit*: generates and opens *gnuplot* files to evaluate frequency sweeps. It determines the quality factor  $Q$  automatically by fitting phase and amplitude.





# Bibliography

- [1] G. M. Whitesides, “Self-assembly at all scales”, *Science* **2002**, *295*, 2418–2421.
- [2] R. P. Feynman, “Forces in molecules”, *Physical Review* **1939**, *56*, 340–343.
- [3] S. Weiner, L. Addadi, “Design strategies in mineralized biological materials”, *Journal of Materials Chemistry* **1997**, *7*, 689–702.
- [4] G. Binnig, H. Rohrer, C. Gerber, E. Weibel, “Surface studies by scanning tunneling microscopy”, *Physical Review Letters* **1982**, *49*, 57–61.
- [5] G. Binnig, C. F. Quate, C. Gerber, “Atomic force microscope”, *Physical Review Letters* **1986**, *56*, 930–933.
- [6] T. R. Albrecht, P. Grütter, D. Horne, D. Rugar, “Frequency modulation detection using high- $Q$  cantilevers for enhanced force microscope sensitivity”, *Journal of Applied Physics* **1991**, *69*, 668–673.
- [7] M. Körner, F. Loske, M. Einax, et al., “Second-layer induced island morphologies in thin-film growth of fullerenes”, *Physical Review Letters* **2011**, *107*, 016101:1–016101:4.
- [8] P. Rahe, M. Nimmrich, A. Greuling, et al., “Toward molecular nanowires self-assembled on an insulating substrate: heptahelicene-2-carboxylic acid on calcite (10 $\bar{1}$ 4)”, *The Journal of Physical Chemistry C* **2010**, *114*, 1547–1552.
- [9] A. Schiffrin, A. Riemann, W. Auwärter, et al., “Zwitterionic self-assembly of L-methionine nanogratings on the Ag(111) surface”, *Proceedings of the National Academy of Sciences* **2007**, *104*, 5279–5284.
- [10] G. Pawin, K. L. Wong, D. Kim, et al., “A surface coordination network based on substrate-derived metal adatoms with local charge excess”, *Angewandte Chemie International Edition* **2008**, *47*, 8442–8445.
- [11] P. A. Staniec, L. M. A. Perdigão, A. Saywell, N. R. Champness, P. H. Beton, “Hierarchical organisation on a two-dimensional supramolecular network”, *ChemPhysChem* **2007**, *8*, 2177–2181.
- [12] U. Schlickum, R. Decker, F. Klappenberger, et al., “Metal-organic honeycomb nanomeshes with tunable cavity size”, *Nano Letters* **2007**, *7*, 3813–3817.
- [13] F. Sedona, M. Di Marino, A. Basagni, L. Colazzo, M. Sambri, “Structurally tunable self-assembled 2D cocrystals of C<sub>60</sub> and porphyrins on the Ag (110) surface”, *The Journal of Physical Chemistry C* **2014**, *118*, 1587–1593.

- [14] D. Bonifazi, S. Mohnani, A. Llanes-Pallas, “Supramolecular chemistry at interfaces: molecular recognition on nanopatterned porous surfaces”, *Chemistry—A European Journal* **2009**, *15*, 7004–7025.
- [15] F. Kling, M. Kittelmann, A. Kühnle, “Adsorption structures of amino acids on calcite(104)” in *Imaging and manipulation of adsorbates using dynamic force microscopy*, (Eds.: P. Moriarty, S. Gauthier), Advances in atom and single molecule machines, Springer-Verlag, Berlin Heidelberg, **2015**, Chapter 8, pp. 119–129.
- [16] P. Rahe, J. Schütte, A. Kühnle, “NC-AFM contrast formation on the calcite (10 $\bar{1}$ 4) surface”, *Journal of Physics: Condensed Matter* **2012**, *24*, 084006:1–084006:14.
- [17] C. A. Orme, A. Noy, A. Wierzbicki, “Formation of chiral morphologies through selective binding of amino acids to calcite surface steps”, *Nature* **2001**, *411*, 775–779.
- [18] F. Rosei, M. Schunack, Y. Naitoh, et al., “Properties of large organic molecules on metal surfaces”, *Progress in Surface Science* **2003**, *71*, 95–146.
- [19] J. Weckesser, J. V. Barth, C. Cai, B. Müller, K. Kern, “Binding and ordering of large organic molecules on an anisotropic metal surface: PVBA on Pd(110)”, *Surface Science* **1999**, *431*, 168–173.
- [20] M. Schunack, T. R. Linderoth, F. Rosei, et al., “Long jumps in the surface diffusion of large molecules”, *Physical Review Letters* **2002**, *88*, 156102:1–156102:4.
- [21] F. Buchner, J. Xiao, E. Zillner, et al., “Diffusion, rotation, and surface chemical bond of individual 2*H*-tetraphenylporphyrin molecules on Cu(111)”, *The Journal of Physical Chemistry C* **2011**, *115*, 24172–24177.
- [22] T. Sonnleitner, I. Swart, N. Pavliček, A. Pöllmann, J. Repp, “Molecular symmetry governs surface diffusion”, *Physical Review Letters* **2011**, *107*, 186103:1–186103:4.
- [23] M. Kittelmann, P. Rahe, A. Gourdon, A. Kühnle, “Direct visualization of molecule deprotonation on an insulating surface”, *ACS Nano* **2012**, *6*, 7406–7411.
- [24] S. Barlow, R. Raval, “Complex organic molecules at metal surfaces: bonding, organisation and chirality”, *Surface Science Reports* **2003**, *50*, 201–341.
- [25] Y. Ye, W. Sun, Y. Wang, et al., “A unified model: self-assembly of trimesic acid on gold”, *Journal of Physical Chemistry C* **2007**, *111*, 10138–10141.
- [26] J. S. Lardge, D. M. Duffy, M. J. Gillan, “Investigation of the interaction of water with the calcite (10.4) surface using ab initio simulation”, *The Journal of Physical Chemistry C* **2009**, *113*, 7207–7212.
- [27] F. Kling, R. Bechstein, P. Rahe, A. Kühnle, “Self-assembly of organic molecules on insulating surfaces” in *Noncontact atomic force microscopy*, (Eds.: S. Morita, F. J. Giessibl, E. Meyer, R. Wiesendanger), Nanoscience and technology, Springer-Verlag, Berlin Heidelberg, **2015**, Chapter 9, pp. 147–171.
- [28] S. Chiang, “Scanning tunneling microscopy imaging of small adsorbed molecules on metal surfaces in an ultra-high vacuum environment”, *Chemical Reviews* **1997**, *97*, 1083–1096.
- [29] S. De Feyter, F. C. De Schryver, “Two-dimensional supramolecular self-assembly probed by scanning tunneling microscopy”, *Chemical Society Reviews* **2003**, *32*, 139–150.

- [30] N. K. Chaki, K. Vijayamohan, “Self-assembled monolayers as a tunable platform for biosensor applications”, *Biosensors and Bioelectronics* **2002**, *17*, 1–12.
- [31] J. C. Love, L. A. Estroff, J. K. Kriebel, R. G. Nuzzo, G. M. Whitesides, “Self-assembled monolayers of thiolates on metals as a form of nanotechnology”, *Chemical Reviews* **2005**, *105*, 1103–1169.
- [32] J. V. Barth, “Molecular architectonic on metal surfaces”, *Annual Review of Physical Chemistry* **2007**, *58*, 375–407.
- [33] F. Cicoira, C. Santato, F. Rosei, “Two-dimensional nanotemplates as surface cues for the controlled assembly of organic molecules” in *STM and AFM studies on (bio)molecular systems: unravelling the nanoworld*, (Ed.: P. Samorì), Topics in current chemistry 285, Springer-Verlag, Berlin Heidelberg, **2008**, Chapter 6, pp. 203–267.
- [34] A. Kühnle, “Self-assembly of organic molecules at metal surfaces”, *Current Opinion in Colloid & Interface Science* **2009**, *14*, 157–168.
- [35] L. Bartels, “Tailoring molecular layers at metal surfaces”, *Nature Chemistry* **2010**, *2*, 87–95.
- [36] R. Otero, J. M. Gallego, A. L. Vázquez de Parga, N. Martín, R. Miranda, “Molecular self-assembly at solid surfaces”, *Advanced Materials* **2011**, *23*, 5148–5176.
- [37] G. Whitesides, J. Mathias, C. Seto, “Molecular self-assembly and nanochemistry: a chemical strategy for the synthesis of nanostructures”, *Science* **1991**, *254*, 1312–1319.
- [38] J.-M. Lehn, “Toward self-organization and complex matter”, *Science* **2002**, *295*, 2400–2403.
- [39] J.-M. Lehn, “Supramolecular chemistry: from molecular information towards self-organization and complex matter”, *Reports on Progress in Physics* **2004**, *67*, 249–265.
- [40] G. R. Desiraju, “A bond by any other name”, *Angewandte Chemie International Edition* **2011**, *50*, 52–59.
- [41] G. R. Desiraju, P. S. Ho, L. Kloo, et al., “Definition of the halogen bond (IUPAC recommendations 2013)”, *Pure and Applied Chemistry* **2013**, *85*, 1711–1713.
- [42] S. Scheiner, “The pnico-gen bond: its relation to hydrogen, halogen, and other noncovalent bonds”, *Accounts of Chemical Research* **2013**, *46*, 280–288.
- [43] D. Mani, E. Arunan, “The X-C-Y (X = O/F, Y = O/S/F/Cl/Br/N/P) "carbon bond" and hydrophobic interactions”, *Physical Chemistry Chemical Physics* **2013**, *15*, 14377–14383.
- [44] C. A. Hunter, J. K. M. Sanders, “The nature of  $\pi$ - $\pi$  interactions”, *Journal of the American Chemical Society* **1990**, *112*, 5525–5534.
- [45] H. A. Skinner, J. A. Connor, “Metal-ligand bond-energies in organometallic compounds”, *Pure and Applied Chemistry* **1985**, *57*, 79–88.
- [46] J. N. Israelachvili, *Intermolecular and surface forces*, Academic Press, San Diego, 3rd ed., **2011**.
- [47] J.-M. Lehn, “Supramolecular chemistry-scope and perspectives: molecules, supermolecules, and molecular devices (Nobel lecture)”, *Angewandte Chemie International Edition* **1988**, *27*, 89–112.

- [48] L. J. Prins, P. Scrimin, “Covalent capture: merging covalent and noncovalent synthesis”, *Angewandte Chemie International Edition* **2009**, *48*, 2288–2306.
- [49] V. Oison, M. Koudia, M. Abel, L. Porte, “Influence of stress on hydrogen-bond formation in a halogenated phthalocyanine network”, *Physical Review B* **2007**, *75*, 035428:1–035428:6.
- [50] M. Forster, M. S. Dyer, M. Persson, R. Raval, “Assembly of chiral amino-acids at surfaces from a single molecule perspective: proline on Cu(110)”, *Topics in Catalysis* **2011**, *54*, 13–19.
- [51] M. Böhringer, K. Morgenstern, W.-D. Schneider, et al., “Two-dimensional self-assembly of supramolecular clusters and chains”, *Physical Review Letters* **1999**, *83*, 324–327.
- [52] A. Kühnle, L. M. Molina, T. R. Linderoth, B. Hammer, F. Besenbacher, “Growth of unidirectional molecular rows of cysteine on Au(110)”, *Physical Review Letters* **2004**, *93*, 086101:1–086101:4.
- [53] L. Scudiero, K. W. Hipps, D. E. Barlow, “A self-organized two-dimensional bimolecular structure”, *The Journal of Physical Chemistry B* **2003**, *107*, 2903–2909.
- [54] Y. L. Huang, W. Chen, H. Li, et al., “Tunable two-dimensional binary molecular networks”, *Small* **2010**, *6*, 70–75.
- [55] S. Lukas, G. Witte, C. Wöll, “Novel mechanism for molecular self-assembly on metal substrates: unidirectional rows of pentacene on Cu(110) produced by a substrate-mediated repulsion”, *Physical Review Letters* **2001**, *88*, 28301:1–28301:4.
- [56] P. Han, P. S. Weiss, “Electronic substrate-mediated interactions”, *Surface Science Reports* **2012**, *67*, 19–81.
- [57] J. Weckesser, J. V. Barth, K. Kern, “Mobility and bonding transition of C<sub>60</sub> on Pd(110)”, *Physical Review B* **2001**, *64*, 161403:1–161403:4.
- [58] J. V. Barth, “Transport of adsorbates at metal surfaces: from thermal migration to hot precursors”, *Surface Science Reports* **2000**, *40*, 75–149.
- [59] M. Roos, A. Breitrock, H. E. Hoster, R. J. Behm, “Entropic stabilization of large adsorbates on weakly binding substrates—a thermal desorption and scanning tunneling microscopy study”, *Physical Chemistry Chemical Physics* **2010**, *12*, 818–822.
- [60] T. Kunstmann, A. Schlarb, M. Fendrich, et al., “Dynamic force microscopy study of 3,4,9,10-perylenetetracarboxylic dianhydride on KBr(001)”, *Physical Review B* **2005**, *71*, 121403:1–121403:4.
- [61] R. Gutzler, L. Cardenas, F. Rosei, “Kinetics and thermodynamics in surface-confined molecular self-assembly”, *Chemical Science* **2011**, *2*, 2290–2300.
- [62] H. Brune, G. S. Bales, J. Jacobsen, C. Boragno, K. Kern, “Measuring surface diffusion from nucleation island densities”, *Physical Review B* **1999**, *60*, 5991–6006.
- [63] F. Loske, J. Lübke, J. Schütte, M. Reichling, A. Kühnle, “Quantitative description of C<sub>60</sub> diffusion on an insulating surface”, *Physical Review B* **2010**, *82*, 155428:1–155428:5.

- [64] T. Glatzel, L. Zimmerli, S. Koch, S. Kawai, E. Meyer, “Molecular assemblies grown between metallic contacts on insulating surfaces”, *Applied Physics Letters* **2009**, *94*, 63303:1–63303:3.
- [65] L. Nony, R. P. Bennewitz, O. D. Pfeiffer, et al., “Cu-TBPP and PTCDA molecules on insulating surfaces studied by ultra-high-vacuum non-contact AFM”, *Nanotechnology* **2004**, *15*, S91–S96.
- [66] L. Nony, E. Gnecco, A. Baratoff, et al., “Observation of individual molecules trapped on a nanostructured insulator”, *Nano Letters* **2004**, *4*, 2185–2189.
- [67] S. A. Burke, J. M. Mativetsky, R. Hoffmann, P. Grütter, “Nucleation and sub-monolayer growth of C<sub>60</sub> on KBr”, *Physical Review Letters* **2005**, *94*, 096102:1–096102:4.
- [68] O. Pfeiffer, E. Gnecco, L. Zimmerli, et al., “Force microscopy on insulators: imaging of organic molecules”, *Journal of Physics: Conference Series* **2005**, *19*, 166–174.
- [69] J. M. Mativetsky, S. A. Burke, S. Fostner, P. Grutter, “Nanoscale pits as templates for building a molecular device”, *Small* **2007**, *3*, 818–821.
- [70] L. Zimmerli, S. Maier, T. Glatzel, et al., “Formation of molecular wires on nanostructured KBr”, *Journal of Physics: Conference Series* **2007**, *61*, 1357–1360.
- [71] S. Maier, L.-A. Fendt, L. Zimmerli, et al., “Nanoscale engineering of molecular porphyrin wires on insulating surfaces”, *Small* **2008**, *4*, 1115–1118.
- [72] S. A. Burke, W. Ji, J. M. Mativetsky, et al., “Strain induced dewetting of a molecular system: bimodal growth of PTCDA on NaCl”, *Physical Review Letters* **2008**, *100*, 186104:1–186104:4.
- [73] T. Dienel, C. Loppacher, S. C. B. Mannsfeld, R. Forker, T. Fritz, “Growth-mode-induced narrowing of optical spectra of an organic adlayer”, *Advanced Materials* **2008**, *20*, 959–963.
- [74] S. A. Burke, J. M. LeDue, Y. Miyahara, et al., “Determination of the local contact potential difference of PTCDA on NaCl: a comparison of techniques”, *Nanotechnology* **2009**, *20*, 264012:1–264012:8.
- [75] S. A. Burke, J. M. Topple, P. Grütter, “Molecular dewetting on insulators”, *Journal of Physics: Condensed Matter* **2009**, *21*, 423101:1–423101:16.
- [76] S. Fremy, A. Schwarz, K. Lämmle, M. Prosenc, R. Wiesendanger, “The monomer-to-dimer transition and bimodal growth of Co–salen on NaCl(001): a high resolution atomic force microscopy study”, *Nanotechnology* **2009**, *20*, 405608:1–405608:9.
- [77] M. Fendrich, M. Lange, C. Weiss, T. Kunstmann, R. Möller, “N,N′-dimethylperylene-3,4,9,10-bis(dicarboximide) on alkali halide (001) surfaces”, *Journal of Applied Physics* **2009**, *105*, 094311:1–094311:5.
- [78] S. Kawai, S. Maier, T. Glatzel, et al., “Cutting and self-healing molecular wires studied by dynamic force microscopy”, *Applied Physics Letters* **2009**, *95*, 103109:1–103109:3.
- [79] R. Pawlak, L. Nony, F. Bocquet, et al., “Supramolecular assemblies of 1,4-benzene-diboronic acid on KCl(001)”, *Journal of Physical Chemistry C* **2010**, *114*, 9290–9295.

- [80] B. Such, T. Trevethan, T. Glatzel, et al., “Functionalized truxenes: adsorption and diffusion of single molecules on the KBr(001) Surface”, *ACS Nano* **2010**, *4*, 3429–3439.
- [81] T. Glatzel, L. Zimmerli, S. Kawai, et al., “Oriented growth of porphyrin-based molecular wires on ionic crystals analysed by NC-AFM”, *Beilstein Journal of Nanotechnology* **2011**, *2*, 34–39.
- [82] A. Hinaut, K. Lekhal, G. Aivazian, et al., “NC-AFM Study of the adsorption of hexamethoxytriphenylene on KBr(001)”, *The Journal of Physical Chemistry C* **2011**, *115*, 13338–13342.
- [83] L. Nony, F. Bocquet, F. Para, et al., “Dipole-driven self-organization of zwitterionic molecules on alkali halide surfaces”, *Beilstein Journal of Nanotechnology* **2012**, *3*, 285–293.
- [84] J. M. Topple, S. A. Burke, W. Ji, et al., “Tailoring the morphology and dewetting of an organic thin film”, *The Journal of Physical Chemistry C* **2011**, *115*, 217–224.
- [85] T. Trevethan, B. Such, T. Glatzel, et al., “Organic molecules reconstruct nanostructures on ionic surfaces”, *Small* **2011**, *7*, 1264–1270.
- [86] C. Barth, M. Gingras, A. S. Foster, et al., “Two-dimensional nanostructured growth of nanoclusters and molecules on insulating surfaces”, *Advanced Materials* **2012**, *24*, 3228–3232.
- [87] F. Bocquet, L. Nony, S. C. B. Mannsfeld, et al., “Inhomogeneous relaxation of a molecular layer on an insulator due to compressive stress”, *Physical Review Letters* **2012**, *108*, 206103:1–206103:5.
- [88] A. Hinaut, A. Pujol, F. Chaumeton, et al., “An NC-AFM and KPFM study of the adsorption of a triphenylene derivative on KBr(001)”, *Beilstein Journal of Nanotechnology* **2012**, *3*, 221–229.
- [89] J. L. Neff, J. Götzen, E. Li, M. Marz, R. Hoffmann-Vogel, “Molecular-resolution imaging of pentacene on KCl(001)”, *Beilstein Journal of Nanotechnology* **2012**, *3*, 186–191.
- [90] R. Pawlak, S. Kawai, S. Fremy, T. Glatzel, E. Meyer, “High-resolution imaging of C<sub>60</sub> molecules using tuning-fork-based non-contact atomic force microscopy”, *Journal of Physics: Condensed Matter* **2012**, *24*, 084005:1–084005:10.
- [91] B. Hoff, M. Gingras, R. Peresutti, et al., “Mechanisms of the adsorption and self-assembly of molecules with polarized functional groups on insulating surfaces”, *The Journal of Physical Chemistry C* **2014**, *118*, 14569–14578.
- [92] J. Schütte, R. Bechstein, M. Rohlfing, M. Reichling, A. Kühnle, “Cooperative mechanism for anchoring highly polar molecules at an ionic surface”, *Physical Review B* **2009**, *80*, 205421:1–205421:5.
- [93] F. Loske, M. Reichling, A. Kühnle, “Steering molecular island morphology on an insulator surface by exploiting sequential deposition”, *Chemical Communications* **2011**, *47*, 10386–10388.
- [94] F. Loske, M. Reichling, A. Kühnle, “Deposition sequence determines morphology of C<sub>60</sub> and 3,4,9,10-perylenetetracarboxylic diimide islands on CaF<sub>2</sub>(111)”, *Japanese Journal of Applied Physics* **2011**, *50*, 08LB07:1–08LB07:4.

- [95] C. Loppacher, U. Zerweck, D. Koehler, et al., “Physical vapour deposition of alkyl phosphonic acid on mica and HOPG investigated by NC-AFM”, *Nanotechnology* **2007**, *18*, 084003:1–084003:5.
- [96] M. Kittelmann, P. Rahe, M. Nimmrich, et al., “On-surface covalent linking of organic building blocks on a bulk insulator”, *ACS Nano* **2011**, *5*, 8420–8425.
- [97] C. M. Hauke, P. Rahe, M. Nimmrich, et al., “Molecular self-assembly of enantiopure heptahelicene-2-carboxylic acid on calcite (10 $\bar{1}$ 4)”, *The Journal of Physical Chemistry C* **2012**, *116*, 4637–4641.
- [98] M. Kittelmann, P. Rahe, A. Kühnle, “Molecular self-assembly on an insulating surface: interplay between substrate templating and intermolecular interactions”, *Journal of Physics: Condensed Matter* **2012**, *24*, 354007:1–354007:5.
- [99] P. Rahe, R. Lindner, M. Kittelmann, M. Nimmrich, A. Kühnle, “From dewetting to wetting molecular layers: C<sub>60</sub> on CaCO<sub>3</sub>(10 $\bar{1}$ 4) as a case study”, *Physical Chemistry Chemical Physics* **2012**, *14*, 6544–6548.
- [100] P. Rahe, M. Nimmrich, A. Kühnle, “Templating: substrate templating upon self-assembly of hydrogen-bonded molecular networks on an insulating surface”, *Small* **2012**, *8*, 2968–2968.
- [101] C. Hauke, R. Bechstein, M. Kittelmann, et al., “Controlling molecular self-assembly on an insulating surface by rationally designing an efficient anchor structural flexibility”, *ACS Nano* **2013**, *7*, 5491–5498.
- [102] M. Kittelmann, M. Nimmrich, R. Lindner, A. Gourdon, A. Kühnle, “Sequential and site-specific on-surface synthesis on a bulk insulator”, *ACS Nano* **2013**, *7*, 5614–5620.
- [103] P. Rahe, M. Kittelmann, J. L. Neff, et al., “Tuning molecular self-assembly on bulk insulator surfaces by anchoring of the organic building blocks”, *Advanced Materials* **2013**, *25*, 3948–3956.
- [104] M. Kittelmann, M. Nimmrich, J. L. Neff, et al., “Controlled activation of substrate templating in molecular self-assembly by deprotonation”, *The Journal of Physical Chemistry C* **2013**, *117*, 23868–23874.
- [105] R. Lindner, P. Rahe, M. Kittelmann, et al., “Substrate templating guides the photoinduced reaction of C<sub>60</sub> on calcite”, *Angewandte Chemie International Edition* **2014**, *53*, 7952–7955.
- [106] J. L. Neff, M. Kittelmann, R. Bechstein, A. Kühnle, “Decisive influence of substitution positions in molecular self-assembly”, *Physical Chemistry Chemical Physics* **2014**, *16*, 15437–15443.
- [107] T. David, J. K. Gimzewski, D. Purdie, B. Reihl, R. R. Schlittler, “Epitaxial growth of C<sub>60</sub> on Ag(110) studied by scanning tunneling microscopy and tunneling spectroscopy”, *Physical Review B* **1994**, *50*, 5810–5813.
- [108] M. Watkins, T. Trevethan, M. L. Sushko, A. L. Shluger, “Designing molecular architecture to control diffusion and adsorption on insulating surfaces”, *The Journal of Physical Chemistry C* **2008**, *112*, 4226–4231.
- [109] F. J. Giessibl, “Advances in atomic force microscopy”, *Reviews of Modern Physics* **2003**, *75*, 949–983.

- [110] P. Rahe, R. Bechstein, J. Schütte, F. Ostendorf, A. Kühnle, “Repulsive interaction and contrast inversion in noncontact atomic force microscopy imaging of adsorbates”, *Physical Review B* **2008**, *77*, 195410:1–195410:6.
- [111] J. Stirling, “Control theory for scanning probe microscopy revisited”, *Beilstein Journal of Nanotechnology* **2014**, *5*, 337–345.
- [112] C. Hauke, “Systematic functionalization of molecules for molecular self-assembly”, PhD thesis, Johannes Gutenberg University Mainz, **2013**.
- [113] M. Nonnenmacher, “Kelvin probe force microscopy”, *Applied Physics Letters* **1991**, *58*, 2921–2923.
- [114] F. Kling, “Tryptophan und Tyrosin auf Calcit(104)”, diploma thesis, Johannes Gutenberg University Mainz, **2012**.
- [115] P. Rahe, “The calcite(10 $\bar{1}$ 4) surface: a versatile substrate for molecular self-assembly”, PhD thesis, Johannes Gutenberg University Mainz, **2011**.
- [116] S. Aeschlimann, “Untersuchung der temperaturabhängigen Strukturbildung und Kinetik der Deprotonierung von 2,5-DHBA auf Calcit”, bachelor thesis, Johannes Gutenberg University Mainz, **2014**.
- [117] B. Heep, “Aufbau und Inbetriebnahme eines Messsystems zur temperaturprogrammierten Desorption von Molekülen auf Isolatoroberflächen”, diploma thesis, Johannes Gutenberg University Mainz, **2014**.
- [118] J. Schindelin, I. Arganda-Carreras, E. Frise, et al., “Fiji: an open-source platform for biological-image analysis”, *Nature Methods* **2012**, *9*, 676–682.
- [119] P. Rahe, R. Bechstein, A. Kühnle, “Vertical and lateral drift corrections of scanning probe microscopy images”, *Journal of Vacuum Science & Technology B* **2010**, *28*, C4E31–C4E38.
- [120] J. T. Woodward, D. K. Schwartz, “Removing drift from scanning probe microscope images of periodic samples”, *Journal of Vacuum Science & Technology B* **1998**, *16*, 51–53.
- [121] G. Ehrlich, “Atomic displacements in one- and two-dimensional diffusion”, *The Journal of Chemical Physics* **1966**, *44*, 1050–1055.
- [122] H. Marbach, H.-P. Steinrück, “Studying the dynamic behaviour of porphyrins as prototype functional molecules by scanning tunnelling microscopy close to room temperature”, *Chemical Communications* **2014**, *50*, 9034–9048.
- [123] J. V. Barth, G. Costantini, K. Kern, “Engineering atomic and molecular nanostructures at surfaces”, *Nature* **2005**, *437*, 671–679.
- [124] A. Tekiel, J. S. Prauzner-Bechcicki, S. Godlewski, J. Budzioch, M. Szymonski, “Self-assembly of terephthalic acid on rutile TiO<sub>2</sub>(110): toward chemically functionalized metal oxide surfaces”, *Journal of Physical Chemistry C* **2008**, *112*, 12606–12609.
- [125] P. Rahe, M. Nimmrich, A. Nefedov, et al., “Transition of molecule orientation during adsorption of terephthalic acid on rutile TiO<sub>2</sub>(110)”, *Journal of Physical Chemistry C* **2009**, *113*, 17471–17478.
- [126] G. Ehrlich, K. Stolt, “Surface diffusion”, *Annual Review of Physical Chemistry* **1980**, *31*, 603–637.



- [127] P. J. Feibelman, “The first wetting layer on a solid”, *Physics Today* **2010**, *63*, 34–39.
- [128] C. Marutschke, “Three-dimensional imaging of the solid-liquid interface with high-resolution atomic force microscopy”, PhD thesis, Johannes Gutenberg University Mainz, **2015**.
- [129] F. Loske, P. Rahe, A. Kühnle, “Contrast inversion in non-contact atomic force microscopy imaging of C<sub>60</sub> molecules”, *Nanotechnology* **2009**, *20*, 264010:1–264010:6.



## List of Figures

2.1	Structural variety of self-assembled patterns. . . . .	6
2.2	Diffusion barrier plots. . . . .	8
2.3	Schematic drawing of the Gibbs energy for a molecule on a surface. . .	10
2.4	Gibbs energy for metastable structures. . . . .	10
2.5	Molecular structures on insulating surfaces. . . . .	12
2.6	C <sub>60</sub> on insulating surfaces. . . . .	13
2.7	Different strategies for enhancing the anchoring of molecules towards a surface. . . . .	15
2.8	Activation of substrate templating ascribed to deprotonation. . . . .	17
2.9	BPDCA on calcite(104). . . . .	17
2.10	Oligo( <i>p</i> -benzamide) molecules on calcite(104). . . . .	19
3.1	Forces and resulting frequency shift. . . . .	22
3.2	Schematic drawing of the AFM setup. . . . .	24
3.3	Example to show how a PLL works. . . . .	25
3.4	I-gain simulation. . . . .	27
3.5	The measurement chamber. . . . .	28
4.1	The calcite(104) surface. . . . .	30
4.2	Molecular structures. . . . .	31
4.3	Schematic drawings of the molecules and the surface. . . . .	31
5.1	Schematic drawing of the data processing with <i>TrackRead</i> . . . . .	33
5.2	Image transformation using motion vectors. . . . .	34
5.3	Motion vector density map with and without transformation with <i>TrackRead</i> . . . . .	36
5.4	Functional principle of <i>I12c</i> . . . . .	37
5.5	Graphical user interface for <i>I12c</i> . . . . .	39
5.6	2D-FFT evaluation. . . . .	40
5.7	Drift compensation using 2D-FFTs. . . . .	42
5.8	Application of the drift correction with <i>I12c</i> . . . . .	42
5.9	<i>AlphaDrift</i> . . . . .	44
5.10	Screen during experiments performed with <i>Justin</i> . . . . .	45
5.11	Sublimation curve acquired with <i>Justin</i> . . . . .	46
5.12	Evaluation of the sublimation data with <i>Justin</i> . . . . .	47

5.13	Plot of sublimation rates generated with <i>Justin</i> . . . . .	48
6.1	Striped and dense phase of 2,5-DHBA. . . . .	51
6.2	Drift corrected and calibrated high resolution image at 185 K of 2,5-DHBA. . . . .	52
6.3	Coverage between 2,5-DHBA islands. . . . .	53
6.4	Determination of the critical coverage of 2,5-DHBA for island formation. . . . .	54
6.5	Motion tracking of 2,5-DHBA molecules. . . . .	55
6.6	Density maps of motion vectors for 2,5-DHBA for different temperatures. . . . .	56
6.7	Explanation for the jump directions of 2,5-DHBA. . . . .	56
6.8	Histograms of 2,5-DHBA jumps for different temperatures. . . . .	57
6.9	Arrhenius plot for the diffusion of 2,5-DHBA. . . . .	58
7.1	TPA at room temperature for different coverages. . . . .	62
7.2	High coverage images of TPA at room temperature. . . . .	63
7.3	TPA after heating. . . . .	64
7.4	TPA and BrTPA at low temperatures. . . . .	66
7.5	Imaging all self-assembly processes of ATPA. . . . .	67
7.6	Density map of motion vectors for ATPA. . . . .	68
7.7	Self-assembly processes for ATPA. . . . .	68
8.1	TPD spectra of water on calcite(104). . . . .	72
8.2	Coexistence of two different structures at low coverages of water. . . . .	73
8.3	Coverage dependent measurements of H <sub>2</sub> O on calcite(104). . . . .	74
8.4	Water desorption observed with AFM. . . . .	75
8.5	The structure of water on calcite. . . . .	76
10.1	Alternative figure showing the calcite surface. . . . .	82
10.2	Sublimation curves for TPA, ATPA and BrTPA. . . . .	82
10.3	The c(4×2) phase of 2,5-DHBA. . . . .	83
10.4	Image series from the diffusion measurements (1st measurement, 185 K). . . . .	86
10.5	Image series from the diffusion measurements (1st measurement, 189.5 K). . . . .	87
10.6	Image series from the diffusion measurements (1st measurement, 194 K). . . . .	88
10.7	Image series from the diffusion measurements (2nd measurement, 185 K). . . . .	88
10.8	Image series from the diffusion measurements (2nd measurement, 189.5 K). . . . .	89
10.9	Image series from the diffusion measurements (2nd measurement, 194 K). . . . .	90
10.10	Motion vector density maps and histograms for the diffusion of 2,5-DHBA (2nd measurement). . . . .	91
10.11	Image series from the ATPA measurements. . . . .	92

## List of Tables

2.1	Intermolecular interactions. . . . .	5
4.1	Molecule properties. . . . .	32
5.1	Calibration parameters for UHV I and UHV II. . . . .	38



## List of acronyms

<b>2D-FFT</b>	two-dimensional fast Fourier transform
<b>AFM</b>	atomic force microscope
<b>ATPA</b>	2-aminoterephthalic acid
<b>BPDCA</b>	biphenyl-4,4'-dicarboxylic acid
<b>BrTPA</b>	2-bromoterephthalic acid
<b>DHBA</b>	dihydroxybenzoic acid
<b>FM-AFM</b>	frequency-modulation atomic force microscopy
<b>FM-KPFM</b>	frequency-modulation Kelvin probe force microscopy
<b>GUI</b>	graphical user interface
<b>NC-AFM</b>	non-contact atomic force microscope
<b>PLL</b>	phase-locked loop
<b>PSD</b>	position sensitive detector
<b>STM</b>	scanning tunnelling microscope
<b>TPA</b>	terephthalic acid
<b>TPD</b>	temperature-programmed desorption
<b>UHV</b>	ultra-high vacuum
<b>VCO</b>	voltage-controlled oscillator





## Publication list

- F. Kling, R. Bechstein, P. Rahe, A. Kühnle  
“Self-assembly of organic molecules on insulating surfaces”  
in *Noncontact atomic force microscopy*, (Eds.: S. Morita, F. J. Giessibl, E. Meyer, R. Wiesendanger), Nanoscience and technology, Springer-Verlag, Berlin Heidelberg, **2015**, Chapter 9, pp. 147–171.
- F. Kling, M. Kittelmann, A. Kühnle  
“Adsorption structures of amino acids on calcite(104)”  
in *Imaging and manipulation of adsorbates using dynamic force microscopy*, (Eds.: P. Moriarty, S. Gauthier), Advances in atom and single molecule machines, Springer-Verlag, Berlin Heidelberg, **2015**, Chapter 8, pp. 119–129.
- M. Schreiber, M. Eckardt, S. Klassen, H. Adam, M. Nalbach, L. Greifenstein, F. Kling, M. Kittelmann, R. Bechstein, A. Kühnle  
“How deprotonation changes molecular self-assembly—an AFM study in liquid environment”  
*Soft Matter* **2013**, 9, 7145–7149.



# Acknowledgement







# Curriculum vitae





## Colophon

This thesis was typeset with L<sup>A</sup>T<sub>E</sub>X 2<sub>ε</sub>. It uses the *Clean Thesis* style developed by Ricardo Langner. The design of the *Clean Thesis* style is inspired by user guide documents from Apple Inc.

Download the *Clean Thesis* style at <http://cleanthesis.der-ric.de/>.

